Department of Electrical, Electronics and Computer Engineering
Collage of Agriculture , Engineering and Science.

CONTROL OF FIVE-LEVEL VOLTAGE SOURCE CONVERTERS USED WITH A TYPE-4 WIND TURBINE

By

Ndumiso Zungu

University of KwaZulu-Natal

A dissertation submitted in fulfillment of the requirements for the degree of

MASTER OF SCIENCE IN ELECTRICAL ENGINEERING

Supervisor:
Prof. J Agee

30 July 2023

Declaration

I, Ndumiso Zungu, declare that :

1. The research reported in this dissertation, except where otherwise indicated, is my original research.

2. This dissertation has not been submitted for any degree or examination at any other university.

3. This dissertation does not contain other person's data, pictures, graphs, or other information unless specifically acknowledged as being sourced from other persons.

4. This dissertation does not contain other person's writing unless specifically acknowledged as being sourced from other researchers. Where other written sources have been quoted, then:

   (a) Their words have been re-written, but the general information attributed to them has been referenced.
   (b) Where their exact words have been used, then their writing has been placed in italics and inside quotation marks and referenced.

5. This dissertation does not contain text, graphics or tables copied and pasted from the internet, unless specifically acknowledged, and the source being detailed in the dissertation and in the Reference sections.

Signed:

.....
Mr. Ndumiso Zungu

As the candidate's Supervisor, I agree/do not agree to the submission of this dissertation.
Signed:

.....
Prof. John Agee
Date:

Abstract

Wind Energy Conversion Systems (WECSs) have attracted considerable attention and emerged as a highly promising and advancing renewable energy option. A typical WECS setup involves a Permanent Magnet Synchronous Generator (PMSG) connected to the power grid via power electronics converters. Nevertheless, the commonly used two-level Voltage Source Converter (2L VSC) configurations suffer from drawbacks such as increased switching losses, significant harmonic distortion at the output, and the need for additional Electromagnetic Interference (EMI) filters. Overcoming these challenges can be achieved through the adoption of multi-level converter topologies, which offer several advantages over conventional ones. These benefits include reduced switching losses, improved overall efficiency, and a decreased number of filtering elements required. By employing multi-level converters, the limitations of traditional 2L VSC topologies can be mitigated, making them a more efficient and suitable replacement.

The main objective of this research was to optimize the control of the proposed WECS by utilizing the Five Level Neutral Point Clamped (5L NPC) Voltage Source Converter (VSC) topology. The ultimate goal was to enhance the stability and power quality of the WECS when integrated into the grid system. The research findings are based on simulations carried out using the Power Systems Computer-Aided Design (PSCAD) software, which incorporates built-in power electronics device models. The study focused on controlling both sides of the converter, namely the Machine Side Converter (MSC) controller and the Grid Side Converter (GSC) controller, with the aim of improving the overall system performance. To achieve this, the control scheme employs the Vector-Oriented Control (VOC) strategy, along with phase lead and lag compensators, to effectively regulate the power flow delivered to the grid and achieve a unity power factor.

Ultimately, the simulation results convincingly demonstrated the enhanced efficiency of the overall system performance. Specifically, the study analyzed and compared Total Harmonic Distortion (THD) with a conventional converter topology under varying wind speeds. The THD values for the simulated voltage and current using the 2L VSC were found to be: 56.48% at 8m/s, 58.03% at 16m/s, and 2.35% at 8m/s, 8.95% at 16m/s, respectively. Nevertheless, by substituting the 2L NPC with the suggested 5L NPC topology, substantial improvements were achieved. The THD voltage saw a significant reduction of 26.63% at 8m/s, 30.5% at 16m/s while the current experienced a slight drop of 0.2% at 8m/s, 6.52% at 16m/s respectively.

This adoption of the proposed topology effectively mitigated the THD percentage, resulting in a much better waveform quality. Moreover, several other advantages were observed, including an increase in voltage amplitude with a high-quality waveform and a decrease in peak THD overshoot during rapid wind changes. In summary, the results demonstrated satisfactory transient and steady-state performance of the proposed system, with notable enhancements in total voltage and current THD. The study's findings underscore the effectiveness of the 5L NPC topology in improving the overall performance and power quality of the WECS.

Dedication

I dedicate this dissertation to the Almighty God and his son Jesus Christ, who has guided and blessed me throughout this journey of knowledge and discovery. Additionally, I would like to express my heartfelt gratitude to my family and friends, whose unwavering support and encouragement have been the pillars of strength in my pursuit of education.

To my beloved family, thank you for your love, understanding and sacrifices, especially to my mother **Sibongile Sangweni** and my later aunt **Nomusa Sangweni**. Your belief in me has been a constant source of motivation, and I am deeply grateful for the opportunities you have provided me with.

To my esteemed dissertation supervisor Pro. John Agee, I am profoundly grateful for your expertise, patience, and valuable guidance. Your insightful feedback and constructive criticism have been instrumental in shaping the direction of this research. Your mentorship has been invaluable, and I have learned so much under your guidance.

To my dear friends, your encouragement, camaraderie, and belief in my abilities have been invaluable. Your presence in my life has made this academic journey more joyful and meaningful.

"Give thanks to the Lord, for He is good; His love endures forever." - Psalm 136:1

Contents

List of Figures

List of Tables

0.1 Abbreviations

2L VSC	Two Level Voltage Source Converter
5L NPC	Five Level Neutral-Point Clamped
AC	Alternating Current
APOD	Alternative Phase Opposition Disposition
CHB	Cascaded H-Bridge
DC	Direct Current
DFIG	Doubly-Fed Induction Generator
Eq.	Equation
FC	Flying-Capacitor
FSWT	Fixed Speed Wind Turbine
HVAC	High Voltage Alternating Current Transmission System
HVDC	High Voltage Direct Current Transmission System
IGBT	Insulated Gate Bipolar Transistor
IRP	Integrated Resource Plan
MPPT	Maximum Power Point Tracking
NPC	Neutral-Point Clamped
ORB	Optimal Relationship Based MPPT
OTC	Optimal Torque Control MPPT
PD	Phase Disposition
PSCAD	Power Systems Computer Aided Design
P&O	Perturb & Observe
PLL	Phase Locked Loop
POD	Phase Opposition Disposition
PWM	Pulse Width Modulation
SCIG	Squirrel Cage Induction Generator
SVM	Space Vector Modulation
TSR	Tip Speed Ratio
VSC	Voltage Source Converter
VOC	Vector Oriented Control
VSWT	Variable Speed Wind Turbine
WECS	Wind Energy Conversion System

Chapter 1

Introduction

1.1 Background

Given the scarcity and environmental concerns associated with fossil fuels, renewable energy has emerged as a viable alternative energy source. However, integrating renewable energy into grid power networks poses challenges both theoretically and practically. Among renewable energy technologies, WECS stand out as one of the most promising options. Over the past few decades, the capacity of WECS technology has grown significantly, progressing from just a few kilowatts (kW) to several megawatts (MW) [14][15]. This trend is expected to continue, with a projected increase in global investments in the WECS sector [16]. In recent times, WECSs equipped with PMSG have gained popularity, especially in offshore applications, due to their lack of gearbox and excitation systems [17]. This development is driving the widespread adoption of PMSG based systems in the wind energy industry.

In PMSG-based WECS, a power converter serves as the intermediary between the generator and the electrical network. Various power electronic converter topologies have been proposed for wind turbines, and among them, multilevel converters like the NPC converter are gaining popularity. These multilevel converters offer advantages such as higher voltage levels and reduced stress on the switch system [18][19]. Compared to the 2L-VSC converter, the NPC converter can transfer electrical energy at low to medium voltage using fewer paralleled devices, resulting in lower current draw and a smaller filter [20][21]. However, integrating megawatt-range wind turbines with advanced power electronic converters into the electricity grid introduces new challenges in terms of voltage and frequency control at the Point of Common Coupling (PCC). Addressing these issues is crucial to ensure seamless integration and reliable operation of large-scale PMSG-based WECS with the grid.

The primary focus of research in the field of WECS revolves around developing efficient control techniques to enhance the system's ability to provide and manage both active and reactive power in the grid power system, as highlighted in a study published in [22]. Various control algorithms have been employed for managing PMSG-based WECS to achieve objectives such as maximizing wind turbine output, maintaining a constant DC-link voltage, regulating reactive power injection into the grid, and mitigating current harmonics at the PCC.

Two main categories of control methods are commonly used for PMSG-based wind turbines. In the first category, Maximum Power Point Tracking (MPPT) is carried out by the MSC control, while the GSC control is responsible for managing the DC-link voltage [23][24]. In the second category, the MSC control is responsible for DC-link voltage regulation, while the active power extraction from the wind turbine is adjusted by the GSC [25]. Both cases employ vector control techniques to achieve the necessary control objectives [26]. Vector control allows for precise and efficient control of the PMSG-based WECS, ensuring optimal performance and power delivery to the grid.

1.2 Problem Statement

Numerous research studies have investigated the integration of renewable wind energy with the electrical grid [27][28][29]. However, the rising demand for electricity has put strain on the system, resulting in performance issues and instability, leading to compromised power quality. Power electronics devices are employed to facilitate this integration, often configured in different topologies [30]. However, the commonly used conventional converter (e,g 2L VSC) topologies suffer from drawbacks such as high switching losses, significant harmonic distortion at the output terminal, and the need for additional EMI filters [31].

To address these challenges, researchers propose the use of multi-level converter topologies as a viable alternative to conventional setups. This alternative brings several advantages, including reduced switching losses, improved overall efficiency, and a smaller number of filtering elements. Nevertheless, integrating megawatt-scale wind turbines with advanced power electronic converters into the power grid introduces new complexities related to controlling voltage, frequency, and current at the point of common coupling. These factors can significantly impact the performance of WECS. As such, ongoing efforts are being made to devise efficient control techniques to manage these aspects effectively and enhance the overall performance and stability of the integrated system [30].

To ensure the required system stability and power quality, effective control approach for VSC is essential. Traditional control techniques like virtual flux-oriented control, direct power control, and decoupled VOC use multiple Proportional-Integral (PI) regulators. However, due to system non-linearity and variable fluctuations, these controllers may lead to instability [32]. Additionally, tuning these regulators for optimal gain requires significant effort and time [33][34].

To address these issues, a new control strategy has been developed, incorporating phase lag and lead compensators. Unlike the trial-and-error design of traditional controllers, this approach is based on well-established design methods derived from fundamental principles, resulting in greater accuracy and stability. By using phase lag and lead compensators, the control system becomes more robust and capable of handling the non-linearities and fluctuations of the system variables effectively, thus ensuring better performance and improved power quality for the Voltage Source Converter.

1.3 Aim and Objective

The main aim of this study was to develop and design a control system for a WECS based on a PMSG that is connected to the grid using a 5L NPC voltage source converter. The primary focus was on enhancing the system's stability and power quality, particularly in the face of wind speed variations. The specific objectives defining the scope of this dissertation were as follows:

- Investigate the characteristics and behavior of the proposed WECS-based PMSG system.
- Develop a comprehensive control strategy for the 5L NPC voltage source converter to effectively manage power flow and ensure stable operation.
- Analyze the performance of the control system under varying wind speeds and study its ability to maintain stable power delivery to the grid.
- Evaluate and compare the power quality of the WECS with the 5L NPC converter to traditional control approaches, such as two-level voltage source converters.
- Assess the impact of the control strategy on system efficiency, including reduced switching losses and improved overall performance.
- Investigate the system's response to transient conditions and examine its ability to handle sudden changes in wind speed and power demand.

By achieving these specific objectives, The study aimed to contribute valuable insights into enhancing the stability and power quality of WECS based PMSG systems interfaced to the grid using the 5L NPC.

1.4 Contribution

The main contribution of this study is the adaptation and application of a control strategy previously used in WECS-based PMSG utilizing a Three-Level Neutral Point Clamped (3L NPC) voltage source converters topology [35][36]. In this research, the control strategy is extended to optimize the performance of the 5L NPC converter in wind turbine applications.

The novelty of this contribution lies in the comprehensive evaluation of the proposed control strategy's effectiveness under varying wind conditions, particularly during significant changes in wind turbine speed. While the previous analysis of the 3L NPC VSC primarily focused on the control aspect in a different converter context, this dissertation addresses this limitation and systematically assesses the control strategy's performance in dynamic wind conditions for the 5L NPC converter. By conducting comparative analyses of the THD% between the 5L NPC and the conventional 2L VSC, the research offers valuable insights into the enhanced power quality and stability provided by the 5L NPC VSC topology in the grid integration of WECS.

In conclusion, this study's key contribution is the application and optimization of a previously developed control strategy from WECS-based PMSG with 3L NPC converter to the specific context of the 5L NPC converter. The comprehensive evaluation of the control strategy's performance under varying wind conditions and the comparison with conventional converters contribute to advancing the understanding and practical implementation of the 5L NPC-VSC topology, highlighting its potential for improving power quality and stability in the grid integration of WECS.

1.5 Limitations

At this stage, the research investigation was confined solely to software simulations. The limitation arises from the challenge of accurately modeling the complex interactions within the wind turbine system using software simulations alone. Complex mechanical, aerodynamic, and electrical dynamics may prove difficult to replicate accurately. Consequently, this could lead to discrepancies between simulated outcomes and real-world performance, thereby reducing the reliability of the research findings.

1.6 Research Scope

The implementation of a control system for a WECS-based PMSG connected to the grid using a 5L NPC voltage source converter will lead to enhanced system stability and improved power quality, particularly in response to variations in wind speed. The WECS-PMSG can be categorized as Horizontal Axis Wind Turbines (HAWTs) or Vertical Axis Wind Turbines (VAWTs), as illustrated in Figure 1.1.

For investigating the effectiveness of the variable WECS, horizontal axis turbines are preferred due to their high efficiency compared to vertical-axis turbines [37]. Additionally, horizontal axis turbines have their blades exposed to strong winds, making them suitable for the study's objectives.

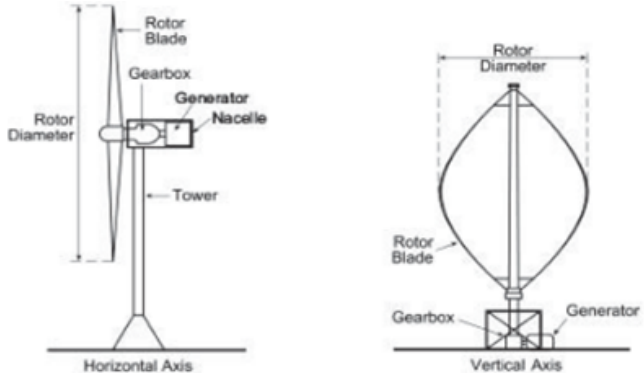

Figure 1.1: Horizontal and Vertical Turbine [1]

The PMSG-derived Type-4 WECS, interconnected with the power grid via a back-to-back VSC system, stands as a highly prospective design within the realm of wind energy [38]. The literature thoroughly covers the suggested methodology [39][40][41]. This investigation focuses primarily on the Type-4 WECS system, illustrated in Figure 1.2.

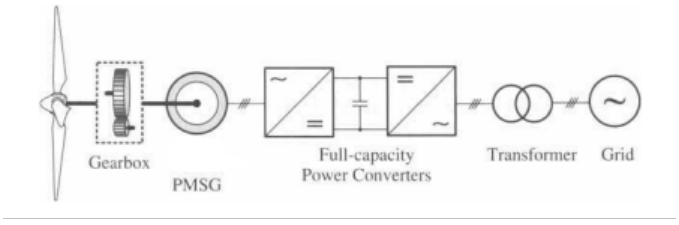

Figure 1.2: WECS based PMSG[1]

1.7 Dissertation Outline

The dissertation is compromises of the following chapters:

Chapter 1: Introduction

The chapter begins with an introduction, providing a concise review of the research's background. It also outlines the problem statement, stating the main issue addressed in the study. Additionally, the chapter highlights the study's objectives and aims, indicating what the research aims to achieve. Furthermore, the chapter discusses the contribution of the study, elaborating on how it adds to the existing body of knowledge. It also acknowledges any limitations that may affect the research's scope or findings. Moreover, the chapter outlines the research's scope, defining the boundaries within which the study will be conducted, specifying the extent of the investigation

Chapter 2: Literature

The chapters offer a comprehensive overview of WECS specifically in the South region. The main focus is on WECS utilizing PMSG, with a detailed exploration of its components and constituent parts. Additionally, the chapters provide a concise explanation of the diverse conversion systems integrated into the setup. Moreover, the chapters provide a brief overview of control techniques employed in such WECS systems.

Chapter 3: Mathematical Model

In the chapter, a detailed model of the WECS based on PMSG is presented. This model elaborates on the intricacies and workings of the entire system. Additionally, the chapter delves into the control model transfer function in-depth, offering a comprehensive explanation of how the control mechanisms function and interact within the WECS-PMSG system.

Chapter 4: Component Sizing

The chapter includes essential information regarding the component size and rating used in the project. It provides a rationale for the selection of each item incorporated into the project, explaining the reasons behind their choices. Additionally, the chapter documents the decisions made during the project's development process, shedding light on the considerations that influenced the final configuration of the components.

Chapter 5: Control Design

In this chapter, the design requirements that the research must meet or achieve are outlined and elaborated upon. These requirements serve as benchmarks to ensure the research's objectives are adequately addressed. Furthermore, the chapter includes a comprehensive

discussion on the design and stability study, specifically focusing on the controller utilized with the generator-side and grid-side converters. The study is conducted using MATLAB software, and Bode plots and step response curves are employed to analyze and assess the controller's performance in the frequency domain.

By employing these analytical tools and methodologies, the chapter aims to gain valuable insights into the stability and effectiveness of the controller in the context of the generator-side and grid-side converters. This analysis helps to ensure the successful functioning of the WECS and the integration with the power grid.

Chapter 6: Simulation

In this chapter, the implementation of the proposed WECS is presented. The system is composed of several subsystems, each serving a specific function in the overall setup.

- The first subsystem is the Wind Turbine block, responsible for capturing and converting the kinetic energy from the wind into mechanical power. This mechanical power is then further converted into electrical power, which is fed into the system.
- The second subsystem is the VSC block. This converter is tasked with converting the electrical power generated by the wind turbine into a stable and controllable form, suitable for integration with the power grid.
- The third subsystem comprises the converter controller blocks, namely the MSC controller and the GSC controller. These controllers are crucial in regulating the power flow and ensuring the efficient operation of the WECS.

By integrating these subsystems together, the proposed WECS aims to harness wind energy effectively and contribute to the power grid in a stable and reliable manner. The chapter delves into the details of how these components are integrated and how they collectively form a functional WECS.

Chapter 7: Results and Discussions

This chapter thoroughly discusses and analyzes the simulation results for the proposed WECS under varying wind speed conditions. It presents the data and findings from the simulations, including performance metrics and key parameters measured during the tests. The chapter offers insightful interpretations and comparisons of the simulation results against the design requirements and objectives outlined earlier. It identifies the strengths and weaknesses of the WECS under specific conditions, while also highlighting any limitations or challenges encountered during the simulations. Visual representations, such as graphs, charts, and plots, aid in understanding the data. Overall, this comprehensive discussion validates the effectiveness and functionality of the proposed WECS design and its control strategies, providing a comprehensive assessment of the system's performance.

Chapter 8: Conclusion

This chapter concludes the project by summarizing the findings and discussions. The system's performance and behavior are assessed, and the achievement of project objectives is evaluated. Recommendations for optimizing the system are based on insights from simulation results and discussions, including adjustments to control strategies, component modifications, and system enhancements. Furthermore, potential applications of the proposed WECS in diverse contexts are explored. The chapter serves as a valuable guide for future researchers and practitioners, offering possibilities for implementing similar WECS systems and adapting the technology for various renewable energy applications. In essence, it provides a comprehensive outlook on the project's outcomes and lays the foundation for potential advancements in renewable energy applications.

Chapter 2

Literature Review

2.1 Overview of WECS in South Africa

South Africa's geographical and size advantages make it conducive for the utilization of diverse renewable energy sources, particularly wind power. The country benefits from a tropical environment, which contributes to its substantial wind energy production. Through global organizations' support, the government has facilitated technical studies and collected factual data on the quantity and quality of renewable energy resources available. Notably, the implementation of the Renewable Energy Independent Power Producers Procurement Program (REIPPPP) has led to a considerable rise in renewable energy projects across South Africa [42].

Eskom is the predominant energy supplier in South Africa, providing 85.8% of the country's energy, primarily generated through coal-fired power stations. Conversely, renewable energy technologies currently account for only 4.5% of the installed capacity. However, the government has allowed the exploration of renewable energy sources through the REIPPPP. Under this initiative, South Africa has seen significant progress in the development of wind energy projects.

As of March 2019, the country had 22 fully operational wind farms with an installed capacity of 2020 MW, and an additional 11 wind farms were under construction, contributing 1391.8 MW of capacity [43]. These developments have been facilitated by the South African Wind Energy Association (SAWEA) study. The REIPPPP is a tender process that encourages grid-connected renewable energy by purchasing clean electrical energy from Independent Power Producers (IPPs). This initiative is critical in diversifying South Africa's energy sources and reducing reliance on coal-based generation. To ensure the smooth integration of Renewable Power Plants (RPPs) into the transmission or distribution grid, the South African Renewable Energy Grid Code (SAREGC) supports the REIPPPP by setting technical standards. This guarantees network stability and power quality for consumers, ensuring a reliable supply of renewable energy [43] [44].

With the ongoing implementation of the REIPPPP, it is expected that wind power production will increase in the near future. Table 2.1 presents a list of large-scale wind farms (>20 MVA) connected to the grid or currently undergoing commissioning [13]. Despite the continued reliance on coal-fired power plants to supply the majority of the country's energy, further research is still needed to study the effects of wind power integration on the utility system.

Table 2.1: Large scale wind farms in South Africa [13]

Wind Farm	MW	Supplier	Status
Dassiesklip	27	Sinovel	In Operation
MetroWind	27	Sinovel	In Operation
Grassridge	60	Vestas	Commissioning
Hopefield	66	Vestas	In Operation
Noblesfontein	74	Vestas	In Operation
Kouga	80	Nordex	Commissioning
Dorper	100	Nordex	In Operation
Sere	100	Siemens	In Operation
Cookhouse	138	Suzlon	Commissioning
Jeffreys Bay	138	Siemens	In Operation

Presently, the efficiency of large synchronous generators plays a significant role in shaping the technical aspects of the electrical grid. It is expected that WECS will fulfill a similar role as current power plants in integrating renewable energy into South Africa's utility grid [45][46]. Ensuring power supply quality is essential for power systems [47]. This quality refers to the ability of WECS to deliver standard system voltage and frequency at the connection point. The primary objective is to minimize power quality differences between the utility grid and the WECS, thereby establishing acceptable levels of compatibility within utility grid power quality regulations. This emphasis on power supply quality is crucial for the successful integration of renewable energy from WECS into the existing utility grid.

2.2 Overview of WECS based PMSG

2.2.1 Energy Conversion Process

The rotation of the rotor is initiated by the impact of the wind, facilitating the conversion of kinetic energy into mechanical energy. As the rotor turns, it drives the attached shaft of the generator, leading to the transformation of mechanical energy into electrical energy [48].

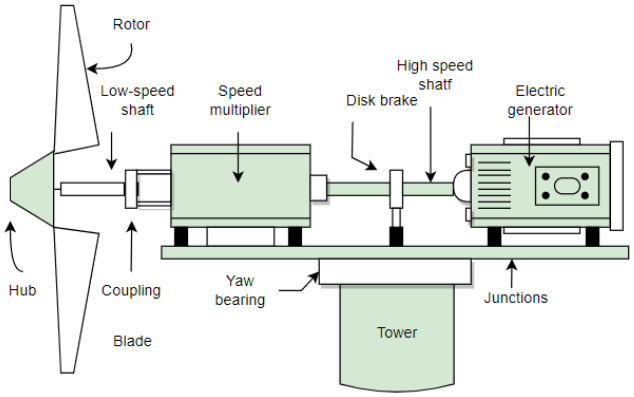

Figure 2.1: Wind Turbine Components [2]

Wind Turbine Structure and their functions

Figure 2.1 depicts the assembled components of the wind turbine, and the corresponding description is provided below [49].

- **Blades**: When kinetic energy is captured, it responds by turning or spinning, which causes the generator's rotor to rotate.
- **Rotor**: Converts kinetic energy into mechanical energy.
- **Electrical generator** : Converts mechanical energy to electrical energy
- **Tower**: Acts as a support for the turbine blades, allowing them to be exposed to the wind so that more wind energy can be captured.
- **Drive-train**: Connects the high-speed shaft and low-speed shaft.
- **Hub**: Gives the gearbox, generator, and other tiny parts a place to be protected.

2.3 Wind Turbine Operating Regions

In Figure 2.2, the operational zones of a Wind Turbine (WT) are illustrated. When the wind speed surpasses the cut-in wind speed, the WT generator initiates the extraction of aerodynamic power from the wind resource. The WT operation ceases when the wind speed reaches the cut-out wind speed [50].

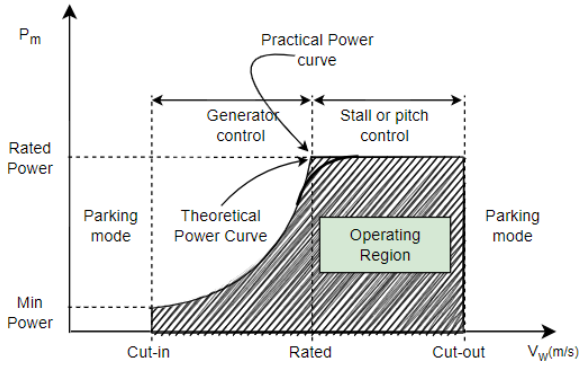

Figure 2.2: Operating regions of a WT [3]

The wind turbine operating regions are summarized as follows:

- **Cut-in speed:**
  The minimum wind speed required for a wind turbine to start generating electricity efficiently. It's the speed at which the turbine begins to produce power.
- **Rated Speed:**
  The wind turbine is operating around the rated rotor speed and rated power.
- **Cut-out:**
  The wind turbine stop working when its reaches the cut-out region.

2.3.1 Maximum Power Point Extraction (MPPT) Algorithms

MPPT based TSR Algorithm

The TSR control method involves adjusting the generator's rotational speed to maintain the TSR at an optimal level, enabling the maximum power extraction from the wind resource [51]. For successful implementation, knowledge of the ideal TSR of the turbine is necessary, along with continuous monitoring or calculation of the wind speed and turbine speed. By employing this approach, the system can effectively produce the highest possible power output [52][53]

Indeed, achieving an optimal value for a wind turbine's TSR is crucial. To calculate the ideal rotor speed, Eq.(2.1) is employed, utilizing the measured wind speed as input. Figure 2.3 illustrates the block diagram for a WECS with TSR control. This control method ensures that the wind turbine operates at its maximum power extraction efficiency by adjusting the rotor speed in response to varying wind conditions [30].

$$\omega_{r\_opt} = \frac{\lambda_{opt} v_w}{r} \tag{2.1}$$

Where,
ω_{r_opt} is the rotor angular speed [rad/s],
v_w is the wind speed upstream of the rotor [m/s] and
r being the radius of the rotor blade [m].

TSR control offers advantages such as increased efficiency, power regulation, and reduced mechanical stresses. However, it requires sophisticated algorithms and real-time monitoring, has limited performance range, and may experience delayed responses due to wind speed changes. Additionally, accurate knowledge of turbine design and wind characteristics is essential for optimal effectiveness.

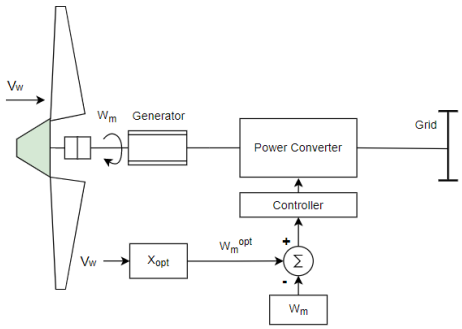

Figure 2.3: The TSR block diagram [2]

MPPT based Optimal Relationship Based (ORB) Algorithm

As stated in [54], understanding the wind turbine's maximum power curve is crucial for monitoring it during ORB control. To obtain this curve, offline simulations or testing on individual wind turbines is required. The wind turbine's mechanical power equation is used in this approach to generate the reference power, utilizing wind speed or rotor speed as input, or referencing the recorded maximum power curve [55].

In Figure 2.4, the ORB controller is depicted, designed to achieve maximum power extraction from the wind turbine. The optimal output power of the wind turbine is determined by Eq.(2.2), which serves as a critical factor in the ORB control strategy for maximizing the system's power generation efficiency.

$$P_{opt} = \frac{1}{2} p A C_{p\_opt} \left(\frac{\omega_{r\_opt} \times r}{\lambda_{opt}} \right)^3 \tag{2.2}$$

$$P_{opt} = K_{opt} \left(\omega_{r\_opt} \right)^3$$

Where,
p Is the air density which equal to 1.225 kg/m^2 at sea level,
A Is the area swept by the rotor blades [m^2] ($A = \pi r^2$).
P_{opt} Is the optimum power constant indicating the ideal power in relation to the optimal rotor speed ω_{r_opt} in [rad/s].

$$K_{opt} = \frac{1}{2} p A C_{p\_opt} \left(\frac{r}{\lambda_{opt}} \right)^3 \tag{2.3}$$

The ORB based MPPT technique in WECS offers advantages such as enhanced power extraction efficiency, fast response to changing wind conditions, reduced mechanical stresses on turbine components, and adaptability to varying wind speeds and loads. However, implementing this approach requires a complex control algorithm, and its effectiveness relies on accurate wind speed data, making it sensitive to wind variability. There is also a risk of potential over-speeding, necessitating careful design and monitoring, along with accurate initial calibration. By carefully considering these factors, the ORB-based MPPT approach can be optimally utilized to efficiently harness wind energy while ensuring safe and reliable WECS operation [56][57].

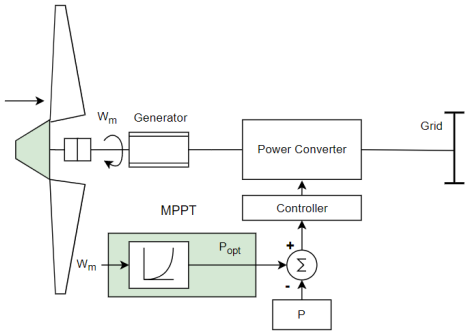

Figure 2.4: The ORB block diagram [2]

Indeed, having knowledge of the wind turbine based MPPT curve is crucial for optimal operation [58]. In[59], the observed rotor speed is utilized to track the optimal power point from the wind turbine's maximum power curve in response to changes in wind speed. Figure 2.5 illustrates the power produced as a function of rotor speeds for various wind speeds, representing the power curve of a typical wind turbine. Understanding and utilizing this curve allows the WT to efficiently harness the available wind energy and operate at its maximum power extraction capability.

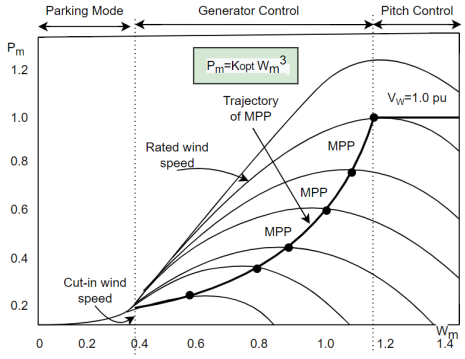

Figure 2.5: Wind Turbine based MPPT curve [4]

2.4 Overview of Transmission VSC-HVDC system

HVDC transmission offers several advantages, including the ability to supply power over long distances and the capability of asynchronous connection using overhead or underground cables. In the past, HVDC transmission relied on thyristors for converting electricity between AC and DC. However, VSC have emerged as a more modern semiconductor technology, replacing thyristors in HVDC systems. VSC-based HVDC transmission provides various benefits compared to traditional HVDC, such as separate power system connection and independent active and reactive power regulation. VSC-HVDC is also utilized in multi-terminal DC systems to change the current direction without altering the DC voltage polarity, without

requiring rapid communication between switching stations [60]. This makes VSC-HVDC a more flexible and advanced solution for efficient power transmission and grid management.

The VSC-HVDC system incorporates advanced high-power, high-frequency semiconductor switches like IGBTs and GTOs, which represent recent technological advancements. These switches are combined with anti-parallel diodes to form a single unit. To achieve the required voltage level and enhance converter redundancy, multiple units are connected in series, creating a valve configuration. The system can dynamically operate these switches using PWM (Pulse Width Modulation) techniques, enabling precise control over the amplitude and phase angle of the generated fundamental (50 Hz) voltage component, as documented in [61]. This capability allows for efficient and flexible high-voltage power transmission and grid management in VSC-HVDC systems [62][63][64].

The VSC is a crucial component in modern power systems, enabling efficient conversion of electrical power between AC and DC. It consists of several key components, including high-power semiconductor switches (such as IGBTs and GTOs), anti-parallel diodes, PWM controllers, DC capacitors, low-pass filters, gate drivers, voltage and current sensors, and a cooling system. The VSC's operation involves precise control of switching frequency and duty cycle through the PWM controller, allowing for accurate adjustment of the AC output voltage's amplitude and phase angle. The VSC technology finds applications in HVDC transmission, renewable energy integration, and power grid stabilization. Researchers continue to explore advancements and improvements to enhance the VSC's performance and efficiency, contributing to the development of modern power systems [30].

The selection of control modes depends on the application and specific needs of the power system at hand. In the context of rectifier and inverter controllers, they adopt any two of the four control strategies mentioned above based on the system's demands and operating conditions. VSC_1 controllers manage active power and reactive power control, while VSC_2 controllers focus on controlling DC voltage and reactive power, as illustrated in Figure 2.6.The detailed mathematical modeling and equations describing a VSC have been discussed in more detail in [5].

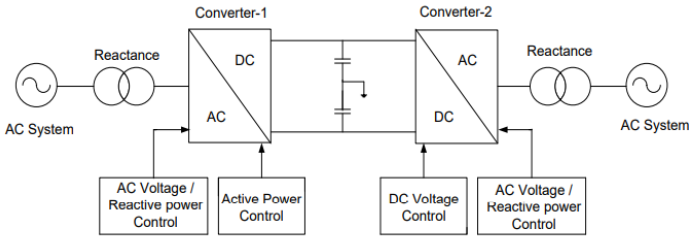

Figure 2.6: VSC Control System [5]

By employing the Sinusoidal Pulse Width Modulation (SPWM) technique, the fundamental AC voltage component's amplitude, phase angle, and frequency can be effectively controlled [63][64]. The fundamental frequency component of the converter's AC voltage output can be determined using Eq. (2.4) when the DC voltage at the converter's DC side, denoted as V_{dc}, remains constant:

$$V_C = \frac{1}{2} V_{dc} M_i \sin(\omega t + \delta) \tag{2.4}$$

Where,
V_{dc} The voltage on the DC side (V), and M_i is the modulating index
δ_1 Phase angle (θ)
ω The angular frequency (rad/s)

From the above equation , it is seen that the VSC-HVDC system depends on the variables M_i, angle δ and frequency which are independently controlled by VSC controllers. The active and reactive power can be controlled by controlling the phase angle δ and the amplitude of the fundamental frequency component of converter AC output voltage V_C respectively [63].

2.5 Modulation Strategy for 5L NPC VSC

In multilayer power conversion applications, various modulation schemes have been utilized. For the NPC multilevel converter, two types of modulation control methods are commonly used: basic switching frequency and high switching frequency PWM. These methods include SPWM, Selective Harmonic Elimination (SHE), and Space Vector Pulse Width Modulation (SVPWM) [65]. Among these, the focus of the study is on SPWM techniques due to their wide applicability and ease of use in harmonic suppression, making them a significant area of investigation.

The modulation index for multilevel converters is given Eq. (2.5).

$$m = \frac{A}{\frac{1}{2}(N-1)A_c} \tag{2.5}$$

Where,
N is number of levels.
The amplitudes of the reference signal and the carrier signal in the SPWM technique are represented by A and Ac , respectively.

In SPWM, there are three main carrier arrangements commonly used to synthesize the gating pulses for the NPC multilevel converter. These arrangements are employed to control the switching of the converter's semiconductor devices, and they play a crucial role in generating the desired output voltage waveform with minimized harmonics and improved performance[66] [67].

2.5.1 Phase Disposition (PD)

In the PD based SPWM method shown in Figure 2.7, the switching function is derived by comparing triangular carriers and sinusoidal reference signals. The carriers are vertically positioned to span the entire voltage range, with each module's carrier covering specific voltage ranges. The first module's carrier covers the range from 0 to V_{dc}, the second module's carrier covers the range from V_{dc} to 2 V_{dc}, and so on. The last module, where N is the total number of modules linked in series, covers the voltage range from $(N-1)$ V_{dc} to N V_{dc}. This technique enables effective control of the multilevel converter, ensuring proper voltage synthesis and harmonics reduction.

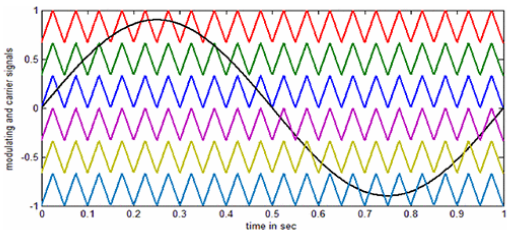

Figure 2.7: Phase Disposition (PD) [6]

2.5.2 Phase Opposition Disposition (POD)

In the POD-SPWM, $(M-1)$ carrier signals are used, where M is the number of output voltage levels. Positive voltage levels have $(M-1)/2$ carrier signals, and negative voltage levels also have $(M-1)/2$ carrier signals. Carrier signals for negative voltage levels are 180 degrees out of phase compared to positive voltage levels. Figure 2.8 illustrates the POD-SPWM concept for a cascaded seven-level multilevel inverter [65]. This technique enables efficient control of the inverter's output voltages, ensuring proper voltage synthesis and reduced harmonics.

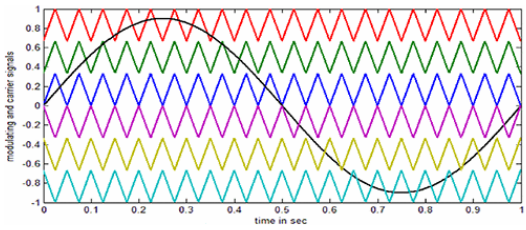

Figure 2.8: Phase Opposition Disposition (POD) [6]

2.5.3 Alternate Phase Opposition Phase Disposition (APOD)

Like the level-shifted systems, the APOD method also uses $(M-1)$ carrier signals [6]. In this technique, each carrier signal is 180 degrees out of phase with its neighboring carrier, as shown in Figure 2.9. This arrangement allows for precise control of the multilevel converter's output voltages, enabling efficient voltage synthesis and harmonic reduction.

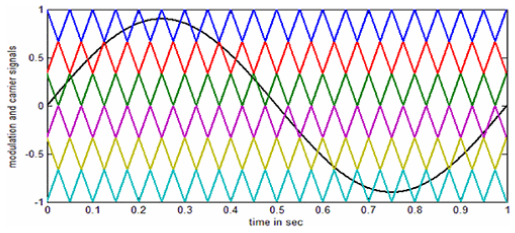

Figure 2.9: Alternate Phase Opposition Phase Disposition [6]

2.6 Power Converters Typologies

The converter's semiconductor switches can be arranged in two different architectures: two-level or multi-level [7]. In the two-level architecture, the switches are organized in a simple, single-level configuration. On the other hand, in the multi-level architecture, the switches are arranged in multiple levels, providing more voltage steps and allowing for finer control of the output voltage waveform. The choice of architecture depends on the specific requirements and applications of the converter.

2.6.1 Two-level Voltage Source Converter

While 2L-VSC topologies are known for their dependability, ease of configuration, and durability, they suffer from significant switching losses and require additional EMI filters to address noise issues [68]. Figure 2.10 depicts the configuration of a 2L-VSC.

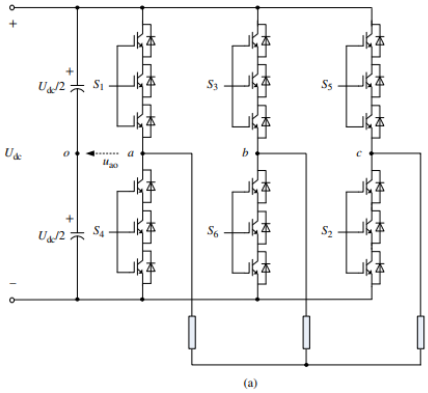

Figure 2.10: Two-level Voltage Source Converter [7]

The literature includes comparisons of the NPC, Flying Capacitor (FC), and Cascaded H-Bridge (CHB) multilevel converter topologies, highlighting their respective advantages and disadvantages [69][70][71][72]. Here's a brief exploration of the benefits and drawbacks of these multilevel converter topologies:

2.6.2 NPC Multilevel Converter

Advantages:
Reduced switching losses, lower voltage stress on switches, and improved efficiency due to the neutral point clamping technique.

Disadvantages:
Higher complexity and increased semiconductor device count, leading to higher costs and more challenging control implementation.

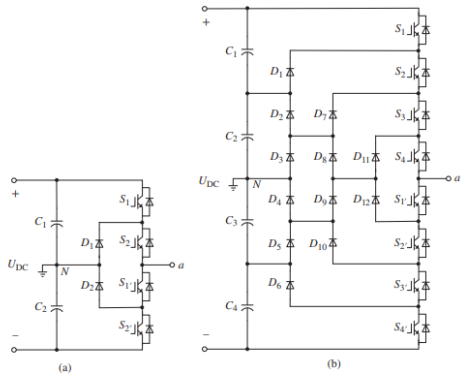

Figure 2.11: Neutral point clamped converter [7]

2.6.3 FC Multilevel Converter

Advantages:
Fewer semiconductor devices required compared to NPC, leading to lower costs and simpler control.

Disadvantages:
Limited scalability due to flying capacitor voltage balancing issues, reduced efficiency, and increased voltage stress on switches.

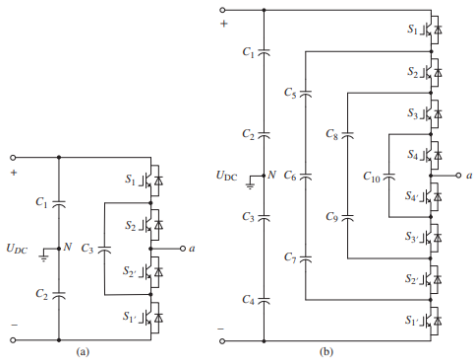

Figure 2.12: Flying capacitor converter [7]

2.6.4 CHB Multilevel Converter

Advantages:
Modular and scalable design, reduced voltage stress on switches, and lower switching losses compared to NPC.

Disadvantages:
Requires a higher number of isolated DC sources, which may result in increased complexity and cost. The choice of multilevel converter topology depends on specific application requirements, cost constraints, scalability needs, and the desired balance between complexity and efficiency.

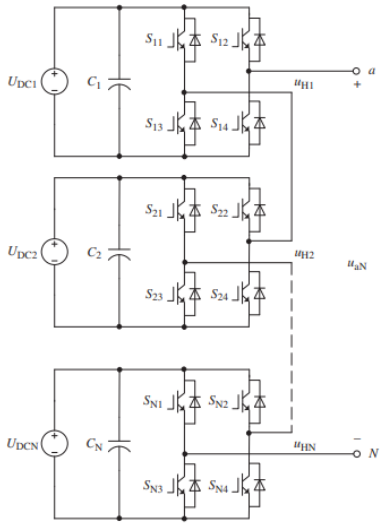

Figure 2.13: Cascade H-bridge Converter [7]

2.7 Control Strategy of a VSC

In grid-connected WECS, sophisticated control methods are employed to regulate power, voltage, and current. The literature [8][73] delves deeper into these strategies. In particular, the author in [74] compared the direct control and vector control approaches. It was demonstrated that while the direct control technique offers fast dynamic response and simplicity, the vector control technique surpasses it in terms of overall performance, fewer current distortions, and a higher grid power factor. The vector control approach's advantages make it a more preferable option for ensuring efficient and stable operation in grid-connected WECS.

2.7.1 Direct Control Strategy

In the direct control technique, the active power can be managed by adjusting the power angle between the converter's basic output voltage and the AC system voltage. On the other hand, reactive power control is achieved by adjusting the magnitude of the VSC voltage relative to the AC system voltage [8]. This control method enables precise regulation of both active and reactive power in grid-connected systems, ensuring efficient and stable operation.

2.7.2 Vector Control Strategy

In the vector control technique, the control of instantaneous active and reactive power is achieved separately in the dq synchronous reference frame. This control method consists of a dual control loop structure, comprising inner and outer current control loops. The external control loops are responsible for regulating the DC-link voltage, AC voltage, and active and reactive power [8]. The output signals from the outer control loops provides $d-q$ reference for the inner current control loop. Figure 2.14 illustrates the vector control scheme integrated with PI controllers, which play a crucial role in achieving precise and stable control of the system.

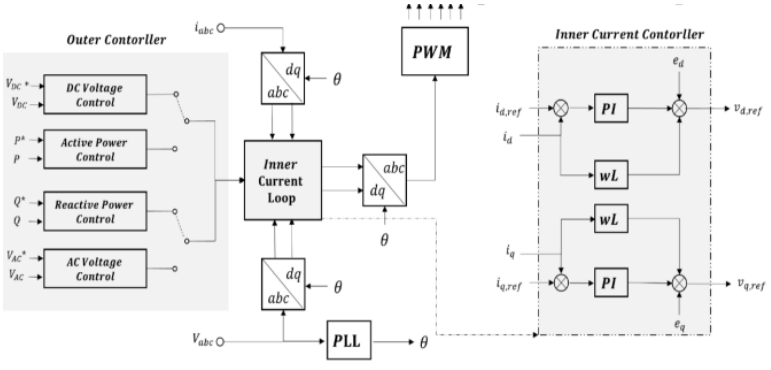

Figure 2.14: Vector Control of VSC with PI controllers [8]

2.8 Fundamental Controllers

In the literature, several control strategies are presented for WECS, including Sliding Mode (SM), Predictive control, Back-stepping, and Neural Network (NN) controllers [75][76][77][78]. These controllers aim to optimize the system's performance and ensure stable operation under various conditions. Widely used controllers in WECS can be categorized into two main groups: PI controllers and Phase-Lag, Phase-Lead compensators [79]. PI controllers are commonly used for simple and straightforward control tasks, while Phase-Lag and Phase-Lead compensators offer more advanced control capabilities, allowing for improved system response and stability. The advantage and disadvantage of this two commonly used control are described as follow :

2.8.1 PI Controllers

Advantages:
PI controllers are advantageous due to their simplicity in design and implementation, providing good stability and steady-state accuracy, and demonstrating robustness in handling system uncertainties and disturbances, making them suitable for a wide range of applications.

Disadvantages:
PI controllers exhibit limited performance in complex systems or applications with strict performance requirements, as they lack advanced control capabilities. Moreover, tuning the PI controller's parameters, such as the proportional and integral gains, can be challenging and may involve trial and error, particularly for complex systems.

2.8.2 Phase-Lag, Phase-Lead Compensators

Advantages:
Phase Lag and Lead compensators provide advanced control capabilities beyond simple PI controllers, resulting in improved transient response and stability. They enhance system performance and response, ensuring more precise control even under challenging conditions.

Disadvantages:
Phase Lag and Lead compensators involve a more complex design process compared to PI controllers, requiring a deeper understanding of control theory. Their implementation may demand more computational resources and effort due to their complexity. The choice between PI controllers and compensators depends on the specific control requirements of the system. PI controllers are well-suited for simple and straightforward control tasks, while compensators are preferred for applications that demand advanced control capabilities and improved performance.

2.9 Total Harmonics Distortion THD

To maintain harmonic emissions within acceptable limits, the IEC 61000-3-6 provides standards for assessing harmonic emissions in electrical networks. For wind farms comprising multiple wind turbine generators, it is crucial to evaluate the cumulative THD at the grid connection point [80][81][82]. PWM is commonly utilized to control the switching mechanism of the generator-side converter and the grid-side inverter in both DFIG and PMSG systems. The output voltage of the grid-side inverter predominantly exhibits sinusoidal-like waveform in bursts [83]. The THD levels in current and voltage waveform are quantified using Eq. (2.6) [84].

$$\mathrm{THD}_i = \frac{1}{i_1}\sqrt{\sum_{h=2}^{\infty}(i_h)^2} \tag{2.6}$$

Where, h denotes the harmonic order.

In the literature, various comparative studies have been conducted [85][86][87], and it has been found that the use of the NPC converter is more advantageous in terms of mitigating THD percentage. Figure 2.15 illustrates the comparison between the two-level and three-level NPC converters.

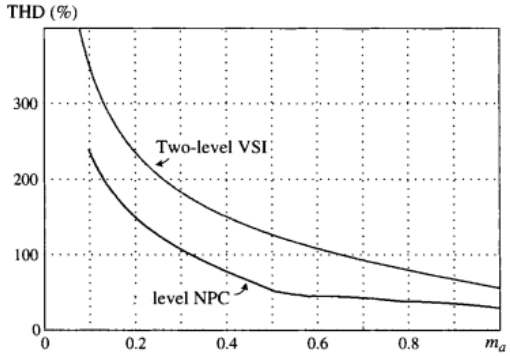

Figure 2.15: THD profile of the output voltage produced by the two-level and three-level NPC converter [9]

2.10 Chapter Summary

This section provides a concise summary review of the components involved in the WECS based on PMSG. Additionally, it outlines the strategy that will be employed to conduct the proposed research investigation.

2.10.1 5L-NPC based HVDC Transmission

The primary objective of this study is to achieve a significant reduction in THD levels at the converter's output terminal. To accomplish this, the 5L NPC architecture is chosen due to its advantages, such as reduced size and number of filtering components, lower harmonic distortion, and decreased losses. Moreover, this converter offers superior waveforms compared to standard topologies and can handle higher voltages. Considering the benefits of an HVDC transmission system, which includes increased transmission capacity, improved system stability, and lower transmission losses, the 5L NPC VSC-based HVDC configuration is deemed suitable for the research investigation.

2.10.2 Vector Oriented Control

Voltage source converters are highly recommended in various applications due to their advantageous characteristics. They provide superior power quality by enabling precise control over current and voltage waveforms, ensuring cleaner and more stable power output with minimized harmonic distortions. VSCs offer higher energy efficiency, reducing energy losses during the conversion process and maximizing the effective delivery of power to the grid or loads. Their advanced control capabilities, such as PWM, enable precise regulation of active and reactive power, enhancing system performance and stability.

Moreover, VSCs' flexibility in voltage control makes them suitable for integrating renewable energy sources with varying voltage characteristics into the grid seamlessly. Additionally, in HVDC transmission systems, VSC-based configurations provide benefits like increased transmission capacity, improved stability, and lower losses, making them a favorable choice for long-distance power transmission and interconnecting power grids. Overall, the combination of enhanced power quality, higher efficiency, advanced control, and grid integration capabilities positions VSCs as a preferred converter technology for modern power systems.

2.10.3 Variable Speed Wind Turbine

At different wind speeds, the VSWT has the ability to generate the maximum power, surpassing the power output of a FSWT. This feature enhances the aerodynamic effectiveness of the WT, as the VSWT can adapt its rotor speed to optimize power production in varying wind conditions. By adjusting its rotor speed to match the wind speed, the VSWT operates at its peak efficiency, leading to increased power generation and improved overall performance compared to fixed-speed WTs that operate at a constant rotor speed regardless of wind conditions.

2.10.4 Optimal Relationship-Based (ORB)

The ORB technique is reliable, has a quick response, is simple and cheaper to implement, and is highly efficient in power smoothing enhancement [53].

2.10.5 Phase Disposition based Pulse Width Modulation

The PD-SPWM technique offers ease of implementation and is highly effective in suppressing harmonics. Moreover, it exhibits lower magnitudes of side-band harmonics compared to the carrier frequency components. This results in significant improvement in the inverter output current waveform, leading to reduced requirements for AC filters. The reduced harmonic content and improved waveform quality contribute to enhanced system efficiency and lower filtering component sizes, making PD-SPWM a favorable choice for applications where harmonic suppression and efficient power conversion are critical.

2.10.6 Phase Lag and Lead Compensators

In contrast to the trial-and-error design approach often used for PI, PD, and PID controllers, the design process for phase-lead and phase-lag compensators is well-established and follows fundamental principles. This structured design methodology allows for precise and accurate results, enabling engineers to achieve the desired control performance more efficiently. By utilizing theoretical principles and control theory concepts, the design of phase-lead and phase-lag compensators can be tailored to meet specific control requirements with high accuracy, making them preferred options for applications where precise control and stability are essential.

Chapter 3

Modelling

3.1 Introduction

This chapter presents a comprehensive dynamic modeling of the WECS based PMSG connected to the grid system through a 5 Level-NPC VSC. The detailed modeling includes the GSC, MSC, and the DC link that interconnects them. The converter's control model and the concept of the wind turbine are also discussed.

Moreover, the chapter derives the open-loop and closed-loop transfer functions of the controllers, providing a thorough understanding of the system's behavior and performance in different operating conditions. This detailed modeling and control analysis contribute to the development of effective control strategies for optimizing power extraction from the wind and ensuring stable and efficient integration of the WECS-PMSG into the grid system.

3.1.1 Wind Turbine Model Drive-Train Mathematical Modeling

The mechanical power extracted from the wind resource by the wind turbine is given by the following equation [88][89] :

$$P_m = \frac{1}{2}\rho A C_p(\lambda, \beta) {v_w}^3, \tag{3.1}$$

Where ρ is the air density which is equal to 1.225 kg/m^3 at sea level, A is the area swept by the rotor blades [m^2] ($A = \pi r^2$, with r being the radius of the rotor blade in m), v_w is the wind speed upstream of the rotor [m/s], and C_p is the aerodynamic power coefficient dependent on the blade-pitch-angle ϑ[deg] and tip speed ratio λ given by the following equation [88][89]:

$$\lambda = \frac{r\omega_r}{v_w}, \tag{3.2}$$

Coefficients	Value
C_1	0.517
C_2	116
C_3	0.4
C_4	5
C_5	21
C_6	0.0068

Table 3.1: Coefficients Parameters

The power coefficient (C_p) is expressed as a function of the TSR, denoted by λ, and the pitch angle β according to Eq. (3.4) and (3.3) [90].

$$C_p(\lambda, \beta) = C_1 \left(\frac{C_2}{\lambda_i} - C_3 \beta^x - C_4 \right) \exp\left(\frac{-C_5}{\lambda_i} \right) + \lambda_i C_6 \tag{3.3}$$

and

$$\frac{1}{\lambda_i} = \frac{1}{\lambda + 0.08\beta} - \frac{0.035}{1 + \beta^3} \tag{3.4}$$

Where, β is the pitch angle of the blade and is measured in degrees. The coefficients parameters are shown in the Table 3.1 above.

The aerodynamic torque T_m is defined as the ratio of the aerodynamic power P_m to the turbine rotor speed ω_r and is given by Eq. (5.13).

$$T_m = \frac{P_m}{\omega_r} \tag{3.5}$$

Eq 3.6 represents the dynamic equation of the wind turbine

$$J \frac{d\omega_m}{dt} = T_e - T_m - F\omega_r \tag{3.6}$$

Where,
J Turbine Inertia [N.m]
T_e Electromagnetic Torque [N.m]
T_m Aerodynamic Torque [N.m]
F Friction of damping coefficient [N.m/s]
ω_r is the rotor angular speed [rad/s].

3.2 5L NPC Converter Operation

The 5L converter employs a NPC topology and consists of three legs for each phase of the 3-phase system. Each leg comprises a pair of semiconductor switches and a pair of diodes. The switches are operated in complementary mode, meaning that only one switch in each pair conducts at a time, while the other remains off. The diodes serve as freewheeling paths for the current flow when the corresponding switch is off, allowing access to the mid-point neutral point of the DC link.

In this 5L NPC converter, there are four voltage levels that can be achieved at the output terminals: positive, neutral, and negative voltages relative to the mid-point of the DC link. By appropriately controlling the switching states of the semiconductor switches, the converter can generate five different voltage levels, providing a higher number of output voltage steps compared to conventional 2-level converters.

Figure 3.1 visually represents the proposed 3-phase 5L NPC converter circuit, showcasing the arrangement of switches, diodes, and the neutral point. The converter is designed to achieve improved voltage quality and reduced harmonic content, making it suitable for high-power applications, such as WECS interfaced with the grid.

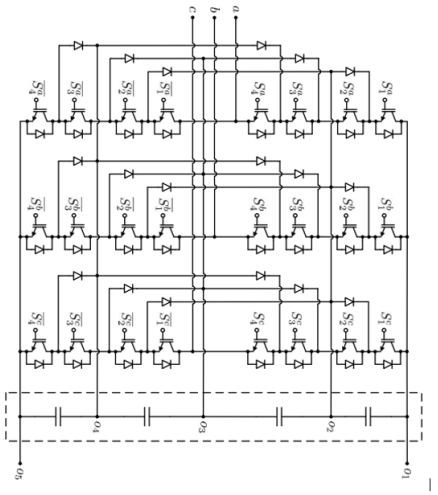

Figure 3.1: Three-phase 5L NPC topology [10]

Table 3.2 Summarizes the five switching states for a phase leg of a 5-level NPC converter.

States	V_{an}	S_{A1}	S_{A2}	S_{A3}	S_{A4}	S_{A5}	S_{A6}	S_{A7}	S_{A8}
1	$2\ V_{dc}$	on	off	on	off	on	off	on	off
2	V_{dc}	on	on	on	off	on	off	off	off
3	0	on	on	on	on	off	off	off	off
4	$-V_{dc}$	on	on	off	on	off	on	off	off
5	$-2\ V_{dc}$	off	on	off	on	off	on	off	on

Table 3.2: Switching states in a phase leg of the 5-level NPC converter [10]

3.3 MSC-side dynamic of 5L-NPC Converter

3.3.1 PMSG Model

The dynamic model of a PMSG is established based on a two-phase synchronous reference frame, where the q-axis is 90° ahead of the d-axis in terms of rotational direction. Figure 3.2 illustrates the $d-q$ reference frame of a salient-pole synchronous machine, which is the reference used for modeling a PMSG [91]. In this reference frame, the d-axis represents the axis of the permanent magnet flux, while the q-axis is the quadrature axis.

The $d-q$ reference frame is commonly used in the analysis and control of PMSGs in wind energy applications. It simplifies the dynamic modeling of the generator and facilitates the implementation of control strategies that ensure efficient power generation and optimal performance. By using this reference frame, the PMSG's behavior can be described in terms of its flux linkage along the d and q axes, making it a valuable tool for understanding and optimizing PMSG-based wind energy conversion system.

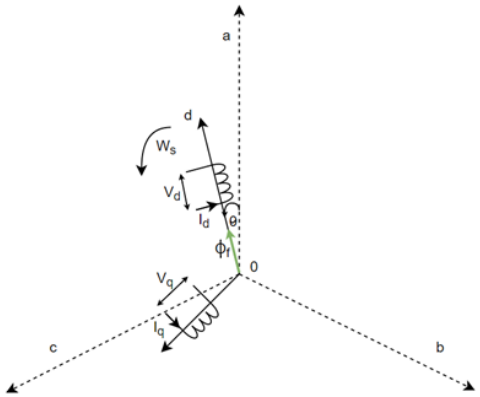

Figure 3.2: $d-q$ axis of a typical PMSG [11]

In the mathematical modeling of a PMSG, common assumptions include the sinusoidal distribution of windings and the neglect of factors such as magnetic saturation, eddy currents, and hysteresis losses. These simplifications make the analysis more tractable and provide a simplified representation of the PMSG's dynamic behavior. The dynamic equation of the PMSG, represented by Eq.(3.7) and (3.8) [92], establishes the relationships between electrical variables, mechanical variables, and the electromagnetic torque.

$$\frac{di_{sd}}{dt} = -\frac{R_s}{L_{sd}} i_{sd} + \omega_e \frac{L_{sq}}{L_{sd}} i_q + \frac{1}{L_{sd}} U_{sd} \tag{3.7}$$

$$\frac{di_{sq}}{dt} = -\frac{R_s}{L_{sq}} i_{sq} - \omega_e \left(\frac{\psi_f}{L_{sq}} + \frac{L_{sd}}{L_{sq}} i_{sd} \right) + \frac{1}{L_{sq}} U_{sq} \tag{3.8}$$

Where,

L_{sdq} The stator self inductance on the d and q -axis [H]
R_s PMSG stator winding resistance [Ω]
U_{sdq} PMSG stator voltage d and q-components (V)
i_{sdq} PMSG stator current d and q-components (A)
ψ_f The flux linkage of the permanent magnet [Wb]
ω_e The electrical angular velocity [rad/s]

Figure 3.3 Shows the equivalent circuits of the PMSG in the dq synchronous rotating reference frame.

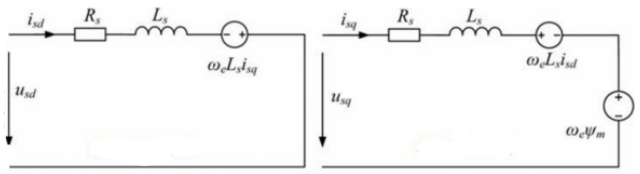

Figure 3.3: d-axis and q-axis equivalent circuits of the PMSG [12]

The electromagnetic torque can be expressed as follows [93]:

$$T_e = \frac{3}{2} N_p \left[\psi_f i_{sq} + \left(L_{sd} - L_{sq} \right) i_{sd} i_{sq} \right] \tag{3.9}$$

Where N_p represents the number of pole pairs in the rotor and ω_e is the rotor's mechanical rotational speed and T_e is the Electromagnetic Torque [N.m]

When considering a surface-mounted PMSG, the electromagnetic torque (T_e) can be simplified further by assuming that the d-axis and q-axis inductance are equal ($L_{sd} = L_{sq}$). Consequently, the equation representing the electromagnetic torque can be expressed as Eq.(3.10).

$$T_e = \frac{3}{2} N_p \left[\psi_f i_{qs}\right] \tag{3.10}$$

3.4 GSC-side dynamics of 5L-NPC Converter

The equation describing the AC-side dynamics of the NPC converter's GSC is given by Eq.(3.11) [94].

$$\frac{d}{dt}\begin{bmatrix} i_a \\ i_b \\ i_c \end{bmatrix} = \begin{bmatrix} \frac{V_{a_{conv}} - V_{a_{grid}}}{L_{grid}} \\ \frac{V_{b_{conv}} - V_{b_{grid}}}{L_{grid}} \\ \frac{V_{c_{conv}} - V_{b_{grid}}}{L_{grid}} \end{bmatrix} - \begin{bmatrix} \frac{R_{grid}}{L_{grid}} & 0 & 0 \\ 0 & \frac{R_{grid}}{L_{grid}} & 0 \\ 0 & 0 & \frac{R_{grid}}{L_{grid}} \end{bmatrix} \begin{bmatrix} i_a \\ i_b \\ i_c \end{bmatrix} \tag{3.11}$$

Where,

$V_{abc_{conv}}$	The converter's output voltages for each phase ($\mathrm{V}_{a_{conv}}, V_{b_{conv}}, V_{c_{conv}}$)
$V_{abc_{grid}}$	Grid voltages for each phase ($\mathrm{V}_{a_{grid}}, V_{b_{grid}}, V_{c_{grid}}$)
i_{abc}	Grid phase current(A)
R_{grid}	Grid resistance (Ω)
L_{grid}	Grid inductance of the interfacing reactor(H)

To obtain the dq version of Eq 3.11, Park transformation is applied to it. Firstly, the equation is rewritten in a compact matrix form as shown in Eq.(3.12) [95].

$$L_{grid} I_{Ident} \frac{di_{abc}}{dt} = V_{abc_{conv}} - V_{abcc_{grid}} - R_{grid} I_{Ident} i_{abc} \tag{3.12}$$

Where, I_{Ident} represents the identity matrix given by Eq 3.13

$$I_{Ident} = \begin{bmatrix} 1 & 0 & 0 \\ 0 & 1 & 0 \\ 0 & 0 & 1 \end{bmatrix} \tag{3.13}$$

When the Park Transformation is applied, and the zero sequence is omitted, Eq. 4.6 transforms into the following equation.

$$\begin{bmatrix} L_{grid} & 0 \\ 0 & L_{grid} \end{bmatrix} \begin{bmatrix} \frac{di_d}{dt} \\ \frac{di_q}{dt} \end{bmatrix} \tag{3.14}$$

$$= \begin{bmatrix} V_d - V_{d_{grid}} \\ V_q - V_{a_{grid}} \end{bmatrix} - \begin{bmatrix} R_{grid} & 0 \\ 0 & R_{grid} \end{bmatrix} \begin{bmatrix} i_d \\ i_q \end{bmatrix} - \begin{bmatrix} 0 & -\omega L_{grid} \\ \omega L_{grid} & 0 \end{bmatrix} \begin{bmatrix} i_q \\ i_d \end{bmatrix}$$

The final equations defining the NPC's AC-side dynamics in the dq reference frame are represented by Eq.(3.15) and (3.16).

$$\frac{di_d}{dt} = \frac{V_d - V_{d_{grid}} - R_{grid}i_d + \omega L_{grid}i_q}{L_{grid}} \tag{3.15}$$

$$\frac{di_q}{dt} = \frac{V_q - V_{q_{grid}} - R_{grid}i_q + \omega L_{grid}i_d}{L_{grid}} \tag{3.16}$$

Applying the $d-q$ axis theory, the instantaneous real and reactive power exchanged between the grid-side converter and the grid can be described using Eq. (3.17).

$$P_{grid} = \frac{3\left(V_{d_{grid}}i_d + V_{q_{grid}}i_q\right)}{2} \tag{3.17}$$

$$Q_{grid} = \frac{3\left(V_{q_{grid}}i_d - V_{d_{grid}}i_q\right)}{2} \tag{3.18}$$

In VOC, the d-axis of the synchronous reference frame is aligned with the grid voltage vector. Consequently, the grid voltage vector only has the d-axis component denoted as $V_{d_{grid}} = V$, while the q-axis component $V_{q_{grid}}$ is set to zero. Thus, we have $V_{d_{grid}} = V$ and $V_{q_{grid}} = 0$. As a result, Eq. (3.19) and (3.20) can be expressed more precisely.

$$P_{grid} = \frac{3\left(V_{d_{grid}}i_d\right)}{2} \tag{3.19}$$

$$Q_{grid} = \frac{3\left(V_{d_{grid}}i_q\right)}{2} \tag{3.20}$$

3.5 DC-side dynamics of 5L -NPC Converter

The DC-side dynamics of the 5-level NPC converter can be described by the following equations:

$$c\frac{dv_{c1}}{dt} = \frac{1}{2}(i_{c1} + i_{d1}) - \frac{v_{c1}}{r}, \tag{3.21}$$

$$c\frac{dv_{C2}}{dt} = \frac{1}{2}(i_{c2} + i_{d2}) - \frac{v_{C2}}{r}, \tag{3.22}$$

$$c\frac{dv_{C3}}{dt} = \frac{1}{2}(i_{c3} + i_{d3}) - \frac{v_{C3}}{r}, \tag{3.23}$$

Where v_{c1}, v_{c2} and v_{c3} are the capacitor voltages of the NPC converter, i_{c1}, i_{c2} and i_{c3} are the currents flowing into the capacitors, i_{d1}, i_{d2} and i_{d3} are the currents flowing into the diodes, c is the capacitance of the capacitors and r is the equivalent resistance of the DC-side circuit. The equations above describe the voltage dynamics of the capacitors and their charging and discharging processes in the DC-side of the 5-level NPC converter, which play a crucial role in maintaining the DC-link voltage stability and the overall converter performance.

When power losses are neglected, the power balance between the DC and AC sides of the converter can be expressed as follows:

$$P_{dc} = P_{ac}, \tag{3.24}$$

Where P_{dc} is the power flowing into the DC-side of the converter, and P_{ac} is the power flowing into the AC-side of the converter. In a 5-level NPC converter, the power flowing into the DC-side is the sum of the power absorbed by the equivalent capacitors:

$$P_{dc} = \frac{1}{2}(v_{c1}i_{c1} + v_{c2}i_{c2} + v_{c3}i_{c3}), \tag{3.25}$$

$$I_{dc} = \frac{1}{2}(i_{c1} + i_{c2} + i_{c3}), \tag{3.26}$$

Where I_{dc} is the DC current flowing into the DC-side of the converter, and i_{c1}, i_{c2}, and i_{c3} are the currents flowing through the equivalent capacitors c_1, c_2, and c_3, respectively.

3.6 Control Model of 5L-NPC Converter

This study focuses on the implementation of a proposed control strategy for WECS based PMSG. The control strategy is applied to regulate both the MSC and the GSC in a 5L NPC voltage source converter. Additionally, the study incorporates VOC to achieve precise control over the system's performance and response. Figure 3.4 shows the detailed control block diagram of the generator-side and grid-side converters.

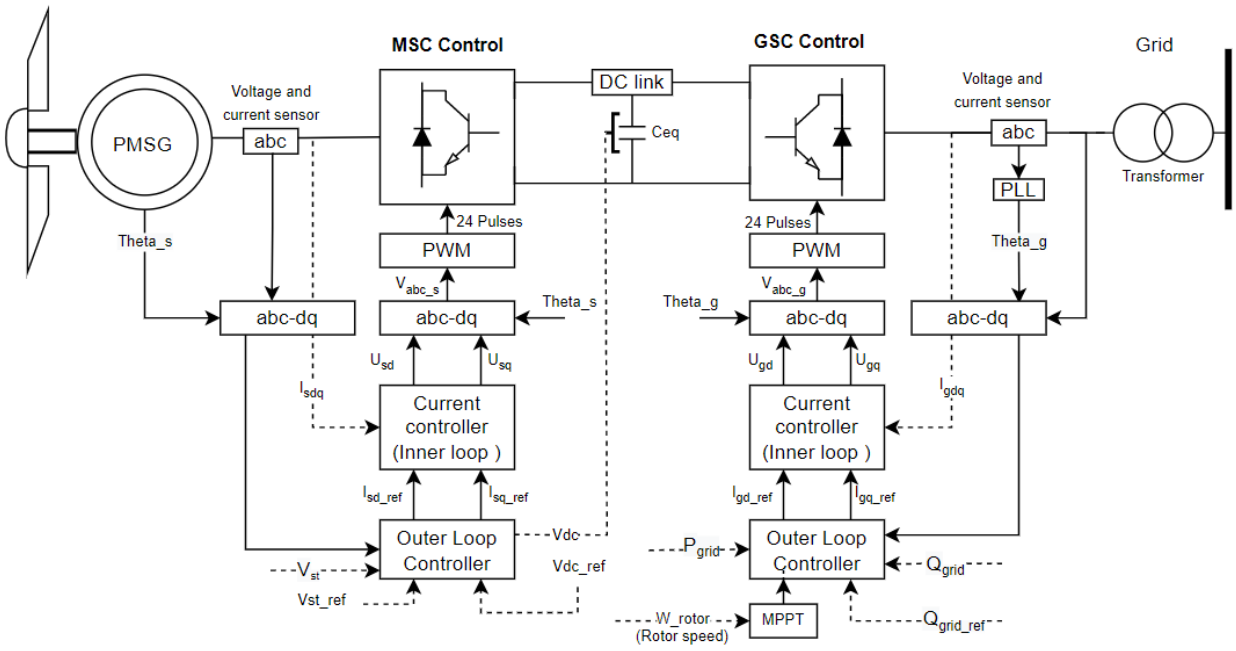

Figure 3.4: Detailed generator-side and grid-side converter control block

As depicted in Figure 3.5, the converter station is controlled through an overall control block, which comprises two main control loops: a fast inner current control loop and a slower outer control loop. The outer control loops are responsible for generating the current reference signals, which serve as inputs to the inner control loops. This hierarchical control structure enables precise regulation and coordination of the converter station's operation, ensuring optimal performance and stability of the WECS.

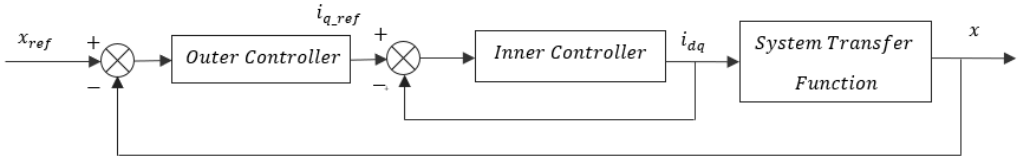

Figure 3.5: Overall Control Block

3.6.1 MSC Control Model

Controller Objective

The MSC controller plays a crucial role in maintaining the required DC-link voltage, ensuring a consistent flow of active power from the WT generator to the grid. By keeping the stator voltage of the generator constant at its rated value, the controller prevents the occurrence of over-voltages, ensuring safe and reliable operation. The MSC control loop consists of both an inner current control loop and an outer control loop, working in tandem to achieve precise regulation and coordination of the converter's operation, thereby optimizing the performance and stability of the WECS.

Inner Current Control

The time constant, arising from the switching of the converter switches, introduces a time delay in the control system. Its transfer function is expressed as shown in Eq. (3.27) [93]. This time delay can affect the overall response and stability of the system, and its proper consideration in the control design is essential to ensure accurate and efficient operation of the WECS-PMSG.

$$T_a(s) = \frac{1}{sT_a + 1} \tag{3.27}$$

$$V_{sdq} = \frac{U_{sdq}}{sT_a + 1} \tag{3.28}$$

The system block is described by Eq. (3.28), where U_{sdq} represents the output of the converter, and V_{sdq} serves as an input to the inner loop transfer function. Consequently, the transfer function of the inner current loop is given by Eq 3.29. This inner current control loop is responsible for regulating the current flowing through the converter, ensuring accurate and stable control of the machine-side currents in the WECS based PMSG.

$$V_{sdq} = \left(i_{sdq\_ref} - i_{sdq}\right) \frac{G_{c\_inner}(s)}{sT_a + 1} \tag{3.29}$$

The stator voltage and current of the PMSG in the dq-axis synchronous reference frame are represented by Eq. (3.30) and Eq. (3.31) respectively. The d-axis voltage equation contains a speed or frequency-induced term $\omega_e \left(L_{sq} i_{sq}\right)$, while the q-axis voltage equation includes both a speed or frequency-induced term and a flux-induced term $\omega_e \left(L_{sd} i_{sd} + \psi_r\right)$, allowing for cross-coupling between the two axes.

$$V_{sd} = R_s i_{sd} - \omega_e \left(L_{sq} i_{sq}\right) + \frac{d}{dt}\left(L_{sd} i_{sd}\right) \tag{3.30}$$

$$V_{sq} = R_s i_{sq} + \omega_e \left(L_{sd} i_{sd} + \psi_r\right) + \frac{d}{dt}\left(L_{sq} i_{sq}\right) \tag{3.31}$$

To achieve effective control performance, decoupling of the $d-q$ axis is essential. This is typically achieved by employing a dual-closed-loop direct current controller with decoupled current compensation and voltage feed-forward compensation [96]. To derive Eq. (3.30), modifications are made to Eq. (3.28) to eliminate the cross-coupling terms.

$$U_{sd} = \left(i_{sd\_ref} - i_{sd}\right) G_{C\_inner}(s) - \omega_e \left(L_{sq} i_{sq}\right) \tag{3.32}$$

$$U_{sq} = \left(i_{sq\_ref} - i_{sq}\right) G_{c\_inner}(s) + \omega_e \left(L_{sd} i_{sd} + \psi_f\right) \tag{3.33}$$

By substituting Eq. (3.29) into (3.33) and (3.32), we obtain Eq. (3.34) and (3.35).

$$V_{sd} = \left(i_{sd\_ref} - i_{sd}\right) G_{c\_inner}(s) - \frac{\omega_e \left(L_{sq} i_{sq}\right)}{sT_a + 1} \tag{3.34}$$

$$V_{sq} = \left(i_{sq\_ref} - i_{sq}\right) G_{c\_inner}(s) + \frac{\omega_e \left(L_{sd} i_{sd} + \psi_f\right)}{sT_a + 1} \tag{3.35}$$

By equating Eq. (3.31) and (3.30) to (3.34) and (3.35), the cross-coupling terms are cancelled, yielding the system's transfer function for both $d-q$ axes. The dynamic transfer function is then obtained by applying the Laplace transformation, as given in Eq. (3.36) and (3.37).

$$\frac{i_{sd}(s)}{V_{sd}(s)} = \frac{1}{sL_{-sd} + R_s} \tag{3.36}$$

$$\frac{i_{sq}(s)}{V_{sq}(s)} = \frac{1}{sL_{-sq} + R_s} \tag{3.37}$$

As a result, Eq. (3.38) represents the open-loop transfer function of the inner current controller.

$$G_{op\_inner}(s) = \frac{G_{c\_inner}(s)}{\left(sT_a + 1\right)\left[s\left(L_{sdq}\right) + R_s\right]} \tag{3.38}$$

The closed-loop transfer function is given by Eq. (3.39).

$$G_{cl\_inner}(s) = \frac{G_{c\_inner}(s)}{\left(sT_a + 1\right)\left[s\left(L_{sdq}\right) + R_s\right] + G_{c\_inner}(s)} \tag{3.39}$$

The complete controller block for the inner current control is as shown in Figure 3.6

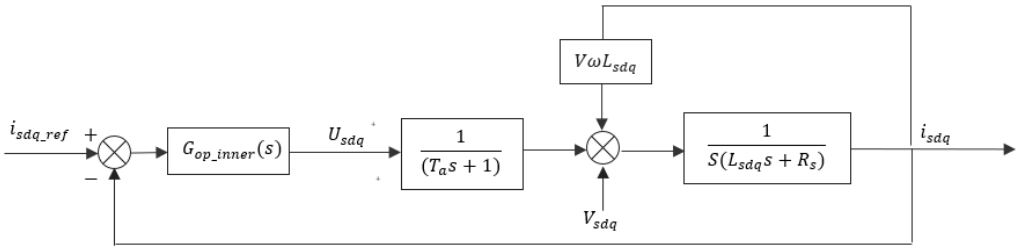

Figure 3.6: Inner current control for MSC-block diagram

Outer Control Loop

To achieve effective control performance and ensure stability, the inner control loop should have a faster response than the outer control loop in a cascaded control system. The outer control loop typically regulates the current, which changes at a relatively slower rate compared to the inner control loop that regulates voltage or power. To avoid instability and oscillations in the overall control system, the triggering frequency of the inner control loop is set to be faster than the outer control loop.

By setting the triggering frequency of the outer loop to be 1/4th of the inner loop frequency, it ensures that the outer control loop can respond quickly to changes in the system and adjust the reference signals for the inner loop accordingly. This helps in achieving better overall system performance and stability, as the inner control loop can follow the changes in the reference signals effectively without excessive oscillations or delays. In this way, the cascaded control system maintains a balance between fast response and stability, leading to optimal control of the wind energy conversion system.

DC Voltage Control Loop

The DC link dynamics can be described by the following Eq. (3.40).

$$\frac{1}{2}C_{dc}\frac{dW}{dt} = \Delta P_{dc} \tag{3.40}$$

Where,
C_{dc} DC-link Capacitance [F]
ΔP_{dc} DC Power is the power flow in the dc side [W].
W is the energy stored in the cap [J].

In an ideal scenario with lossless power flow on the DC-side and constant DC voltage, the active power supplied by the AC side must be equal to the power flowing through the DC-side. This ensures efficient energy conversion and stable system operation.

$$P_{gen} = P_{dc} \tag{3.41}$$

Therefore,

$$I_{dc} = \frac{3}{2}\frac{V_{sd}}{V_{dc}} i_{sd}$$

Equation (4.29) becomes;

$$C\frac{dV_{dc}}{dt} = \frac{3}{2}\frac{V_{sd}}{V_{dc}} i_{sd} - I_L$$

The system transfer function primarily focuses on i_{sd} as the relevant input, while I_L functions as a disturbance. Thus, the detailed simplified equation can be found in [31]. Consequently, the transfer function of the system is represented by 3.42.

$$C\frac{d\Delta V_{dc}}{dt} = \frac{3}{2}\frac{V_{sd}}{V_{dc\_ref}} \Delta i_{sd} \tag{3.42}$$

Taking the Laplace transform of Eq. (3.42) gives Eq. (3.43) that relates the d-component of the stator current to the DC-link voltage.

$$Cs\Delta V_{dc}(s) = \frac{3}{2}\frac{V_{sd}}{V_{dc\_ref}} \Delta i_{sd}(s), \quad \frac{\Delta V_{dc}}{\Delta i_{sd}(s)} = \frac{3}{2}\frac{V_{sd}}{V_{dc\_ref}} \times \frac{1}{Cs} \tag{3.43}$$

Therefore, the open-loop transfer function of the DC link dynamics can be represented as shown in Eq. (3.44):

$$G_{Vdc\_outer\_ol}(s) = G_{Vdc\_outer}(s) \times G_{cl\_inner}(s) \times \frac{3}{2}\frac{V_{sd}}{V_{dc\_ref}} \times \frac{1}{Cs} \tag{3.44}$$

$$G_{Vdc\_outer\_ol}(s) = \frac{3V_{sd}G_{Vdc\_outer}(s)G_{cl\_inner}(s)}{2V_{dc\_ref}Cs\left[(sTa+1)(sL_{sd}+R_s) + G_{cl\_inner}(s)\right]}$$

Thus, the closed-loop transfer function of the DC-link voltage controller can be expressed as Eq. (3.45).

$$G_{Vdc\_outer\_cl}(s) \tag{3.45}$$

$$= \frac{G_{Vdc\_outer}(s)G_{c\_inner}(s)}{2V_{dc\_ref}Cs\left[(sT_a+1)(sL_{sdq}+R_s) + G_{cl\_inner}(s)\right] + 3V_{sd}G_{Vdc\_outer}(s)G_{cl\_inner}(s)}$$

The complete control block of the DC-link voltage controller is illustrated in Figure 3.7.

The inner current closed-loop transfer function is given by Eq. (3.55).

$$G_{cl\_inner}(s) = \frac{G_{c\_inner}(s)}{(sT_a+1)\left[s\left(L_{sdq}\right)+R_s\right] + G_{c\_inner}(s)} \tag{3.46}$$

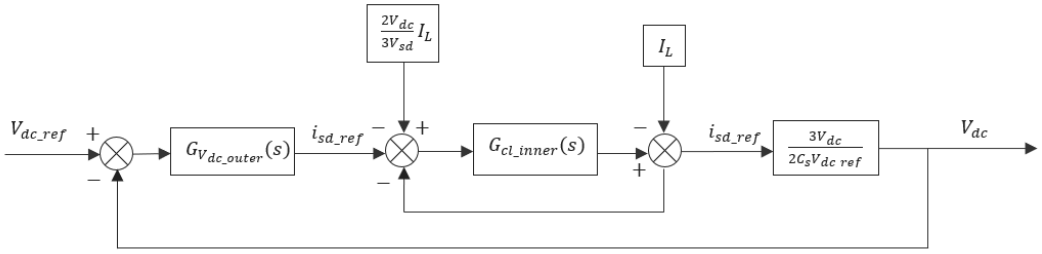

Figure 3.7: DC Outer Voltage Control block

3.6.2 Stator Voltage Control Loop

The stator control block is represented by the Eq. (3.47).

$$\Delta V = V_{st} - V_{conv} = \frac{R_s P_{gen} + X_s Q_{gen}}{V_{st}} \tag{3.47}$$

Where:
V_{st} Stator voltage (V)
V_{conv} Converter voltage (V)
X_s The synchronous reactance equal to: $\omega_e(L_{sd} + L_{sq})$ (H)

In this scenario, assuming that R_s is smaller than X_s, the stator reactance, the voltage drop across the stator reactance is primarily determined by the reactive power flow. Thus, the detailed simplified equation can be found in [31].

Therefore the Eq. (3.48) represents the closed-loop transfer function of the stator voltage controller.

$$G_{Vst\_outer\_cl}(s) \tag{3.48}$$
$$= \frac{-3\left[X_s + V_{conv}\right] G_{Vst\_outer}(s) G_{cl\_inner}(s)}{2\left[(sT_a + 1)\left[sL_{sq} + R_s\right] + G_{cl\_inner}(s)\right] - \left[3X_s + V_{conv}\right] G_{Vst\_outer}(s) G_{cl\_inner}(s)}$$

The complete control block of the stator voltage controller is illustrated in Figure.

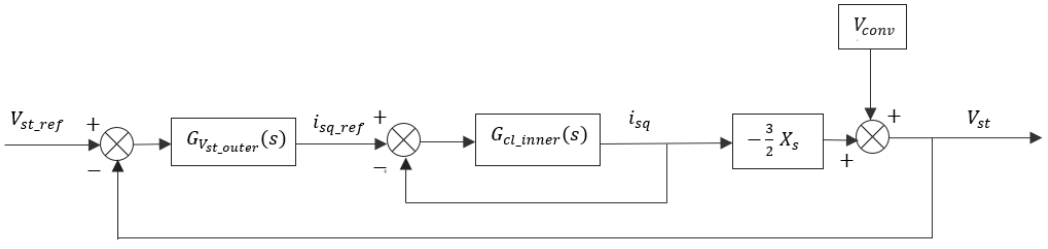

Figure 3.8: Stator Voltage Control block

3.6.3 GSC Control Model

Controller Objective

The GSC controller is responsible for two main tasks: maximizing power extraction from the wind source during low wind speed conditions and regulating the reactive power injected into the grid to maintain a unity power factor.

Inner Current Control

The transfer function of the GSC inner current controller is derived similarly to that of the MSC, with some variations in the parameters used. The closed-loop transfer function is given by Eq. (3.49).

$$G_{c\_inner\_cl}(s) = \frac{G_{c\_inner}(s)}{(sT_a + 1)\left[s\left(L_g\right) + R_g\right] + G_{c\_inner}(s)} \tag{3.49}$$

Outer Control Loop

Active Power

The ORB control technique is employed for MPPT, offering quick response, power smoothing, simplicity, and efficiency. By continuously adjusting the rotor speed (ω_r) based on changes in wind speed (V_w), the ORB control technique ensures the turbine operates at its optimal power output. The ideal power with respect to the rotor speed can be calculated using this approach.

$$P_{opt} = \frac{1}{2} p A C_{p\_opt} \left(\frac{\omega_{r\_opt} \times r}{\lambda_{opt}} \right)^3 \tag{3.50}$$

The optimal power generated from the MPPT, denoted as P_{opt}, is used as an input into the active power control loop. The outer controller ($G_{P\_outer\_cl}(s)$) block generates the d-component of the reference current, which is then fed into the inner current control loop. The transfer function of the active power is represented by Eq. (3.51).

$$G_{P\_grid}(s) = \frac{3}{2} V_{gd} \tag{3.51}$$

The active power controller's closed-loop transfer function is described by the Eq. (3.52):

$$G_{P\_outer\_cl}(s) = \frac{3 G_{P\_outer}(s) G_{cl\_inner}(s) V_{gd}}{3 G_{P\_outer}(s) G_{cl\_inner}(s) V_{gd} + 2} \tag{3.52}$$

Figure 3.9 shows the active power control block.

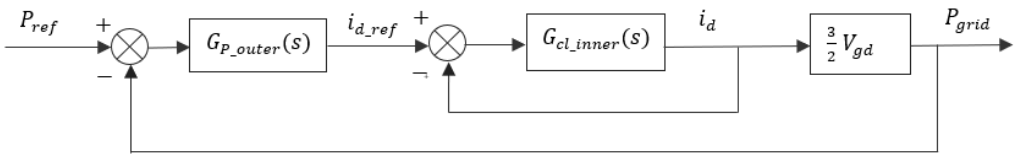

Figure 3.9: Active Power Control Block

Reactive Power

The transfer function of the reactive power is given Eq. (3.53):

$$G_{Q_{grid}}(s) = -\frac{3}{2}V_{gd} \tag{3.53}$$

The detailed simplified equation can be found in [31]. Therefore, the reactive power controller's closed-loop transfer function is provided by Eq. (3.54):

$$G_{Q_{grid}-ol}(s) = -\frac{3G_{Q\_outer}(s)G_{c\_inner\_cl}(s)V_{gd}}{3G_{Q\_outer}(s)G_{c\_inner-cl}(s)V_{gd} + 2} \tag{3.54}$$

Figure 3.10 shows the reactive power control block.

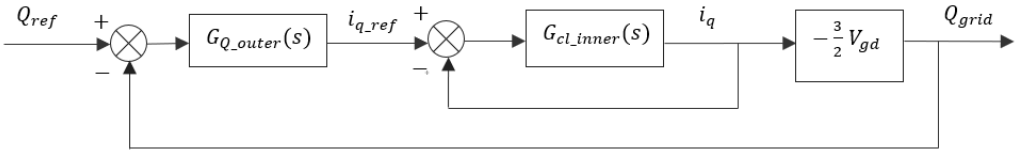

Figure 3.10: Reactive Power Control Block

The inner current closed-loop transfer function is given by Eq. (3.55).

$$G_{cl\_inner}(s) = \frac{G_{c\_inner}(s)}{(sT_a + 1)\left[s\left(L_{sdq}\right) + R_s\right] + G_{c\_inner}(s)} \tag{3.55}$$

3.7 Chapter Summary

The open-loop and closed-loop transfer functions derived in this chapter will be utilized to analyze and evaluate the initial performance of the proposed wind energy conversion system. By developing suitable controllers and integrating them into the system, its performance will be enhanced, meeting the required specifications and ensuring optimal operation. The following chapters will delve into the detailed design and implementation of the controllers, focusing on improving the system's stability, efficiency, and power extraction capability from the wind source. Through rigorous analysis and simulation, the proposed control strategies will be validated, demonstrating their effectiveness in achieving the desired system performance and contributing to the advancement of wind energy conversion technology.

Chapter 4

Component Sizing

4.1 Introduction

In this chapter, the sizing and rating of each component used in the project are presented along with the reasoning and justification behind the choices made. Various engineering trade-offs are carefully considered with the aim of achieving improved system performance and efficiency. The selection of appropriate component sizes and ratings is crucial to ensure the system operates optimally and meets the specified requirements. Factors such as power capacity, voltage ratings, thermal considerations, and cost-effectiveness are taken into account during the component sizing process. By thoroughly evaluating these trade-offs and making informed decisions, the chapter aims to provide a comprehensive overview of the design process and demonstrate how the chosen component specifications contribute to enhancing the overall performance of the project.

4.2 WECS Component Sizing

4.2.1 Wind Turbine Specifications

The choice of a variable-speed wind turbine with a rated capacity of 2 MW and a direct linkage to a PMSG is well-justified on several reasons. The employment of a gear-less drive train enhances efficiency by minimizing mechanical failures and reducing maintenance requirements, thus ensuring improved reliability and operational uptime. Additionally, PMSGs offer superior efficiency and reduced weight compared to conventional generator technologies like induction generators, owing to the absence of rotor copper losses and the elimination of additional excitation systems. Despite these advantages, the selected setup maintains high power generation capabilities with its 2 MW rated capacity, ensuring the wind turbine system can reliably meet the demands of its intended application or grid connection. This comprehensive integration of efficiency, maintenance reduction, and high power generation capabilities underscores the rationale behind choosing the variable-speed wind turbine with a direct linkage to a PMSG.

According to literature, the rating of the direct-driven wind turbine based on PMSG is as follows:

Table 4.1: Wind Turbine Specifications

Parameters	**Value**	**Per Unit**
Rated Mechanical Power (P_m)	2.0 MW	1.0 pu
Cut-in wind speed (m / s)	4	1.0 pu
Rated wind speed (m / s)	12	1.0 pu
Cut-out wind speed (m / s)	25	1.0 pu
Number of rotor blades	3	
Length of blades (m)	37.5	1.0 pu
Rotor diameter (m)	76.42	1.0 pu
Rotor area (m^2)	4587	1.0 pu
Speed range (rpm)	13-21.9	1.0 pu
Rated speed (rpm)	19	
Rotor mass (rpm)	40	

4.2.2 PMSG Parameters

Table 4.2: Permanent Magnetic Synchronous Generator

Parameters	**Value**	**Per Unit**
Rated Mechanical Power (P_s)	2.0MW	1.0pu
Rated Apparent Power (S_s)	2.2419MVA	1.0pu
Rated Line to Line Voltage (V_{l-l})	690 V(rms)	
Rated Phase Voltage (V_s)	398.4 V(rms)	1.0pu
Rated stator Current (I_s)	1867.76 A(rms)	1.0pu
Rated stator Frequency (F_s)	9.75 Hz	1.0pu
Rated Power Factor (PF_s)	0.8921	1.0pu
Rated Rotor Speed (ω_{m})	22.5(rpm)	0.4538pu
Number of Poles (P)	26	0.00387pu
Rated Mechanical Torque (T_m)	848.826kN $\cdot$ m	0.4538pu
Rated Rotor Flux Linkage (λ_{r})	5.8264 Wb(rms)	
Stator Winding Resistance (R_s)	0.821 m	
Synchronous Inductance (L_d)	1.5731mH	
Synchronous Inductance (L_q)	1.5731mH	

PMSG Simulation Model

The PSCAD model of the PMSG is depicted in Figure 4.1.

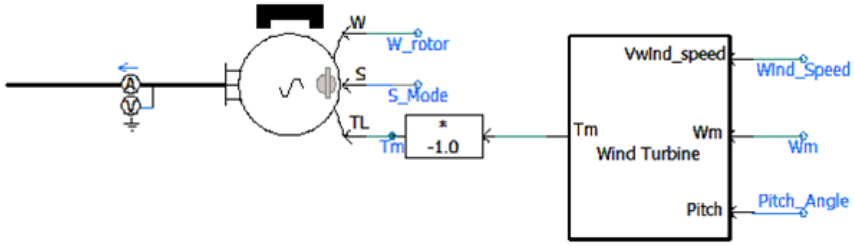

Figure 4.1: Permanent Magnetic Synchronous Generator ratings

4.2.3 5L NPC Voltage Source Converter Rating

The decision to specify a 6 MVA VSC-HVDC rating for the PMSG system is based on the need to align capacities and effectively manage reactive power dynamics. Given that the PMSG is rated at 2 MW for mechanical power and 2.2419 MVA for apparent power, the chosen VSC-HVDC capacity matches the system's power generation and conversion requirements. Moreover, it enables the absorption and provision of reactive power, essential for voltage stability and grid synchronization. This specification considers the requirements for AC filters, converter operations, and efficient power flow management, ensuring optimal performance and adaptability across different grid conditions.

Converter Terminal Rating

The peak of the fundamental component of the converter's output line-to-line voltage is related to the steady-state modulation index m and the DC-link voltage V_{dc} as given by Eq. (4.1) [97].

$$V_{conv} = \frac{1}{2}\sqrt{\frac{3}{2}}V_{dc}m \tag{4.1}$$

$$V_{conv} = \frac{1}{2}\sqrt{\frac{3}{2}}(1126.77)(0.9)$$

$$V_{conv} = 620.62 \text{ V}$$

DC Voltage Rating

The dc voltage rating is determined to ensure that the converter does not saturate when switching on/off using SPWM technology [98][11][99]. Therefore, the minimum dc voltage is determined based on these considerations.

$$V_{dc} = 2\sqrt{\frac{2}{3}}V_{LL} \tag{4.2}$$

$$V_{dc} = 2\sqrt{\frac{2}{3}}(690) = 1126.77V$$

In order to operate within the linear modulation index range and prevent saturation effects, the PWM modulation index is limited to 1, with a range of $0 < m \leq 1$. For this study, a modulation index of $m = 0.9$ is chosen, corresponding to 1126.77 V for the dc voltage rating.

DC-Capacitor Rating

The capacitor rating is chosen considering the power magnitude transferred through the converter, and it is related to the general capacitor time constant. This time constant is calculated as the ratio of the DC-link voltage to the difference between the active power and the power at the fundamental frequency. By considering this criterion, the appropriate capacitor rating can be determined for the converter system [100][101].

$$C_{dc} = \frac{\tau S_N}{0.5{V_{dc}}^2} \tag{4.3}$$

With a time constant of 5ms and utilizing Eq. (4.3) along with a converter rating of 3MVA, the DC-link capacitor can be determined as follows.

$$C_{dc\_eq} = \frac{(5 \times 10^{-3})(3 \times 10^6)}{(0.5)(1126.77^2)} = 23.63\text{mF}$$

The sizes of individual capacitors are determined as follows:

$$C_{dc\_indv} = 4C_{dc\_eq} = 94.52\text{mF}$$

4.2.4 AC Filters Rating

The filter capacitance required to achieve the cutoff frequency of 200 Hz and to address potential ringing resulting from the combination of L_{grid} and C_{filter} is calculated, considering that the AC-filters are rated at 30% of the converter rating. Additionally, a damping circuit is included to reduce any undesirable effects caused by their interaction.

The filter capacitance needed to provide the cutoff frequency with the inductor (L_{grid}) can be calculated as follows:

$$C_{filter} = \frac{1}{(2\pi f_{cutoff})^2 L_{grid}} \tag{4.4}$$

The filter capacitance for the system using Eq. (4.4).

$$C_{filter} = \frac{10^6}{(2\pi 200)^2 (0.0015731)} = 403\text{uF}$$

$$L_{\_GSC} = 5L_{grid} = 7.86\text{mH}$$

The damping capacitance and resistance can be calculated:

$$C_{\_GSC} = \frac{C_{filter}}{2} = \frac{5974}{2} = 201.5\text{uF}$$

$$R_{\_GSC} = \sqrt{\frac{L\_GSC}{C\_GSC}} \tag{4.5}$$

$$R_{\_GSC} = \sqrt{\frac{0.00786}{201.5}} = 6.245\Omega$$

Figure 4.2 Present a simulation block of the the grid side filter.

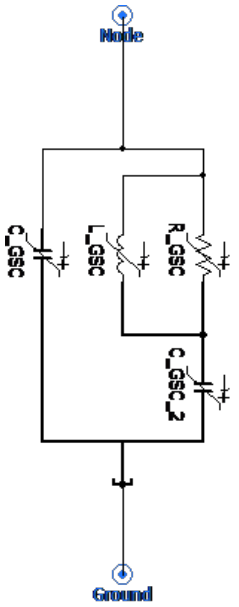

Figure 4.2: Grid Side Filters

4.2.5 Reactance Rating

The phase reactor plays a critical role in enabling the VSC-HVDC system to independently control active and reactive powers. Additionally, the reactor serves to eliminate higher-order harmonics present in the grid's output current [102]. Choosing the right coupling inductance is of paramount importance as it directly influences the effectiveness of filtering and harmonic tracking [103]. The equation governing the interfaced reactor is provided in Eq. (4.6).

$$\mathrm{L} = \frac{\Delta t \omega_e \left(\Delta V_{LL}\right)}{0.9 \times 0.612 V_{dc}} \tag{4.6}$$

$$= \frac{0.25 \times 10^{-3} \times 314.16 \times \left(\Delta V_{LL}\right)}{0.9 \times 0.612(1126.77)} = 66.5\mathrm{mH}$$

Where,
Δt The current's tracking time (s)
ω_e The electrical angular frequency (rad/s)
ΔV_{LL} The change in converter line-to-line voltage (V)
V_{dc} DC-Link Voltage (V)

4.2.6 Transformers Parameters

To integrate the 690 V wind turbine into the 33kV utility grid, a transformer is necessary to step up the converter's output terminal voltage to match the voltage level of the local grid. The PSCAD model of the PMSG is depicted in Figure 4.3.

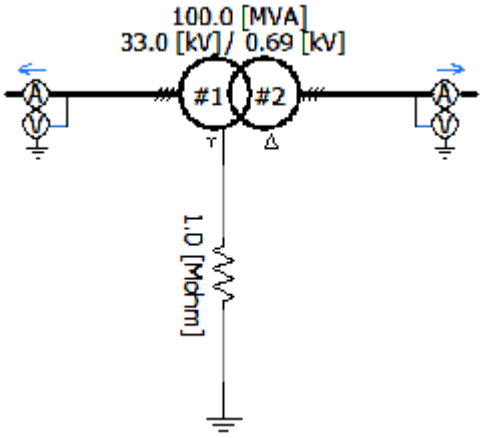

Figure 4.3: Transformers Parameters

4.3 Chapter Summary

This chapter focused on determining the appropriate sizes of the components that constitute a wind energy conversion system. The computed values for these components are consolidated and presented in Table 4.3.

Parameters	**Values**
WT -PMSG rating	$2\text{MW}, 690$ V
DC-link voltage	1126.77 V
line-to-line voltage	620.62 V
DC-link capacitor size	94.52mF
Phase reactor size	66.5mH

Table 4.3: System Specification

Chapter 5

Control Design

5.1 Introduction

This chapter focuses on the control design of the WECS based PMSG. It is dedicated to addressing essential design requirements such as bandwidth, phase margin, percentage overshoot, rising time, and settling time, which play a vital role in this research. The performance and stability of the controllers are evaluated through the use of bode plots and step response curves, all implemented within the MATLAB environment.

5.1.1 Inner Current Specification

The study considered a typical frequency range of 1 to 2 kHz for high-power VSC switching [104]. Consequently, a switching frequency of 2 kHz was selected for this particular investigation. However, it's important to note that high switching frequencies can be detrimental to Insulated Gate Bipolar Transistors (IGBTs) due to their lack of overcapacity [105]. For a megawatt system, a switching frequency of 2 kHz is desirable. If the frequency bandwidth of the inner current controller is chosen to be equal to one-fourth of the switching frequency , therefore :

$$\omega_{inner} = \frac{2\pi}{4} f_{switching} = \frac{2\pi}{4}(2000) = 3141.59\text{rad/sec} \tag{5.1}$$

The converter's PWM produces a delay that is equivalent to 50 % of the switching frequency. Hence

$$.T_a = \frac{1}{2f_{switching}} = \frac{1}{2(2000)} = 2.5 \times 10^{-4}\text{sec} \tag{5.2}$$

The design specifications for the inner control loop are presented in Table 5.1.

Table 5.1: Inner Current Control Specification

Parameters	**Values**
Bandwidth (ω_{inner})	3141.59 rad/sec
Natural Frequency (ω_{inner})	7274.26 rad/sec
Percentage Overshoot (OS_{inner})	0.05
Damping Ratio (ζ_{inner})	0.69
Phase Margin (PM_{inner})	57.85°
Settling time (Ts_{inner})	1.45×10^{-3}sec
Rise Time (Tr_{inner})	0.52×10^{-3}sec

5.1.2 Outer Control Specification

This design intentionally sets the outer current control loops to operate at a slower rate than the inner current control loops. To accomplish this, the bandwidth of the outer control loops is configured to be one-fourth of the switching frequency utilized in the inner current control loops. This modification ensures that the outer control loops react at a reduced frequency, enabling them to proficiently regulate and oversee the dynamics of the entire system. Therefore :

$$\omega_{outer} = \frac{1}{4}\omega_{inner} = \frac{1}{4}(3141.59) = 785.323\text{rad/sec} \tag{5.3}$$

Table 5.2 shows the outer control loop design specifications that must be met.

Table 5.2: Outer Control Specification

Parameters	**Values**
Bandwidth (ω_{outer})	785.40 rad/sec
Natural Frequency (ω_{outer})	1001.11 rad/sec
Percentage Overshoot (OS_{outer})	0.05
Damping Ratio (ζ_{outer})	0.69
Phase Margin (PM_{outer})	57.85°
Settling time (Ts_{outer})	5.79×10^{-3}sec
Rise Time (Tr_{outer})	2.09×10^{-3}sec

5.2 MSC Control Design

Table 5.3 displays the parameters of the MSC as sized in the previous chapter.

Table 5.3: Machine Side Converter- PMSG Parameters

Parameters	Values
PMSG Inductor (L_{sdq})	1.573×10^{-3}H
PMSG Stator (R_s)	$0.821 \times 10^{-3}\Omega$

5.2.1 Inner Current Control Loop

Uncompensated System

The open-loop transfer function of the uncompensated system is represented by Eq. (5.4).

$$G_{c\_inner\_uncomp}(s) = \frac{G_{c\_inner}(s)}{(sT_a + 1)\left[s\left(L_{sdq}\right) + R_s\right]} \tag{5.4}$$

$$G_{c\_inner\_uncomp}(s) = \frac{G_{c\_inner}(s)}{(2.5 \times 10^{-4}s + 1)\left[1.585 \times 10^{-3}s + 0.832 \times 10^{-3}\right]}$$

Figure 5.1 shows the bode plot of the uncompensated system which presents an inner current loop ,where $G_{c\_inner}(s)$=1.

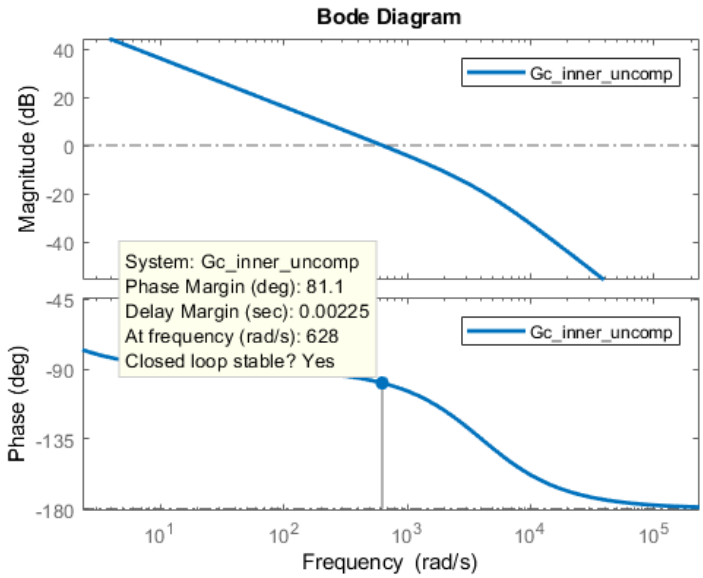

Figure 5.1: Bode plot of the uncompensated inner current controller open-loop transfer function

The uncompensated system has a bandwidth frequency of 628 rad/s and a phase margin of 81.1°. From Figure 5.1, it can be observed that the actual value of 3141.59 rad/s is less than the bandwidth frequency, causing a delayed response in the system. The system's reaction time is slowed down by at least a 90° phase lag.

To increase the magnitude curve and achieve the required bandwidth of 3141.59 rad/s, the uncompensated system must be multiplied by the gain K_{-gain}. The value of the gain can be determined using the following formula:

$$|G_{c\_inner\_uncomp}(s)| = \frac{K_{-gain}}{(2.5 \times 10^{-4}s + 1)\left[1.573 \times 10^{-3}s + 0.821 \times 10^{-3}\right]} \tag{5.5}$$

Let $|G_{c\_inner\_uncomp}(s)| = 3141.59$ rad/s
Therefore,the calculated value of the gain is ($K_{-gain} = 6.3$)

$$G_{c\_inner\_uncomp}(s) = \frac{6.3}{(2.5 \times 10^{-4}s + 1)\left[1.573 \times 10^{-3}s + 0.821 \times 10^{-3}\right]} \tag{5.6}$$

The phase margin of the transfer function given by Eq. (5.5) is calculated to be $PM_{inner} = 51.9°$. However, to increase the phase margin to the required value of $PM_{inner} = 57.9°$, a phase lead compensator is needed. The frequency response technique is employed to design a first-order phase lead compensator, represented by the transfer function presented in Eq. (5.7) [106].

$$G_{lead}(s) = G_c\left[\frac{s + 1/T_1}{s + 1/(\alpha T_2)}\right], 0 < \alpha < 1 \tag{5.7}$$

To shift the phase margin to the required value, the pole and zero of the phase-lead compensator are located as follows: $\omega_{inner\_zero} = 2831.20$ rad/sec and $\omega_{inner\_pole} = 3486.04$ rad/sec. The phase-lead compensator can be computed as follows:
Where,

$$\alpha = \left(\frac{\omega_{inner\_zero}}{\omega_{inner\_pole}}\right) = \frac{2831.20}{3486.04} = 0.812 \tag{5.8}$$

$$G_c = \sqrt{\alpha} = \sqrt{0.812} = 0.901$$

$$T_1 = \frac{1}{\omega_{inner\_zero}} = \frac{1}{2831.20} = 3.53 \times 10^{-4}, \quad T_2 = T_1\alpha = 2.868 \times 10^{-4}$$

The Phase Lead compensator transfer function is given by Eq. (5.9).

$$G_{lead}(s) = 0.901\left[\frac{1 + 3.58 \times 10^{-4}s}{1 + 2.898 \times 10^{-4}s}\right] \tag{5.9}$$

Compensated System

The compensated transfer function of the inner current control is obtained by taking the product of Eq. (5.6) and Eq. (5.10).

$$G_{c\_inner\_comp}(s) = G_{c\_inner\_comp\_gain}(s) \times G_{lead}(s) \tag{5.10}$$

$$G_{C\_inner\_comp}(s)$$
$$= \frac{5.65 + 1.99 \times 10^{-3}s}{1.18 \times 10^{-10}s^3 + 8.389 \times 10^{-7}s^2 + 1.573 \times 10^{-3}s + 0.821 \times 10^{-3}}$$

As shown in Figure 5.2, the phase lead compensator successfully maintained the bandwidth at 3.14e+3 rad/sec while adjusting the phase curve to achieve a phase margin of 57.9°. Therefore, the phase margin and bandwidth design requirements have been met, ensuring the desired performance and stability of the system.

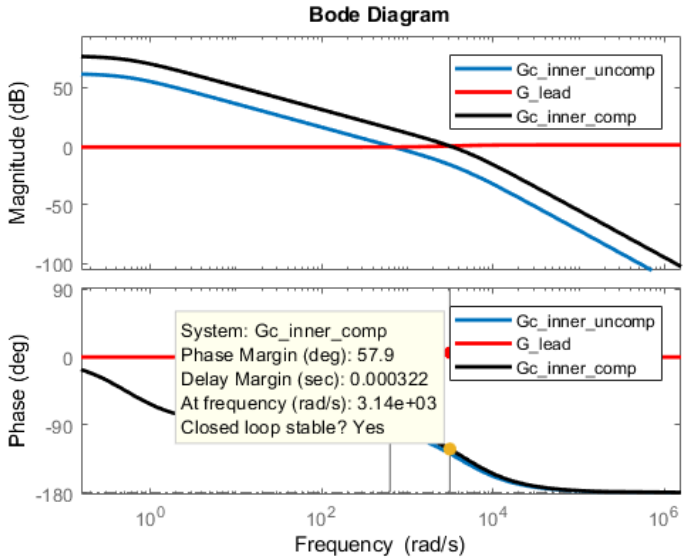

Figure 5.2: Bode plot of the open-loop inner current controller with phase-lead compensation transfer function

Step Response

Figure 5.3 illustrates the step response of the inner current control loop for both the uncompensated and compensated closed-loop transfer functions. As presented in Table 5.4, the achieved overshoot, settling time, and rising time all fall within the desired range, confirming that the design requirements have been successfully fulfilled. This validates the satisfactory performance of the control system for the inner current loop.

$$G_{C\_inner\_comp\_sys}(s) = \frac{4.959 + 1.77 \times 10^{-3}s}{1.114 \times 10^{-10}s^3 + 8.389 \times 10^{-7}s^2 + 3.347 \times 10^{-3}s + 4.96} \tag{5.11}$$

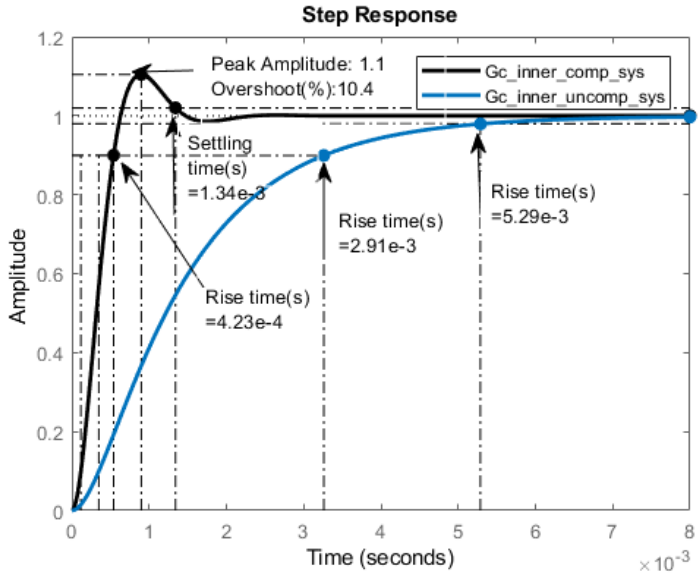

Figure 5.3: Inner current transfer function's step response when compensated and uncompensated

Table 5.4: Inner current control loop specification

Parameters	**Desired Values**	**Obtained Values**
Percentage Overshoot (OS_{inner})	0.05	0.104
Settling time (Ts_{inner})	1.45×10^{-3}sec	1.34×10^{-3}sec
Rise Time (Tr_{inner})	0.52×10^{-3}sec	0.423×10^{-3}sec

5.2.2 DC Voltage-Outer Current Loop

Table 5.5 presents the calculated DC side parameters from the previous chapter:

Table 5.5: DC side Parameters

Parameters	Values
DC Voltage (V_{dc})	$1126.77V$
Capacitor (C_{eq})	$23.63uF$

Uncompensated System

The closed-loop transfer function of the phase-lead compensated inner current system, given by Eq.(5.10), is substituted into Eq.(5.12). As a result, the DC-link voltage's uncompensated open-loop transfer function is expressed as follows:

$$G_{Vdc\_outer\_uncomp}(s) = \frac{G_{c\_outer}(s)G_{c\_inner\_comp}(s)}{C_{eq}s\left[(sT_a+1)(sL_{sdq}+R_s)\right] + G_{c\_inner\_comp}(s)} \tag{5.12}$$

$$= \frac{G_{c\_outer}(s)(4.13s + 1.17\times10^4)}{6.11\times10^{-9}s^4 + 4.49\times10^{-5}s^3 + 0.19s^2 + 301.05s}$$

The uncompensated outer DC-link voltage control loop's is shown in Figure 5.4. Where, $G_{c\_outer}(s) = 1$.

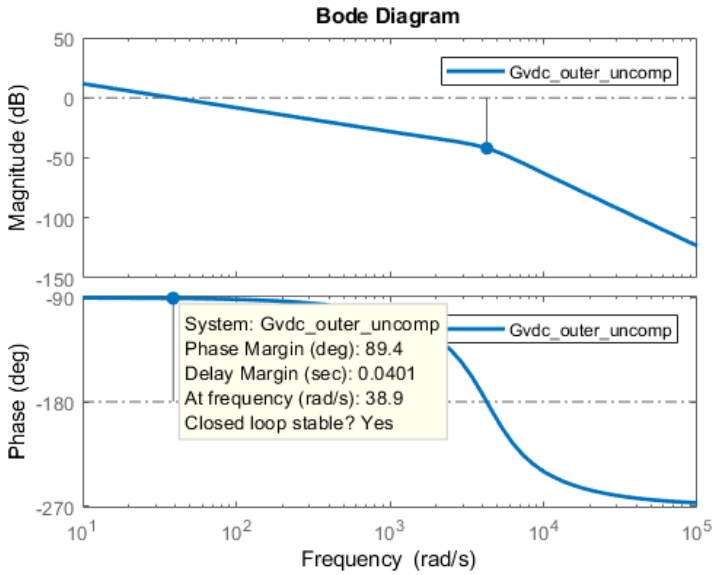

Figure 5.4: Bode plot of the uncompensated outer DC-link voltage controller's open-loop transfer function

The uncompensated system has a phase margin of 89.4°, but the bandwidth frequency is only 38.9 rad/s, which is significantly lower than the desired target value of 785.40 rad/s. This low bandwidth frequency leads to a delayed system response. To achieve the required bandwidth of 785.40 rad/s, the gain (K_{Vdc_gain}) is applied to the uncompensated system to raise the magnitude curve and improve the system's response.

$$|G_{Vdc\_outer\_uncomp}(s)| = \frac{G_{c\_outer}(s)K_{Vdc\_gain}(4.13s + 1.17 \times 10^4)}{6.01 \times 10^{-9}s^4 + 4.49 \times 10^{-5}s^3 + 0.19s^2 + 300.9s} \tag{5.13}$$

Let $|G_{Vdc\_outer\_uncomp}(s)| = 785.40$ rad/s.
Therefore, the value of the gain is calculated as $K_{Vdc\_gain} = 20.05$

$$G_{Vdc\_outer\_comp\_gain}(s) = \frac{(82.83s + 2.35 \times 10^5)}{6.01 \times 10^{-9}s^4 + 4.498 \times 10^{-5}s^3 + 0.190s^2 + 300.9s} \tag{5.14}$$

The phase margin of the transfer function given by Eq 5.13 is calculated to be $PM_{outer} = 77.3°$. However, to decrease the phase margin to the desired value of $PM_{outer} = 57.9°$, a phase lag compensator is needed. The frequency response technique is employed to design a first-order phase lag compensator, represented by the transfer function presented in Eq. (5.15).

$$G_{lag}(s) = G_c\left[\frac{s + 1/T_1}{s + 1/(\alpha T_2)}\right], 0 < \alpha < 1 \tag{5.15}$$

The pole and zero that are required to shift the phase margin to required value are located as follows: $\omega_{outer\_zero} = 1110.30$ rad/sec and $\omega_{outer\_pole} = 555.56$ rad/sec. Therefore, the phase-lead compensator is computed as follows:
Where,

$$\alpha = \left(\frac{\omega_{inner\_zero}}{\omega_{inner\_pole}}\right) = \frac{1110.30}{555.56} = 1.99 \tag{5.16}$$

$$G_c = \sqrt{\alpha} = \sqrt{1.99} = 1.41$$

$$T_1 = \frac{1}{\omega_{outer\_zero}} = \frac{1}{1110.30} = 9.0 \times 10^{-4}, \quad T_2 = T_1\alpha = 1.79 \times 10^{-3}$$

The transfer function of the phase lag compensator is given by Eq. (5.17)

$$G_{lag}(s) = 1.41\left[\frac{1 + 9.0 \times 10^{-4}s}{1 + 1.79 \times 10^{-3}s}\right] \tag{5.17}$$

Compensated System

The compensated transfer function of the DC voltage control is obtained by taking the product of Eq. (5.17) and Eq. (5.14). It is given as Eq. (5.18).

$$G_{Vdc\_outer\_comp}(s) = G_{lag}(s) \times G_{Vdc\_outer\_uncomp\_gain}(s) \tag{5.18}$$
$$= \frac{0.106s^2 + 415.7s + 3.32 \times 10^5}{1.08 \times 10^{-11}s^5 + 8.69 \times 10^{-8}s^4 + 38.71 \times 10^{-5}s^3 + 0.732s^2 + 300.9s}$$

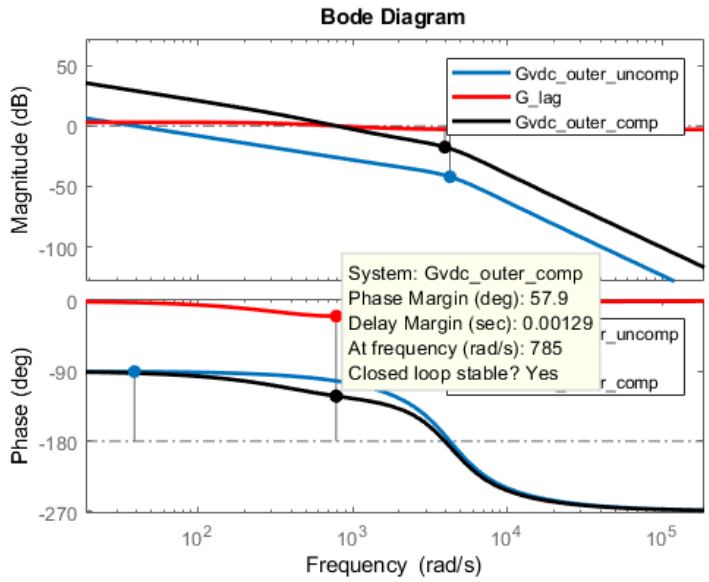

Figure 5.5: Bode plot of the phase -lag compensated DC-link voltage control loop

As depicted in Figure 5.5, the phase-lag compensator effectively pushed the phase curve downward, achieving a phase margin of 57.9°. The 785 rad/s bandwidth remains unaffected, meeting the design specifications for both the bandwidth and phase margin. This successful fulfillment of the design requirements ensures the desired performance and stability of the DC-link voltage control loop.

Step Response

Figure 5.6 illustrates the step response of the DC voltage control for both the uncompensated and compensated systems. As indicated in Table 5.6, the design specifications for overshoot, settling time, and rise time were successfully met, confirming the satisfactory performance of the DC voltage control loop.

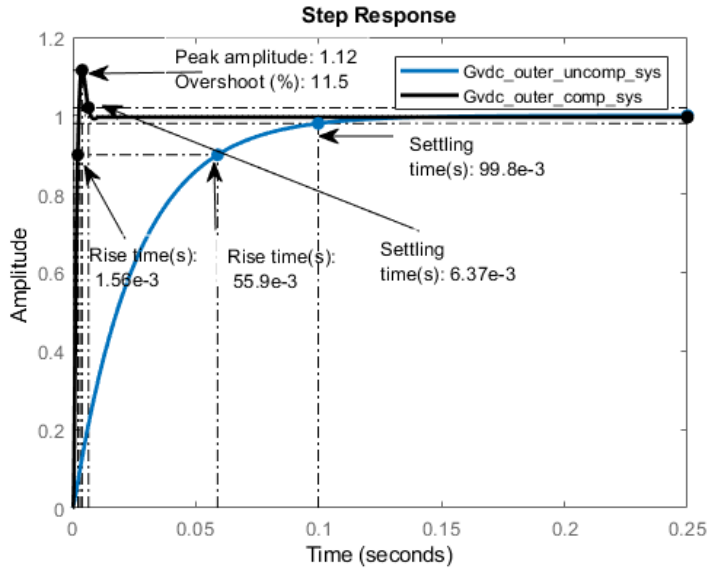

Figure 5.6: Step response of DC voltage outer loop control for compensated and uncompensated system

Table 5.6: DC Voltage outer control loop specification

Parameters	**Desired Values**	**Obtained Values**
Percentage Overshoot (OS_{outer})	0.03	0.115
Settling time (Ts_{outer})	5.79×10^{-3}sec	6.37×10^{-3}sec
Rise Time (Tr_{outer})	2.09×10^{-3}sec	1.56×10^{-4}sec

5.2.3 Stator Voltage-Outer Loop

Table 5.7 present the stator voltage side parameters calculated from the previous chapter:

Table 5.7: Stator Voltage Parameters

Parameters	Values
Stator Voltage (V_{st})	$620.62V$

Uncompensated System

The uncompensated outer stator voltage control loop's open-loop transfer function is depicted by Eq. (5.19).

$$G_{V\_st\_outer\_uncomp}(s) = G_{V\_st}(s)G_{c\_inner\_comp}(s)\left[\frac{3X_s}{2} + V_{conv}\right] \tag{5.19}$$

$$G_{V\_st\_outer\_uncomp}(s) = \frac{(2.48s + 7010) \times G_{V\_st}}{2.256 \times 10^{-10}s^3 + 1.689 \times 10^{-6}s^2 + 7.14 \times 10^{-3}s + 11.3}$$

Figure 5.7 demonstrates the magnitude and phase curves of the outer stator voltage control loop's uncompensated open-loop transfer function. Where, $G_{V\_st}(s) = 1$.

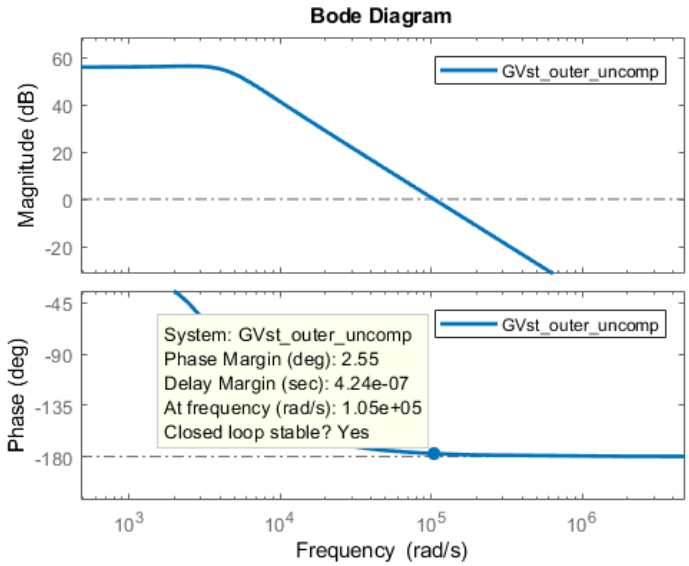

Figure 5.7: Bode plot of the uncompensated outer stator voltage controller's open-loop transfer function

The bode plot of the open-loop transfer function of the uncompensated outer stator voltage controller in Figure 5.7 reveals that the phase margin and bandwidth of the uncompensated system are 2.55° and 1.05e+05 rad/s, respectively. Although the bandwidth is significantly higher than required, the phase margin falls short of expectations.

To address this, a phase-lag compensator is necessary to reduce the magnitude curve and ensure that it intersects the 0dB line at the required bandwidth of 785.40 rad/s. By employing the phase-lag compensator, the phase margin can be increased to meet the design specifications while maintaining the desired bandwidth.

The transfer function of the phase-lag compensator is presented by Eq 5.20.

$$G_{lag}(s) = \left[\frac{1 + s/z_c}{1 + s/p_c}\right] \tag{5.20}$$

The pole and zero that are required to shift the phase margin to required value are located as follows: $z_c = 0.490 \times 10^6$rad/sec and $p_z = 1.259$rad/sec. Therefore, the transfer function of the phase lag compensator is given by Eq 5.21

$$G_{lag}(s) = \left[\frac{1 + 0.490 \times 10^{-6}s}{1 + 0.795s}\right] \tag{5.21}$$

Compensated System

The open-loop transfer function of the phase-lag compensated system is obtained by substituting Eq. (5.19) into Eq. (5.47), resulting in Eq. (5.22).

$$G_{V\_st\_outer\_comp}(s) = G_{lag\_}(s) \times G_{V\_st\_outer\_uncomp}(s) \tag{5.22}$$

$$= \frac{5.056 \times 10^{-6}s^2 + 2.49s + 7010}{1.79 \times 10 - 10s^4 + 1.34 \times 10^{-6}s^3 + 5.67 \times 10^{-3}s^2 + 8.98s + 11.3}$$

The phase-lag compensator successfully reduced the magnitude curve by 55.9 dB at the bandwidth of 786 rad/s, which is close to the required bandwidth, as indicated by the transfer function given in Eq. (5.22). The design criteria for the bandwidth have been met. However, although the phase margin of 77.5° is achieved, it still falls short of the desired phase margin of 57.85°. To attain the necessary phase margin, a second phase-lag compensator is needed to further lower the phase curve. By employing this additional phase-lag compensator, the phase margin can be increased to meet the design requirements.

The pole and zero that are required to shift the phase margin to required value are located as follows: $\omega_{outer_zero} = 1114.39$rad/s and $\omega_{outer_pole} = 553.49$rad/s. Therefore, the second phase-lead compensator is computed as follows:

$$G_{lag\_2}(s) = G_c \left[\frac{s + 1/T_1}{s + 1/(\alpha T_2)} \right], 0 < \alpha < 1 \tag{5.23}$$

Where,

$$\alpha = \left(\frac{\omega_{outer\_zero}}{\omega_{outer\_pole}} \right) = \frac{1114.39}{555.49} = 2.01 \tag{5.24}$$

$$G_c = \sqrt{\alpha} = \sqrt{1.99} = 1.42$$

$$T_1 = \frac{1}{\omega_{outer\_zero}} = \frac{1}{1114.39} = 8.97 \times 10^{-4}, T_2 = T_1 \alpha = 1.804 \times 10^{-3}$$

Therefore, the transfer function of the phase lag compensator is given by Eq. (5.25).

$$G_{lag\_2}(s) = 2.01 \left[\frac{1 + 8.97 \times 10^{-4} s}{1 + 1.804 \times 10^{-3} s} \right] \tag{5.25}$$

The second phase-lag compensator is applied to the phase-lag compensated system in order to calculate the transfer function of the system. The transfer function is therefore given by Eq. (5.26).

$$G_{V\_st\_outer\_comp}(s) = G_{lag\_1}(s) \times G_{lag\_2}(s) \times G_{V\_st\_outer\_uncomp}(s) \tag{5.26}$$

$$= \frac{6.44 \times 10^{-9} s^3 + 31.78 \times 10^{-3} s^2 + 12.46 s + 9947}{3.24 \times 10 - 13 s^5 + 2.61 \times 10 - 9 s^4 + 1.16 \times 10 - 5 s^3 + 21.9 \times 10 - 3 s^2 + 9.01 s + 11.3}$$

Figure 5.8 shows the bode plot of the outer stator voltage controller's open-loop phase-lag-lag adjusted transfer function.

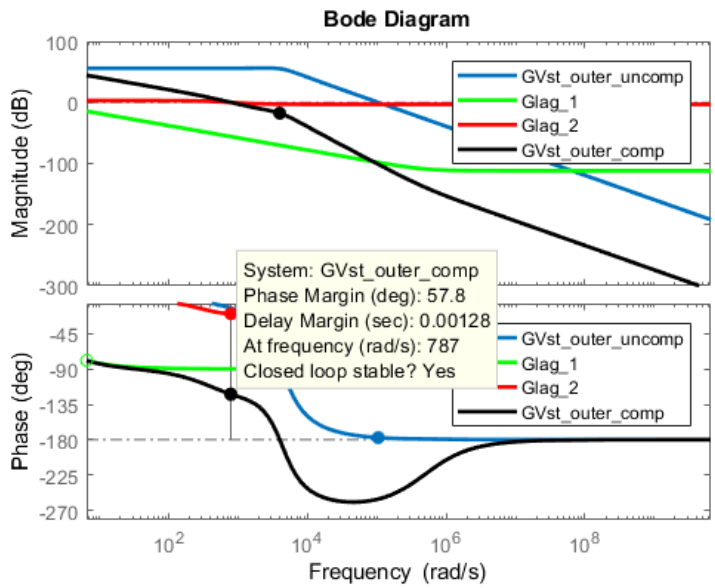

Figure 5.8: Bode plot of the phase-lag-lag compensated stator voltage control loop

Step Response

Figure 5.9 illustrates the step response of the stator outer control loop's closed-loop transfer function for both the uncompensated and compensated systems.

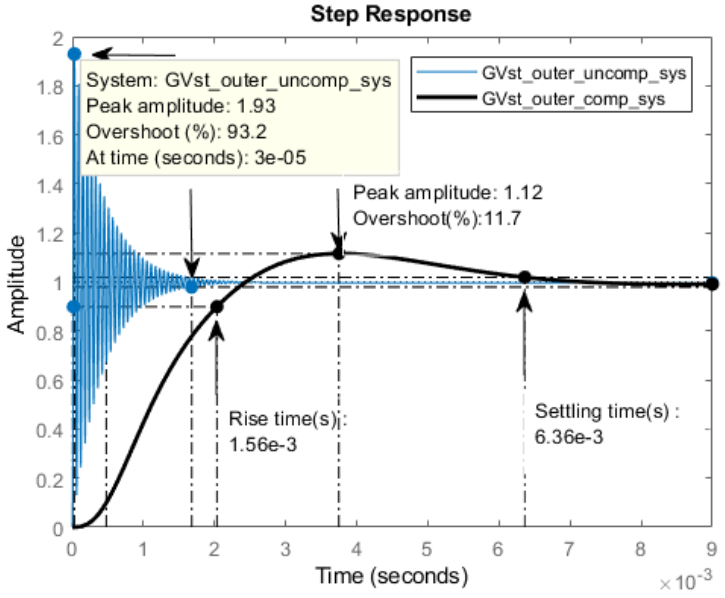

Figure 5.9: Step response of the stator outer loop control

Table 5.8 illustrates that the overshoot, settling time ,rise time design specification has been met.

Table 5.8: Stator outer control loop specification

Parameters	**Desired Values**	**Obtained Values**
Percentage Overshoot (OS_{outer})	0.03	0.117
Settling time (Ts_{outer})	5.79×10^{-3}sec	6.36×10^{-3}sec
Rise Time (Tr_{outer})	2.09×10^{-3}sec	1.56×10^{-4}sec

5.3 GSC Control Design

Table 5.9 displays the parameters of the GSC as sized in the previous chapter.

Table 5.9: Grid parameters

Parameters	Value
Grid inductance (L_g)	66.5×10^{-3}H
Grid resistance (R_g)	$0.665 \times 10^{-3}\Omega$

5.3.1 Inner Current Control Loop

The open-loop inner current control transfer function of the uncompensated system is represented by Eq. (5.27).

$$G_{c\_inner\_uncomp}(s) = \frac{G_{c\_inner}(s)}{(sT_a + 1)\,[sL_g + R_g]} \tag{5.27}$$

Uncompensated System

$$G_{c\_inner\_uncomp}(s) = \frac{G_{c\_inner}(s)}{(2.5 \times 10^{-4}s + 1)\,[66.5 \times 10^{-3}s + 0.665 \times 10^{-3}]} \tag{5.28}$$

Figure 5.10 shows the bode plot of the inner current control loop uncompensated, where $G_{c\_inner}(s) = 1$

That's correct. Since the bandwidth of the uncompensated system is lower than the desired value of 3141.59 rad/s, the system's response may be slower than expected. To achieve the desired bandwidth, the uncompensated system can be multiplied by the gain $K_{g\_inner\_gain}$ to increase the magnitude curve, effectively raising the bandwidth and improving the system's response. This gain adjustment allows the system to meet the required performance specifications for the inner current control loop.

$$\left|G_{c\_inner\_uncomp}(s)\right| = \frac{G_{c\_inner}(s)K_{g\_inner\_gain}}{(2.5\times10^{-4}s+1)\left[66.5\times10^{-3}s+0.665\times10^{-3}\right]}$$

Let $\left|G_{c\_inner\_uncomp}(s)\right|$=314.59 rad/s.
Therefore, $K_{g\_inner\_gain} = 266.01$

$$G_{c\_inner\_comp\_gain}(s) = \frac{266.01}{(2.5\times10^{-4}s+1)\left[1.573\times10^{-3}s+0.821\times10^{-3}\right]} \tag{5.29}$$

The phase margin of the transfer function given by Eq. (5.29) is calculated to be $PM_{inner} = 51.8°$. However, to increase the phase margin to the desired value of $PM_{inner} = 57.9°$, a phase lead compensator is needed. The frequency response technique is utilized to design a first-order phase lead compensator, represented by the transfer function presented in Eq. (5.30) [106].

$$G_{lead}(s) = G_c\left[\frac{s+1/T_1}{s+1/(\alpha T_2)}\right], 0<\alpha<1 \tag{5.30}$$

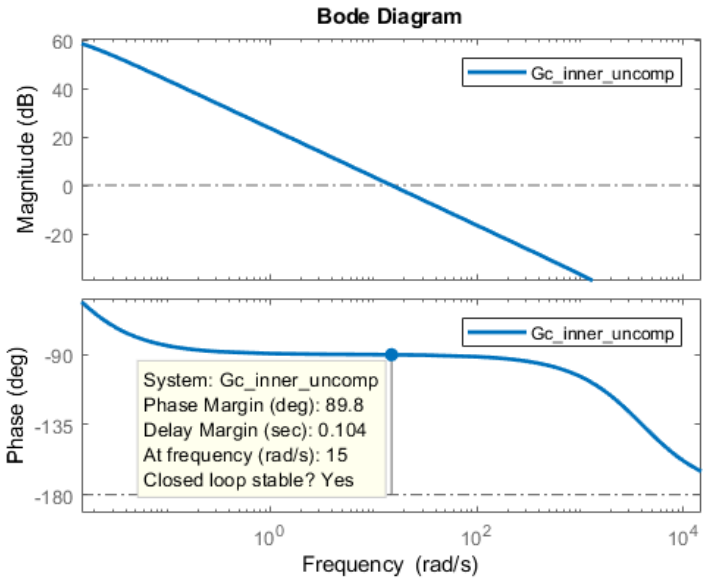

Figure 5.10: Bode plot of the uncompensated inner controller open-loop transfer function

To shift the phase margin to the desired value, the pole and zero of the phase-lead compensator are located at $\omega_{inner_zero} = 2826.24$rad/s and $\omega_{inner_pole} = 3492.13$rad/s, respectively. The phase-lead compensator can be computed as follows:

Where,

$$\alpha = \left(\frac{\omega_{inner\_zero}}{\omega_{inner\_pole}}\right) = \frac{2826.24}{3492.13} = 0.809 \tag{5.31}$$

$$G_c = \sqrt{\alpha} = \sqrt{0.809} = 0.899$$

$$T_1 = \frac{1}{\omega_{inner\_zero}} = \frac{1}{2826.24} = 3.54 \times 10^{-4}, \quad T_2 = T_1\alpha = 2.864 \times 10^{-4}$$

The transfer function of the phase lead compensator is given by Eq. (5.32).

$$G_{lead}(s) = 0.84\left[\frac{1 + 3.54 \times 10^{-4}s}{1 + 2.864 \times 10^{-4}s}\right] \tag{5.32}$$

Compensated System

The gain-compensated system is subjected to the phase-lead compensator, multiplying Eq. (5.29) by Eq. (5.32) results in Eq. (5.33), which denotes the inner current control loop's open-loop phase-lead compensated transfer function.

$$G_{c\_inner\_comp\_gain}(s) = G_{c\_inner\_uncomp\_gain}(s) \times G_{lead}(s) \tag{5.33}$$

$$= \frac{9.924 \times 10^{-3}s + 26.21}{5.018 \times 10^{-10}s^3 + 3.882 \times 10^{-6}s^2 + 7.5 \times 10^{-3}s + 6.5 \times 10^{-4}}$$

Figure 5.11 presents the phase and magnitude curves of the phase-lead compensated open-loop transfer function of the inner current control loop.

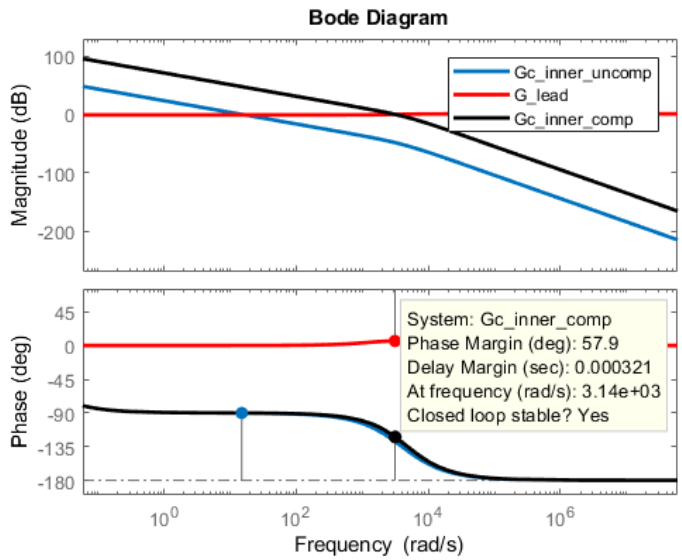

Figure 5.11: illustrates the magnitude and phase curves of the phase-lead compensated open-loop transfer function of the inner current control loop

Step Response

Figure 5.12 the step response of the inner current control loop's compensated and uncompensated closed-loop transfer function.

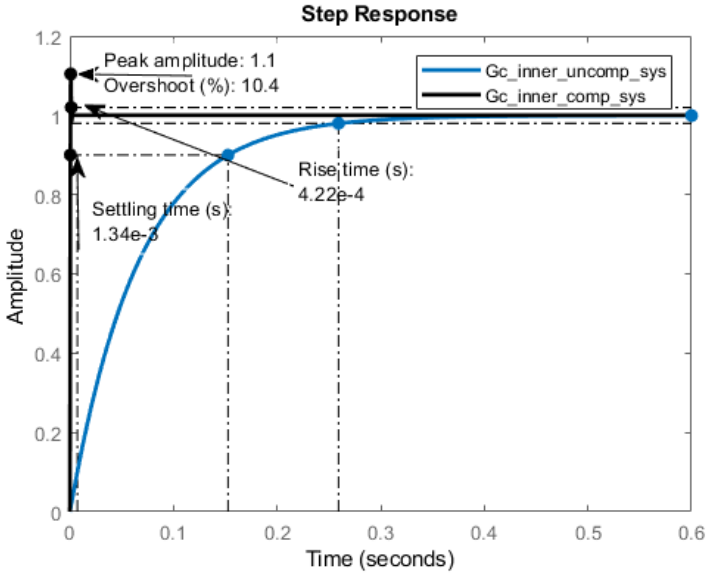

Figure 5.12: Step response of the compensated and uncompensated system

Table 5.10 illustrates that the overshoot, settling time ,rise time design specification has been met.

Table 5.10: Inner current control loop specification

Parameters	**Desired Values**	**Obtained Values**
Percentage Overshoot (OS_{inner})	0.05	0.104
Settling time (Ts_{inner})	1.45×10^{-3}sec	1.34×10^{-3}sec
Rise Time (Tr_{inner})	0.52×10^{-3}sec	0.422×10^{-3}sec

5.3.2 Active Power-Outer Control Loop

Table 5.11 present the stator voltage side parameters calculated from the previous chapter:

Table 5.11: Active Power Parameters

Parameters	**Values**
Voltage d-component (V_{gd})	$620.62V$

Uncompensated System

The active power control loop's uncompensated transfer function is given by Eq. (5.34).

$$G_{P\_outer\_uncomp}(s) = G_{P\_outer}(s)G_{c\_inner\_cl}(s)\frac{3}{2}V_{gd} \tag{5.34}$$

Where, $G_{c\_inner\_cl}(s)$ is the closed-loop transfer function of the phase-lead compensated grid side inner current loop given by Eq.(5.35).

$$G_{c\_inner\_cl}(s) = \frac{84.67 \times 10^{-3}s + 239.3}{4.76 \times 10^{-9}s^3 + 3.57 \times 10^{-5}s^2 + 151.2 \times 10^{-3}s + 239.3} \tag{5.35}$$

Figure 5.13 demonstrates the bode plot of the uncompensated outer active power control loop provided by Eq.(5.35) Where, $G_{P_{outer}}(s) = 1$.

$$G_{P\_outer\_uncomp}(s) = \frac{(157.7s + 4.46 \times 10^5) \times G_{P\_outer}(s)}{9.52 \times 10^{-9}s^3 + 7.13 \times 10^{-5}s^2 + 302.3 \times 10^{-3}s + 478.6} \tag{5.36}$$

The uncompensated system exhibits a phase margin of 2.08 degrees and a bandwidth of

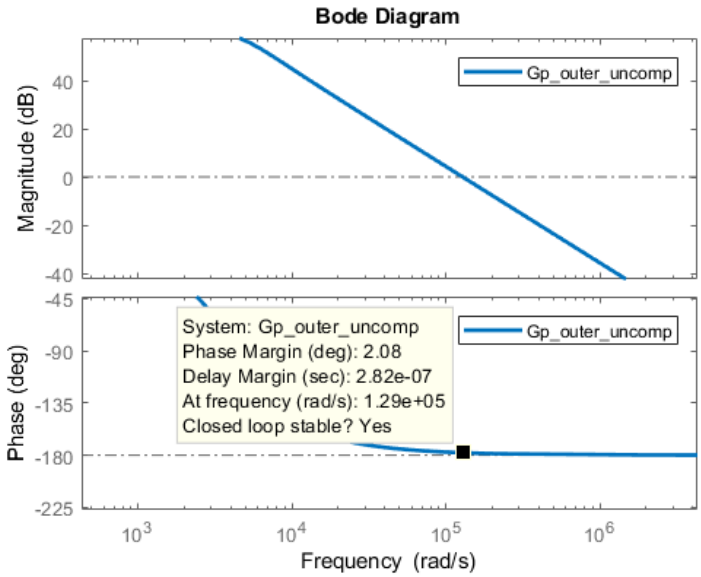

Figure 5.13: Bode plot of the uncompensated outer active power controller's open-loop transfer function

1.29e+05 rad/s, which surpasses the initially planned level by a considerable margin. However, the phase margin remains quite small. To bring the magnitude curve down and ensure it intersects the 0dB line at the desired bandwidth of 785.40 rad/s, a first-order phase lag compensator is designed using the frequency response approach. The transfer function is presented by Eq. (5.37).

$$G_{lag}(s) = \left[\frac{1 + s/z_c}{1 + s/p_c}\right] \tag{5.37}$$

The pole and zero that are required to shift the phase margin to required value are located as follows: $z_c = 0.733 \times 10^6$rad/sec and $p_z = 0.841$rad/sec rad/sec. The phase lag compensator's transfer function is therefore given by Eq. (5.38).

$$G_{lag}(s) = \left[\frac{1 + 1.36 \times 10^{-6}s}{1 + 1.195s}\right] \tag{5.38}$$

$$G_{P\_outer\_uncomp\_lag}(s) = \frac{0.214 \times 10^{-3}s^2 + 158.3s + 4.45 \times 10^5}{1.138 \times 10^{-8}s^4 + 8.53 \times 10^{-5}s^3 + 0.361s^2 + 572.3s + 478.6} \tag{5.39}$$

Compensated System

With the transfer function given by Eq. (5.39), the phase-lag compensator successfully reduced the magnitude curve by 59.4 dB at a bandwidth of 786 rad/s, which is close to the intended bandwidth. Hence, the bandwidth design requirements have been met. However, to attain the required phase margin of 57.85 degrees, an additional second phase-lag compensator is needed, which results in a phase margin of 77.5 degrees

The pole and zero that are required to shift the phase margin to required value are located as follows: $\omega_{outer_zero} = 1114.39$rad/s and $\omega_{outer_pole} = 553.55$rad/s. Therefore, the second phase-lead compensator is computed as follows:

$$G_{lag\_2}(s) = G_c \left[\frac{s + 1/T_1}{s + 1/(\alpha T_2)} \right], 0 < \alpha < 1 \tag{5.40}$$

Where,

$$\alpha = \left(\frac{\omega_{outer\_zero}}{\omega_{outer\_pole}} \right) = \frac{1114.39}{555.49} = 2.01 \tag{5.41}$$

$$G_c = \sqrt{\alpha} = \sqrt{1.99} = 1.42$$

$$T_1 = \frac{1}{\omega_{outer\_zero}} = \frac{1}{1114.39} = 8.97 \times 10^{-4}, \quad T_2 = T_1 \alpha = 1.804 \times 10^{-3}$$

Therefore, the transfer function of the phase lag compensator is given by Eq 5.42

$$G_{lag\_2}(s) = 2.01 \left[\frac{1 + 8.97 \times 10^{-4} s}{1 + 1.804 \times 10^{-3} s} \right] \tag{5.42}$$

In order to determine the transfer function of the phase-lag-lag compensated system, Eq.(5.42) and Eq.(5.51) must be multiplied, yielding Eq.(5.43). The second phase-lag compensator is then applied to the phase-lag compensated system.

$$G_{P\_outer\_comp\_lag\_lag\_2}(s) = G_{P\_outer\_comp\_lag\_1}(s) \times G_{lag\_2}(s) \tag{5.43}$$

$$= \frac{2.723 \times 10^{-7} s^3 + 0.202 s^2 + 791.8 s + 6.32 \times 10^5}{2.056 \times 10^{-11} s^5 + 1.654 \times 10^{-7} s^4 + 0.738 \times 10^{-3} s^3 + 1.395 s^2 + 573.2 s + 478.6}$$

Indeed, the second phase-lag compensator effectively adjusted the phase curve downward, achieving a phase margin of 57.7 degrees while maintaining a constant bandwidth of 785 rad/s. This successful adjustment ensures that both the phase-margin and bandwidth design requirements have been met satisfactorily.

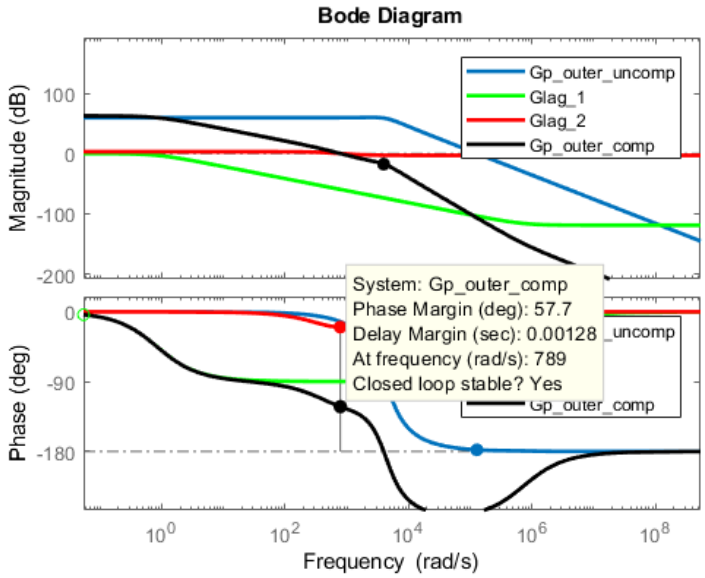

Figure 5.14: Represents the bode plot of the active power controller's open-loop transfer function compensated with the two phase-lag compensator

Step Response

Figure 5.15 illustrates the step response of the grid active power control's closed-loop transfer function for both the compensated and uncompensated cases. All the design specifications for overshoot, settling time, and rising time have been met successfully, as presented in Table 5.12.

.

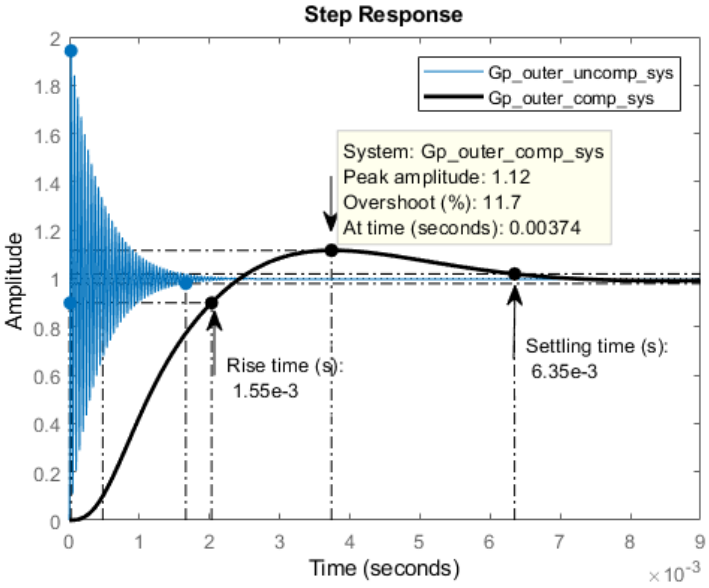

Figure 5.15: Step response of the compensated and uncompensated active power transfer function

Table 5.12: Active Power control specification

Parameters	**Desired Values**	**Obtained Values**
Percentage Overshoot (OS_{outer})	0.05	0.117
Settling time (Ts_{outer})	5.79×10^{-3}sec	6.35×10^{-3}sec
Rise Time (Tr_{outer})	2.09×10^{-3}sec	1.55×10^{-3}sec

5.3.3 Reactive Power-Outer Control Loop

Table 5.13 present the stator voltage side parameter sized from the previous chapter:

Table 5.13: Reactive Power Parameters

Parameters	**Values**
Voltage d-component (V_{gd})	$620.62V$

Uncompensated System

The reactive power control loop's uncompensated transfer function is given by Eq. (5.34).

$$G_{Q\_outer\_uncomp}(s) = -G_{Q\_outer}(s)G_{c\_inner\_cl}(s)\frac{3}{2}V_{gd} \tag{5.44}$$

Figure 5.16 shows the bode plot of the uncompensated outer reactive power control loop given by Eq.(5.45) Where, $G_{Q_{outer}}(s) = 1$.

$$G_{Q\_outer\_uncomp}(s) = \frac{(-157.7s - 4.46 \times 10^5) \times G_{Q\_outer}(s)}{9.52 \times 10^{-9}s^3 + 7.13 \times 10^{-5}s^2 + 302.3 \times 10^{-3}s + 478.6} \tag{5.45}$$

The uncompensated system exhibits a phase margin of -178 degrees and a bandwidth of 1.29e+05 rad/s, which is unexpectedly much higher than anticipated. The phase margin is also quite small. To lower the magnitude curve and make it intersect the 0dB line at the desired bandwidth of 785.40 rad/s, a phase-lag compensator is required. The transfer function of the phase-lag compensator is given by Eq. (5.46).

$$G_{lag}(s) = \left[\frac{1 + s/z_c}{1 + s/p_c}\right] \tag{5.46}$$

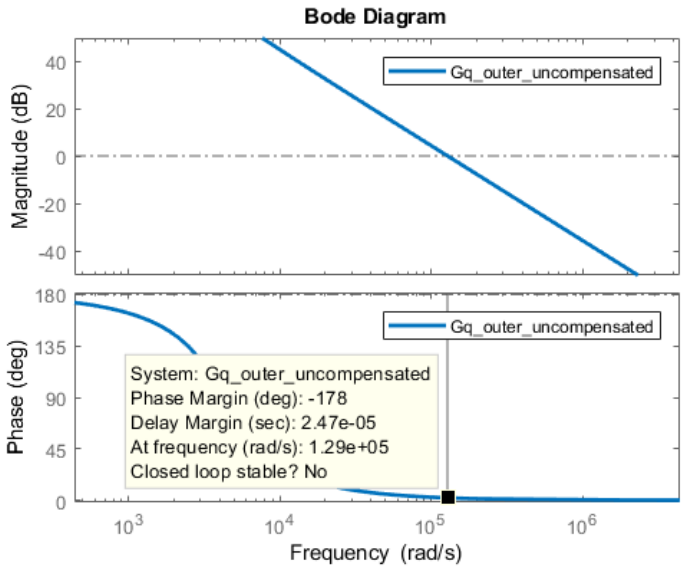

Figure 5.16: Bode plot of the compensated reactive power control loop

The pole and zero that are required to shift the phase margin to required value are located as follows: $z_c = 0.733 \times 10^6$rad/sec and $p_z = 0.841$rad/sec. Therefore, the transfer function of the phase lag compensator is given by Eq 5.47.

$$G_{lag}(s) = \left[\frac{-1 - 1.36 \times 10^{-6}s}{1 + 1.195s}\right] \tag{5.47}$$

$$G_{Q\_outer\_uncomp\_lag}(s) = \frac{0.214 \times 10^{-3}s^2 + 158.3s + 4.45 \times 10^5}{1.138 \times 10^{-8}s^4 + 8.53 \times 10^{-5}s^3 + 0.361s^2 + 572.3s + 478.6} \tag{5.48}$$

Compensated System

The phase-lag compensator effectively reduced the magnitude curve by 59.4 dB at the bandwidth of 786 rad/s, which closely aligns with the desired bandwidth, as indicated by the transfer function in Eq. (5.48). Thus, the bandwidth design criteria have been successfully met. However, although a phase margin of 77.5 degrees is attained, an additional second phase-lag compensator is needed to further lower the phase curve and achieve the required phase-margin of 57.85 degrees.

The pole and zero that are required to shift the phase margin to a required value are located as follows: $\omega_{outer_zero} = 1114.39$rad/s and $\omega_{outer_pole} = 553.55$rad/s. Therefore, the second phase-lead compensator is computed as follows:

$$G_{lag\_2}(s) = G_c\left[\frac{s + 1/T_1}{s + 1/(\alpha T_2)}\right], 0 < \alpha < 1 \tag{5.49}$$

Where,

$$\alpha = \left(\frac{\omega_{outer\_zero}}{\omega_{outer\_pole}}\right) = \frac{1114.39}{555.49} = 2.01 \tag{5.50}$$

$$G_c = \sqrt{\alpha} = \sqrt{1.99} = 1.42$$

$$T_1 = \frac{1}{\omega_{outer\_zero}} = \frac{1}{1114.39} = 8.97 \times 10^{-4}, \quad T_2 = T_1\alpha = 1.804 \times 10^{-3}$$

Therefore, the transfer function of the phase lag compensator is given by Eq.(5.47)

$$G_{lag\_2}(s) = 2.01\left[\frac{1 + 8.97 \times 10^{-4}s}{1 + 1.804 \times 10^{-3}s}\right] \tag{5.51}$$

The phase-lag compensated system is then subjected to the second phase-lag compensator, and the transfer function of the phase-lag-lag compensated system is computed by multiplying Eq.(5.48) and Eq.(5.51), which yields Eq.(5.52).

$$G_{Q\_outer\_comp\_lag\_lag\_2}(s) = G_{Q\_outer\_comp\_lag\_1}(s) \times G_{lag\_2}(s) \tag{5.52}$$

$$= \frac{2.723 \times 10^{-7}s^3 + 0.202s^2 + 791.8s + 6.32 \times 10^5}{2.056 \times 10^{-11}s^5 + 1.654 \times 10^{-7}s^4 + 0.738 \times 10^{-3}s^3 + 1.395s^2 + 573.2s + 478.6}$$

Clearly, the second phase-lag compensator effectively decreased the phase curve, achieving a phase-margin of 57.8° while maintaining a constant bandwidth of 788 rad/s. As a result, the design requirements for both bandwidth and phase-margin have been successfully met.

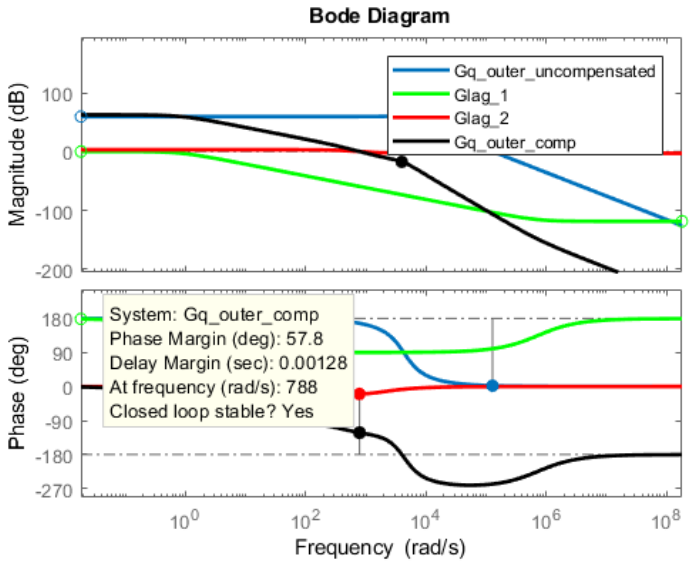

Figure 5.17: Represents the bode plot of the reactive power controller's open-loop transfer function compensated with the two phase-lag compensators

Step Response

Figure 5.18 illustrates the step response of the closed-loop transfer function for grid reactive power control, comparing the uncompensated and compensated versions. It's worth noting that Table 5.14 demonstrates how the design requirements for overshoot, settling time, and rising time have all been successfully met.

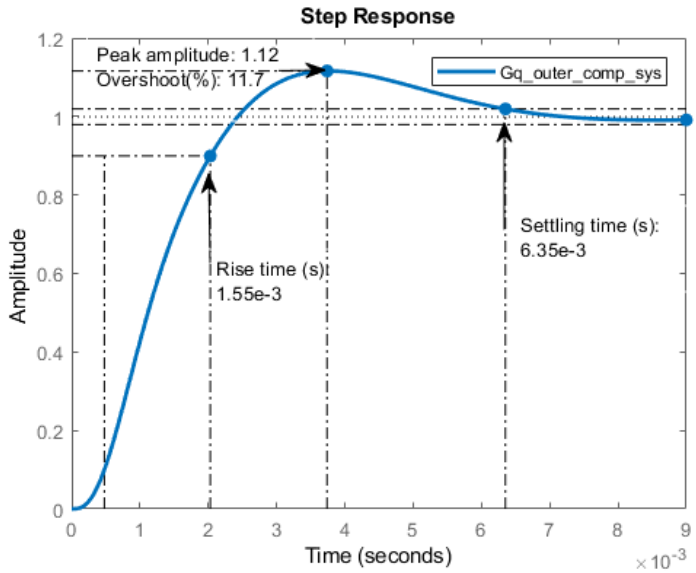

Figure 5.18: Step response of the compensated and uncompensated reactive power transfer function

Table 5.14: Reactive Power control specification

Parameters	**Desired Values**	**Obtained Values**
Percentage Overshoot (OS_{outer})	0.05	0.117
Settling time (Ts_{outer})	5.79×10^{-3}sec	6.35×10^{-3}sec
Rise Time (Tr_{outer})	2.09×10^{-3}sec	1.55×10^{-3}sec

5.4 Chapter summary

In this chapter, a thorough design and stability analysis was performed for both the MSC and GSC controller, aiming to meet specific specifications for power system operation. The primary focus was on creating efficient control algorithms to regulate power flow between the machine side and the grid side. Before implementing the controllers, extensive stability studies were conducted to ensure system stability under various conditions. Bode plots and step response curves played a crucial role in this analysis, providing valuable insights into the system's frequency response and transient behavior, respectively. MATLAB software was utilized to implement the controllers, generate bode plots, and simulate step responses, streamlining the design process. Through iterative tuning of controller parameters based on these analyses, the designs were refined to meet all required performance metrics. As a result, the MSC and GSC controllers were successfully tailored to guarantee stable, efficient, and reliable power system operation in accordance with the specified requirements.

Chapter 6

Simulation

6.1 Introduction

These chapters center on the simulation model of the essential elements of the WECS, which integrates with the control system introduced in the previous chapter. However, the primary focus of this chapter is to develop this simulation model using the PSCAD software and assess the system's performance as the wind turbine responds to varying wind speeds. Through rigorous testing and examination, the chapter seeks to gain valuable insights into the WECS's behavior in real-world conditions and its ability to adapt effectively to changing environmental factors. This analysis is crucial for optimizing the system's efficiency, ensuring seamless grid integration, and advancing the practical implementation of renewable energy technologies. Figure 6.1 illustrates the proposed subsystem, which consists of the following main blocks: the Wind Turbine block, Voltage Source Converter block, Machine-Side Converter, and Grid-Side Converter control block.

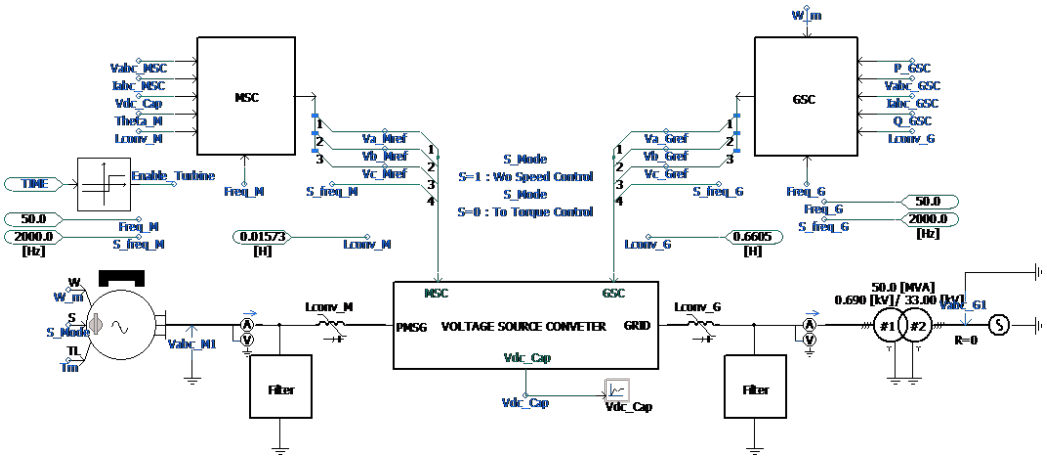

Figure 6.1: Proposed Subsystem

6.1.1 Wind Turbine Model

The PSCAD model of a wind turbine generator's mechanical aspects is depicted in figure 6.2. It involves three inputs: generator speed, pitch angle, and wind speed.

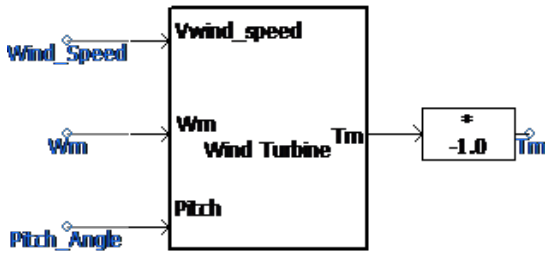

Figure 6.2: Wind Turbine Mechanical Model

In figure 6.3, the tip-speed ratio (λ) is visually depicted, providing a comprehensive representation of the wind turbine. This ratio is obtained by dividing the rational speed in per unit (pu) of the base rotational speed by the wind speed in per unit (pu) of the base wind speed, resulting in the tip speed ratio in per unit of nominal tip speed ($\lambda_{\_nom}$).

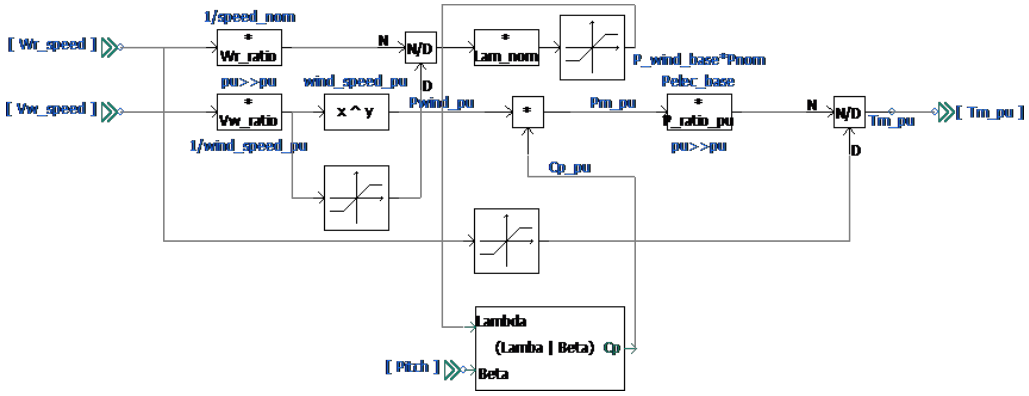

Figure 6.3: Tip Speed Ratio PSCAD model

6.1.2 Voltage Source Converter Block

Figure 6.4 shows the voltage source converter block.

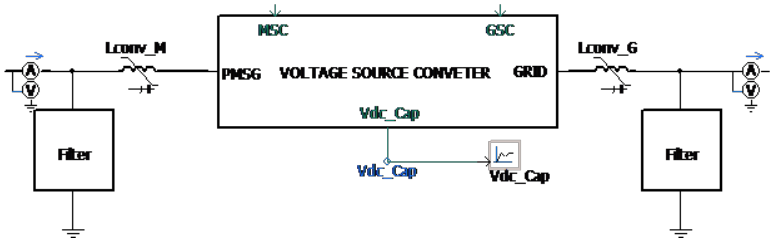

Figure 6.4: Voltage source converter block

In figure 6.5, the 5L NPC converter simulation model is depicted, situated within the voltage source converter block.

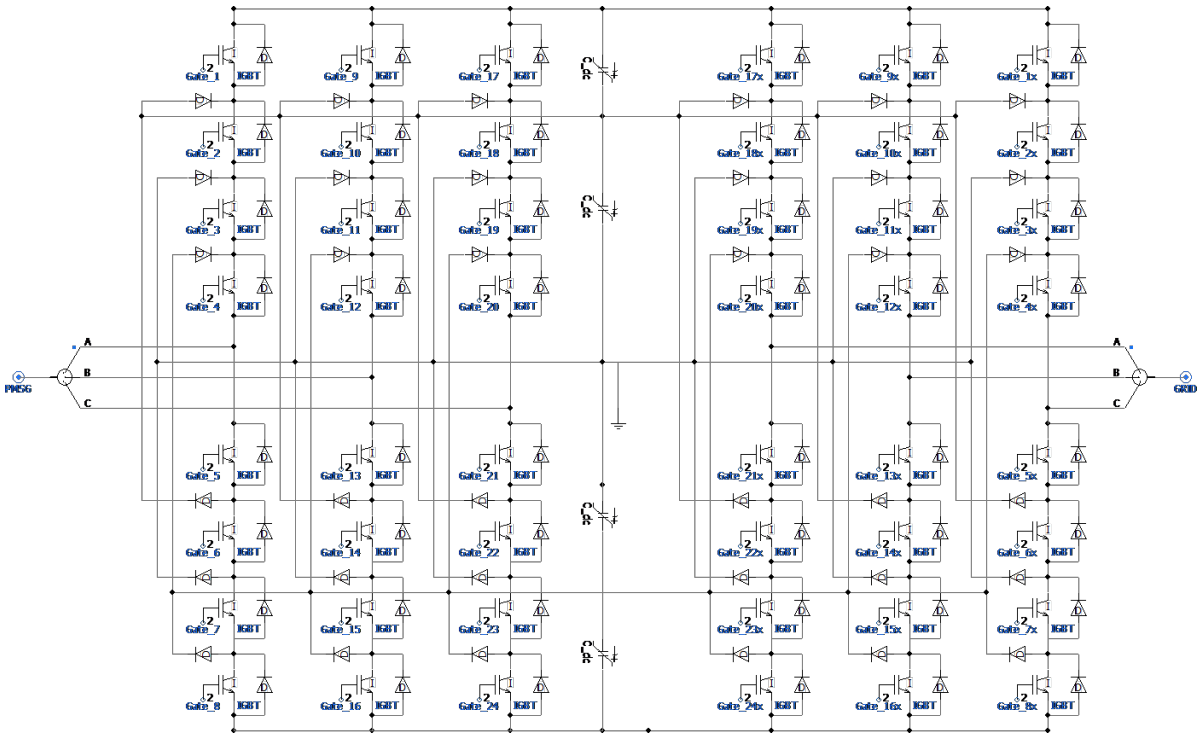

Figure 6.5: 5L NPC converter model

6.1.3 Machine Side Controller

The MSC controller is responsible for stabilizing the DC-link voltage and ensuring a constant stator voltage at the rated value, thereby preventing any possibility of over-voltage. Figure 6.6 illustrates the machine-side control block, which is instrumental in achieving these objectives.

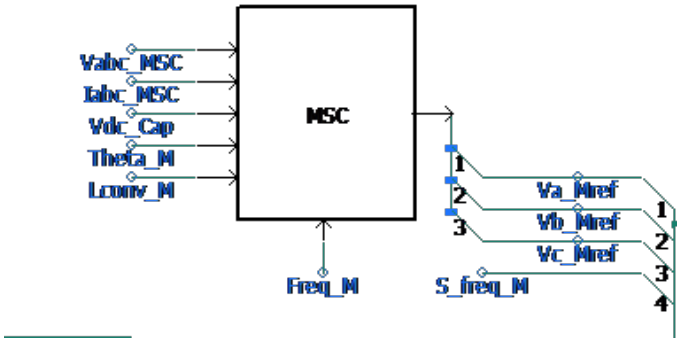

Figure 6.6: Machine-side controller block

Figure 6.7 illustrates the process of per-unitization and transformation of measured current and voltage. Subsequently, as demonstrated in Figure 6.8, the output from the outer loop control is utilized to generate the input inner current references. To enhance the quality of the *dq* values, high reject filters with a characteristic frequency of 360 Hz are incorporated, effectively filtering out some of the power electronic converter's high-frequency harmonics. This filtration process helps in improving the overall performance and efficiency of the system.

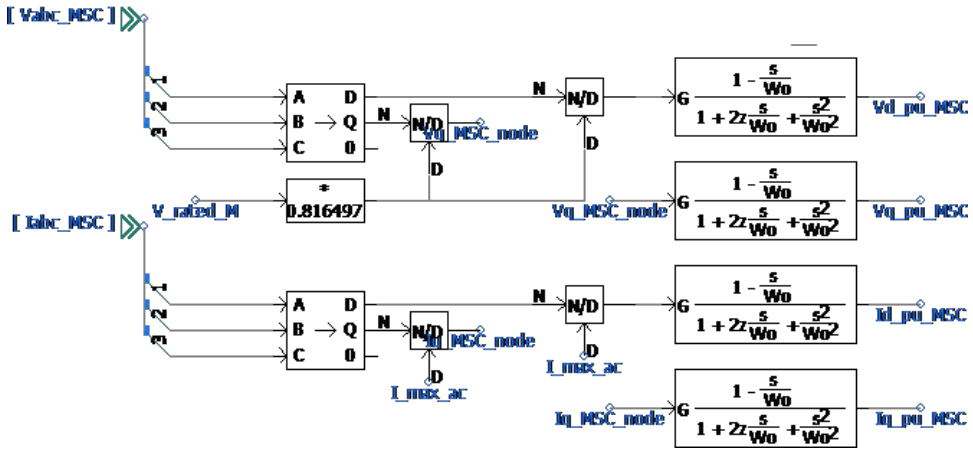

Figure 6.7: Current per-unitizing and transformation from abc to dq0

The outer control loops of the machine-side converter controller play a crucial role in generating the *dq* components of the stator's reference current. Figure 6.8 depicts the control loops for the DC-link voltage and stator voltage, which are integral parts of the machine-side converter controller. to the overall stability and efficiency of the system.These control loops are responsible for regulating the DC-link voltage and maintaining the stator voltage at the desired reference values, contributing

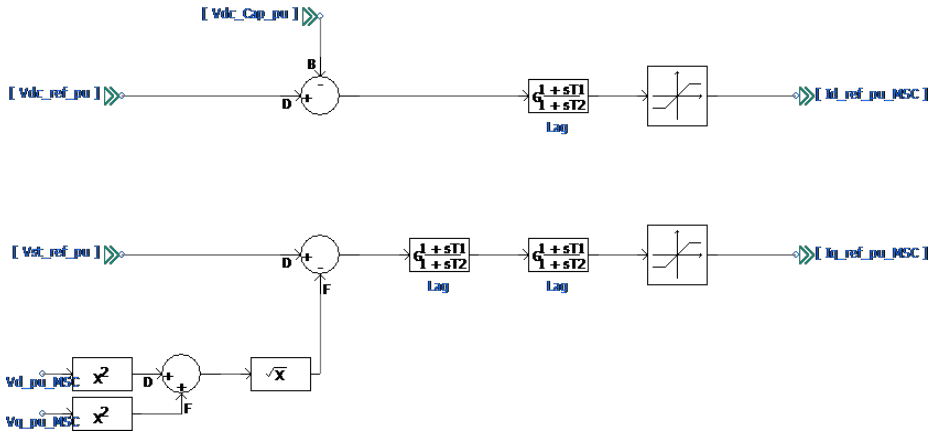

Figure 6.8: MSC Outer Voltage Control Loop

The lag blocks within the system act as phase-lag compensators, while the lead blocks function as phase-lead compensators. The DC-link voltage control loop is responsible for generating the d-component of the stator's reference current, while the stator voltage control loop generates the q-component. These output signals, denoted as (U_{d_ref}) and (U_{q_ref}), from the inner current control loops, are then fed into the PWM block. Figure reffig:MSC Inner current loop control provides a detailed representation of the internal current control loops of the machine-side converter. These control loops are instrumental in accurately regulating and controlling the stator's current components, ensuring optimal performance and stability of the system.

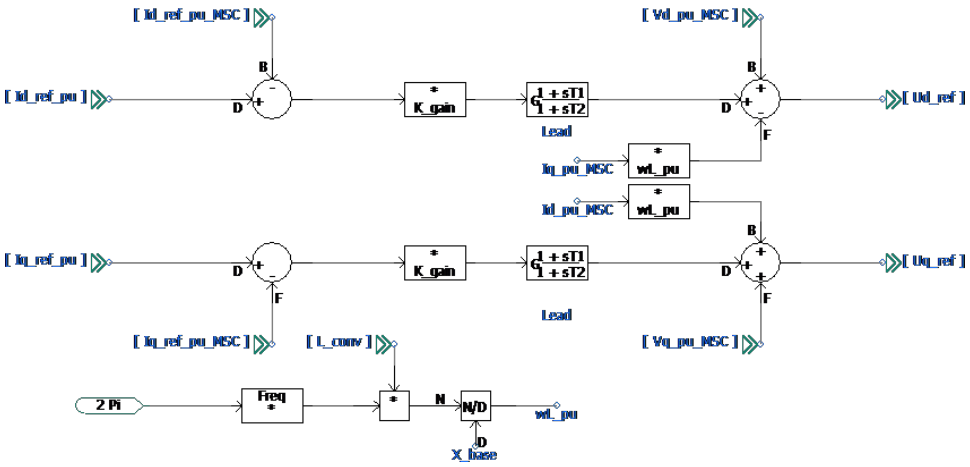

Figure 6.9: MSC Inner current loop control

In figure 6.10, the reference voltages generated by the machine-side controller are depicted. These reference voltages, denoted as U_{d_ref} and U_{q_ref}, are polarized from the rectangular domain, where their magnitudes (M) are per unitized and constrained to 0.85 pu by employing a saturation component. This ensures that the generated reference voltages remain within safe and controllable limits, contributing to the stable operation of the system.

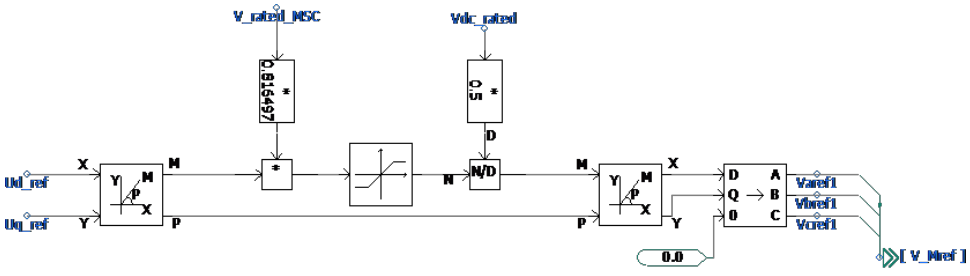

Figure 6.10: MSC reference voltages provided by machine-side controller

By applying the $dq0$ to abc transformation to U_{d_ref} and U_{q_ref}, using ThetaPLL as the conversion angle, the three-phase reference voltage waveforms are obtained. The AC voltage peak to ground serves as the base voltage throughout the process of constructing the reference wave-shapes in per-unit terms. This method ensures consistency and allows for accurate representation of the reference voltages in the three-phase system, facilitating smooth and efficient operation of the system.

6.1.4 Grid Side Controller

The controller employed on the grid-side converter is designed with the objective of extracting the maximum possible power from the wind source. Additionally, the controller is responsible for regulating the reactive power supplied to the grid to ensure a unity power factor. This dual functionality enables efficient power extraction from the wind source while maintaining a balanced and stable grid operation, optimizing the overall performance of the system.

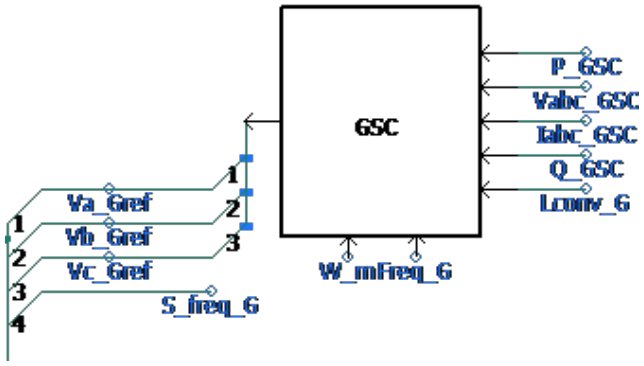

Figure 6.11: Grid-side controller block

In figure 6.12, the per-unitization and transformation of measured current and voltage are illustrated. As shown in figure 6.13, the output from the outer loop control is utilized to generate the input inner current references. To enhance the quality of the dq values, high reject filters with a characteristic frequency of 360 Hz are integrated, effectively filtering out some of the high-frequency harmonics introduced by the power electronic converter. This filtration process improves the accuracy and performance of the system, ensuring smooth and reliable operation.

The outer control loops of the grid-side converter controller are responsible for generating the d and q components of the grid's reference current. In Figure 6.13, the Lag blocks are used to represent phase-lag compensators. The active power and reactive power control loops are depicted in the same figure. The reactive power control loop generates the q-component of the grid's reference current, while the MPPT control loop produces the d-component of the grid's reference current. By effectively managing the active and reactive power components, the grid-side converter controller ensures efficient power extraction from the wind source while maintaining a balanced and stable grid operation.

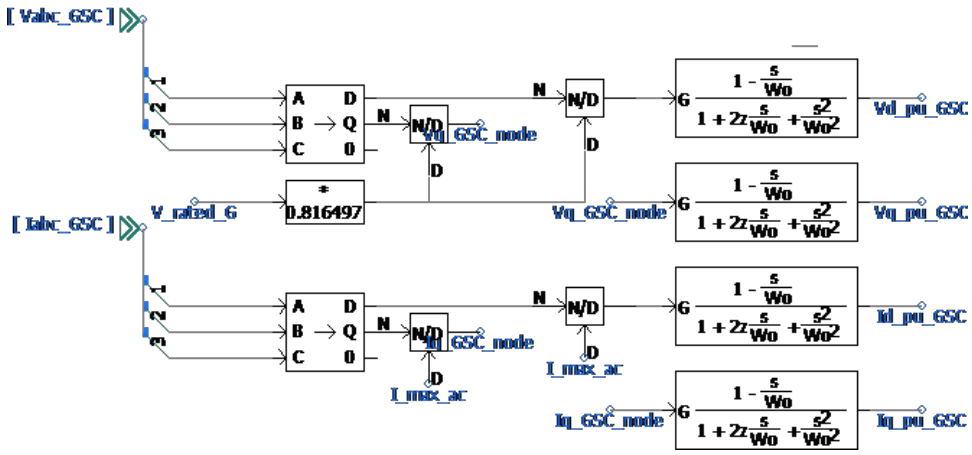

Figure 6.12: GSC current per-unitizing and transformation from abc to dq0 and PLL

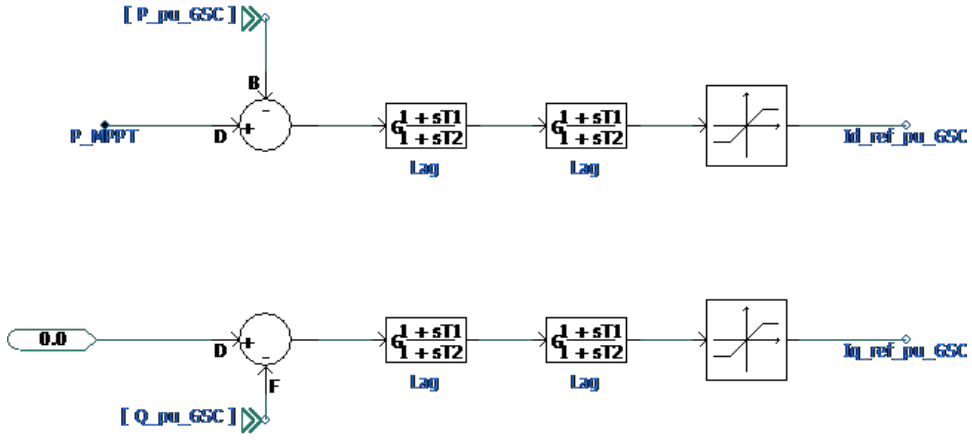

Figure 6.13: GSC outer control loop

Figure 6.14 shows the grid-side converter's inner current control loops.

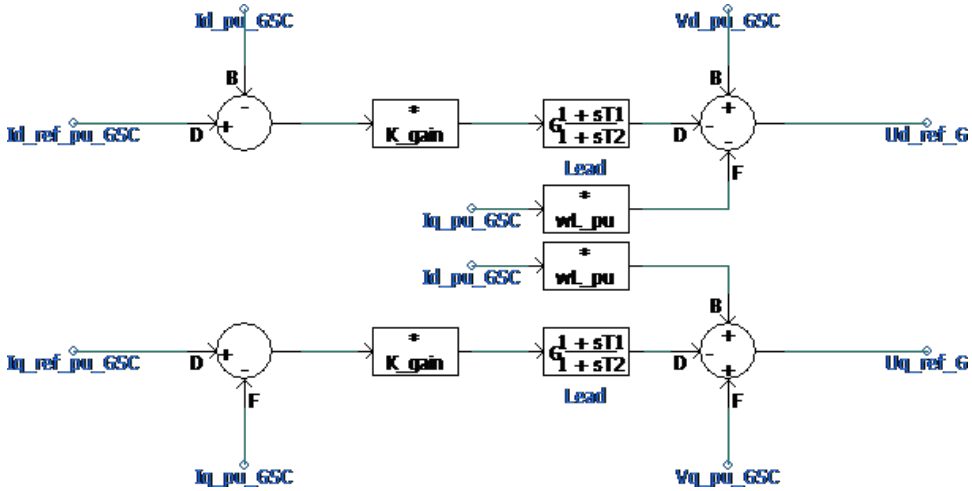

Figure 6.14: GSC inner current control

Indeed, the Lead blocks in the system serve as representations of phase-lead compensators. The output signals $U_{d\_ref\_G}$ and $U_{q\_ref\_G}$ obtained from the inner current control loops are utilized as inputs into the transformation block. This transformation block is responsible for generating the *abc* references for the PWM block. By processing these signals, the transformation block ensures that the appropriate control signals are sent to the PWM block, which then regulates the grid-side converter's operation accordingly, achieving the desired grid connection and power flow control.

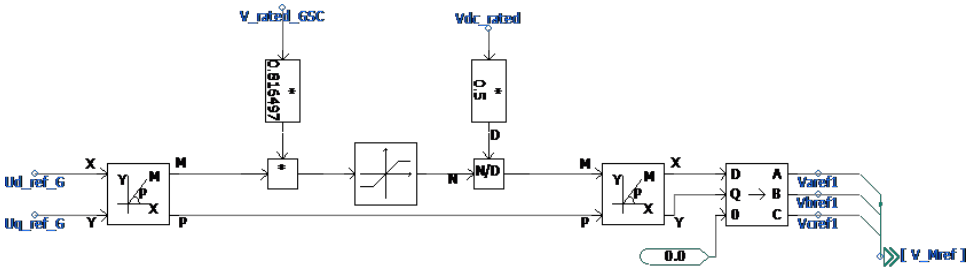

Figure 6.15: GSC reference voltages provided by machine-side controller

6.1.5 Pulse Width Modulation Block

In this study, the PD-PWM technique has been implemented. The PD-PWM method enables the generation of load voltage and current with reduced harmonic distortion. Figure 6.16 illustrates the PD carrier arrangement used in the implementation. By employing this modulation technique, the system aims to enhance the overall power quality, minimize harmonic distortions, and improve the efficiency of the power conversion process.

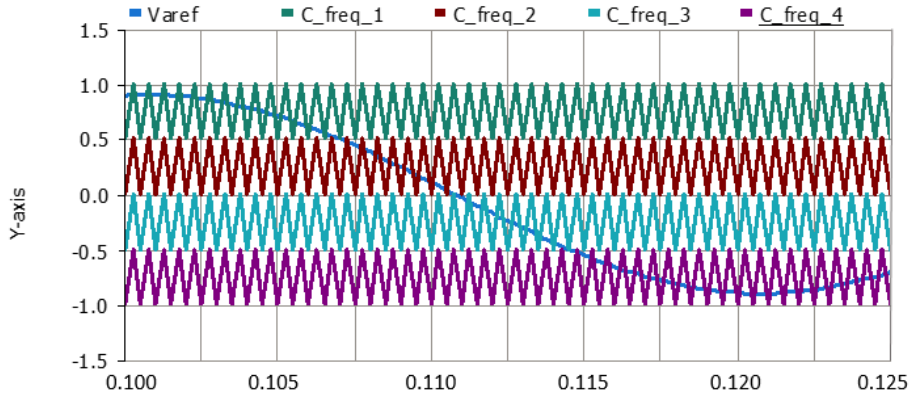

Figure 6.16: Phase Disposition Carrier Arrangement

6.1.6 Phase-Locked Loop Block

Figure 6.17 show the PLL model used to generate the angle for grid-side control

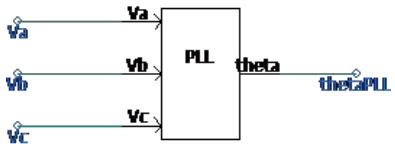

Figure 6.17: Phase Locked Loop PSCAD model

The observed grid voltages and currents undergo transformation using the Clarke and Park Transformations, which convert the 3-phase *abc* reference frame to the *dq* synchronous reference frame. This transformation is carried out using the angle received from the Phase-Locked Loop (PLL). The PLL-generated angle theta is illustrated in figure 6.18. By utilizing this angle in the transformation process, the system achieves synchronization between the grid-side converter and the grid, enabling accurate control and regulation of the grid-connected operation.

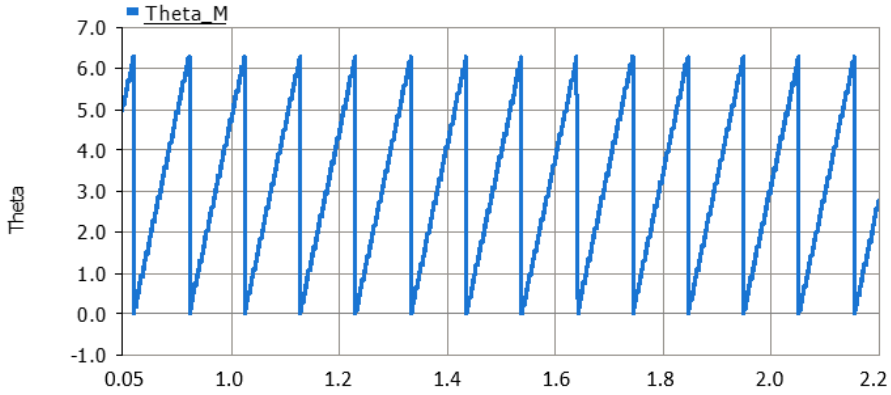

Figure 6.18: Angle theta generated by the PLL

6.2 Chapter Summary

The main focus of this chapter was the development and implementation of all the key components of the proposed WECS and the associated controller schemes, namely the MSC and GSC control. These components were designed and simulated using the PSCAD software. By thoroughly exploring and validating the performance of the WECS and its control strategies within the simulation environment, this chapter aimed to provide valuable insights and a solid foundation for the practical implementation of the system.

Chapter 7

Results and Discussion

7.0.1 Introduction

This chapter presents the simulation results of the proposed WECS obtained from PSCAD software package. The dynamics behaviour of the WECS is analysed based on this time intervals listed below:

- The wind turbine is enabled at $t = 0.1s$.
- The wind turbine speed experienced drastically change at $t = 2.5s$.

7.0.2 Wind Turbine Results

Wind Speed

Since the wind does not change instantly in reality, it is accelerated in this study to examine the effects of a major shift in wind speed from 8 m/s to 16 m/s at the time interval of $t = 2.5s$, as shown in Figure 7.1.

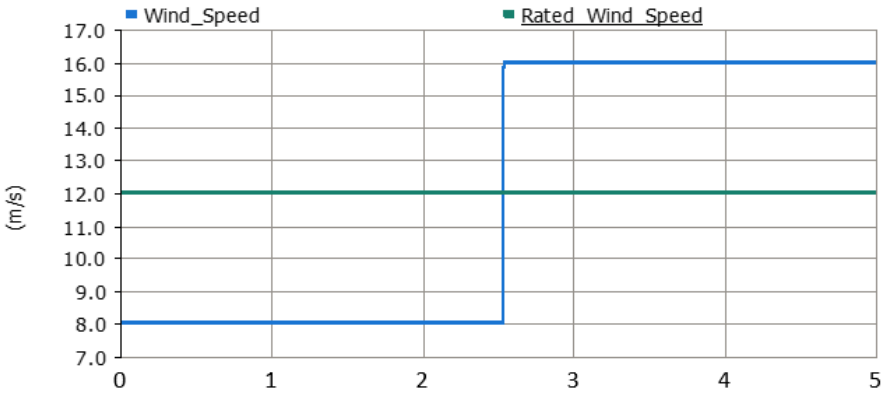

Figure 7.1: Wind profile

-

7.0.3 Mechanical Angular Speed

Initial response (t = 0.1 seconds): When the wind turbine starts operating, the rotor speed initiates with rapid acceleration, reaching its rated speed (1 pu) in a short duration. This initial burst is common as the turbine adapts to the starting conditions and the available wind energy.

Steady-state adjustment: After the initial burst, the rotor speed gradually adjusts to a new equilibrium to match the wind speed. In this case, the wind speed is specified as 8 m/s. The rotor speed of the turbine tends to stabilize to a level that maximizes the energy extracted from the wind while maintaining stability and efficiency.

Response to drastic wind speed change (t = 2.5 seconds): At 2.5 seconds, the wind speed changes, prompting the rotor speed to respond accordingly. The rotor speed increases at a rate that complements the change in wind speed. This response is crucial for maintaining the turbine's efficiency and stability, as it ensures that the rotor speed remains synchronized with the wind, maximizing energy capture.

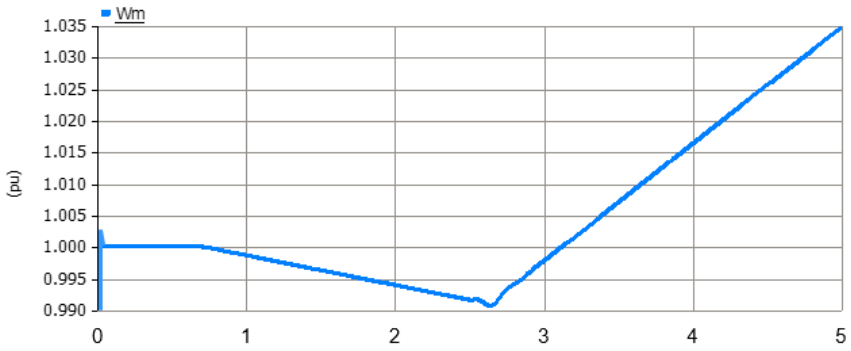

Figure 7.2: Angular speed

7.1 Permanent Magnet Synchronous Generator (PMSG) Results

7.1.1 Power Curves

Regarding a change in wind speed, the active and reactive power generated by the PMSG increase. At $t = 2.5s$, as the power production rises, the reactive power is increased again to prevent a voltage surge. This relationship can be expressed by the following equations:

$$P = VI\cos\theta \tag{7.1}$$

$$Q = VI\sin\theta \tag{7.2}$$

As the active power (P) increases, both voltage and current rise proportionally due to their direct relationship. However, to maintain a constant voltage level, the reactive power (Q) also increases, compensating for the rise in voltage caused by the increase in active power. This mechanism ensures voltage stability despite fluctuations in active power. Consequently, the current rises symmetrically with the active power, resulting in a balanced and stable system operation. This control strategy ensures efficient power utilization and seamless integration with the grid for the WECS in response to varying wind conditions.

Due to machine dynamics, the initial power generated at a wind speed of 8 m/s exhibits ripples at $t = 0.1s$, but the controller rapidly stabilizes it afterward, as evident from both figures below. Initially, the reactive power ramps up to support the voltage being generated, as shown in Figure 7.4. Subsequently, as anticipated, it gradually decreases until it reaches nearly zero. At $t = 2.5s$, when the wind speed changes from 8 m/s to 16 m/s, the active power steadily increases as it adapts to the new wind conditions, as depicted in Figure 7.3. To prevent the voltage from rising excessively with the increase in power production, the reactive power rises once again at $t = 2.5s$, effectively maintaining voltage stability.

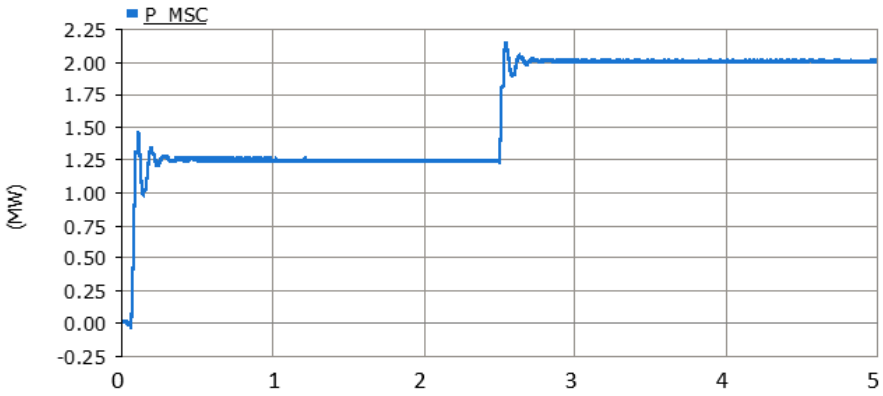

Figure 7.3: PMSG active power with the wind speed varied

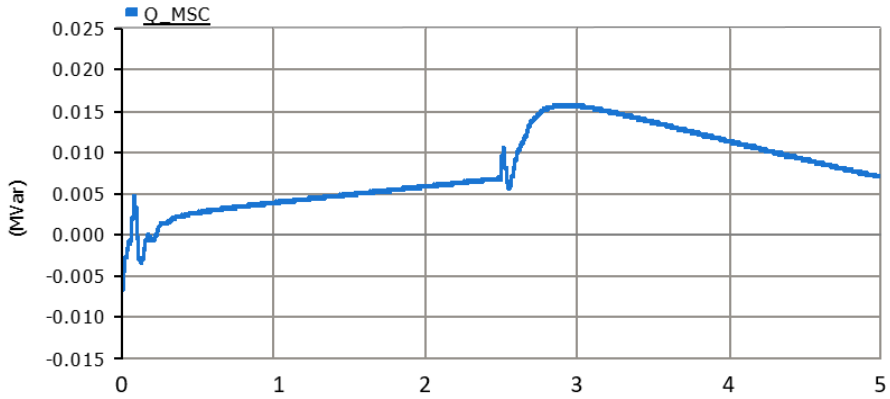

Figure 7.4: PMSG reactive power with the wind speed varied

Power factor at the wind speed of $8 - 16$ m/s

The measured active and reactive power at $t = 1.5$ s where,
$P_{_MSC} = 1.25$MV and
$Q_{_MSC} = 0.005$MVar respectively.

Therefore, the power factor (PF) is:

$$\theta = \tan^{-1}\left(\frac{Q_{\_MSC}}{P_{\_MSC}}\right) \tag{7.3}$$

$$\theta = \tan^{-1}\left(\frac{0.005}{1.25}\right)$$

$$PF = 0.999$$

The rated power factor of 0.8921, as derived from the specifications in chapter 5, indicates the expected power factor of the system. With the implementation of the 5L NPC VSC on the stator transmission side, the power factor can be significantly improved to around 0.9999. The 5L NPC VSC is designed to enhance power factor correction and improve overall power quality. By effectively compensating for reactive power and providing precise voltage control, this converter ensures the power factor approaches unity (0.9999), signifying a highly efficient and near-ideal power factor for the WECS.

7.1.2 Torque

In the steady state, the electromagnetic torque produced by the generator is equal in magnitude but opposite in direction to the mechanical torque, as depicted in Figure 7.5. This relationship is mathematically expressed by Eq.(7.4), which was elaborated in detail in Chapter 3.

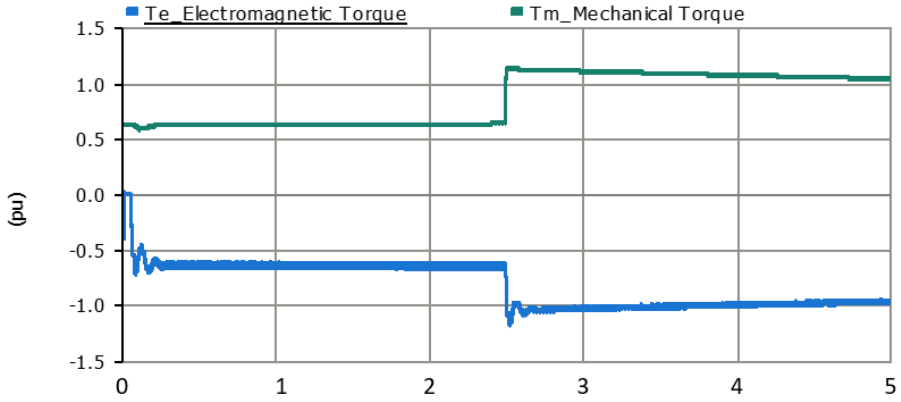

Figure 7.5: PMSG Electromagnetic and Mechanical Torque

$$T_m = -T_e = \frac{3}{2} i_{sq} \psi_{PM} \tag{7.4}$$

This equation indicates that the electrical and mechanical torques are counteracting each other, resulting in a stable equilibrium state where the generator operates smoothly and efficiently. The torque produced by electromagnetic forces is directly proportional to the q-component of the stator current, as described in Eq.(7.4). Figure 7.7 displays the connection, providing an illustration of the effective dynamics of the generator-side controller.

At the rated power of 2 MW, the torque is nearly equal to the rated torque of the wind turbine generator, which is 849kNm (1 pu). This mathematical verification can be performed as follows:

$$T_m = \frac{P_m}{\omega_{r\_m}} = \frac{2 \times 10^6}{2.356} = 848\text{kNm}$$

7.2 Machine-Side Converter Control

7.2.1 Stator dq Component Currents

Figure 7.6 and Figure 7.7 illustrate the measured stator currents, which closely follow the reference stator currents derived from the DC-link voltage control loop. Initially, the controller displays a slight overshoot but then effectively tracks the reference currents without any deviation until $t = 2.5s$. At this point, when the power output increases, the controller momentarily loses track of the reference currents but quickly regains it. As the power output continues to rise, the controller seamlessly matches the reference current with precision.

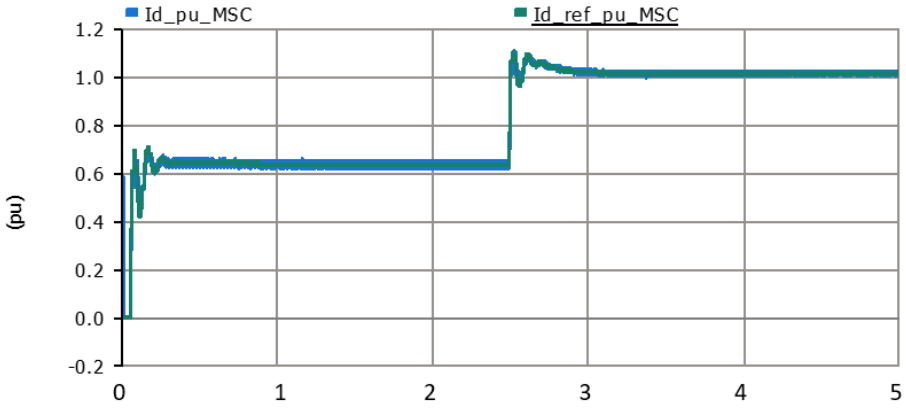

Figure 7.6: Stator d component currents

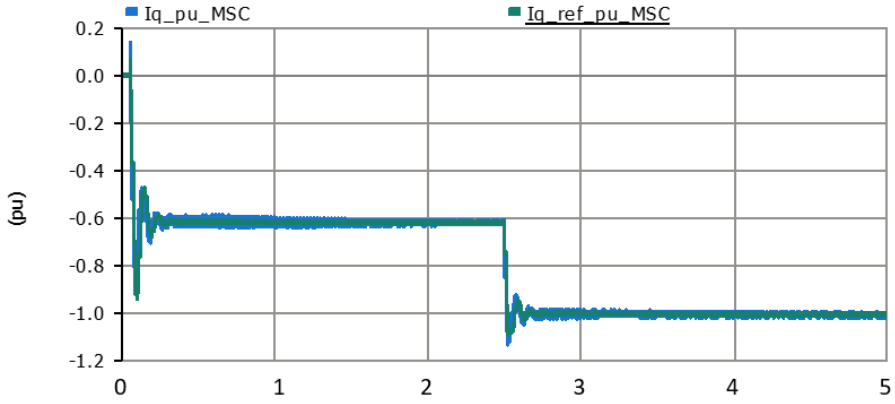

Figure 7.7: Stator q Component Currents

Consequently, the effectiveness of the inner current controllers is demonstrated by the measured current values' ability to maintain currents within acceptable limits while accurately tracking the reference currents obtained from the outer control loops.

7.2.2 Stator *abc* Currents and Voltage

Below are the wave-forms of the *abc* stator current and voltage, depicted in Figure 7.10 and Figure 7.8, respectively. To minimize the risk of over-voltages, the stator voltage is controlled to remain within ±5% of its rated value. Starting from the rated line-line voltage of 690V, the rated stator phase voltage (rms) can be determined as follows:

$$V_{phase(\text{rms})} = \frac{690 \text{ V}}{\sqrt{3}} = 398.37 \text{ V} \tag{7.5}$$

Its can be observed in figure 7.8 that the voltage is maintained to within the expected range of 378.45V to 418.29V.

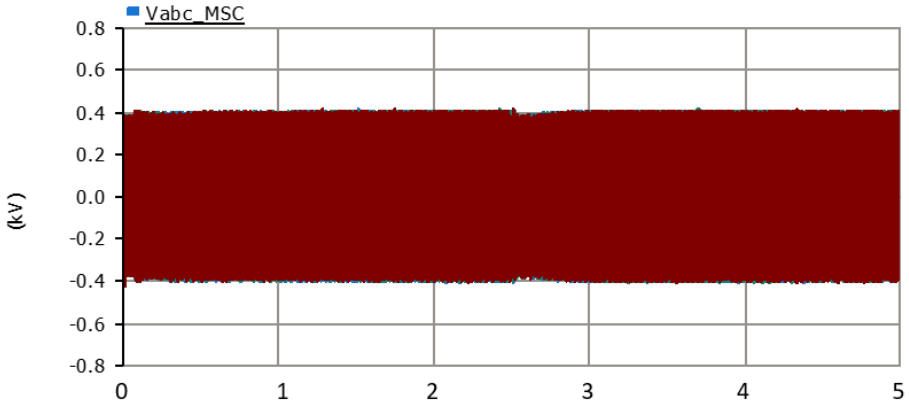

Figure 7.8: Stator *abc* voltage waveform

Figure 7.9 shows the *abc* zoomed stator voltage with good waveform which is within the accepted

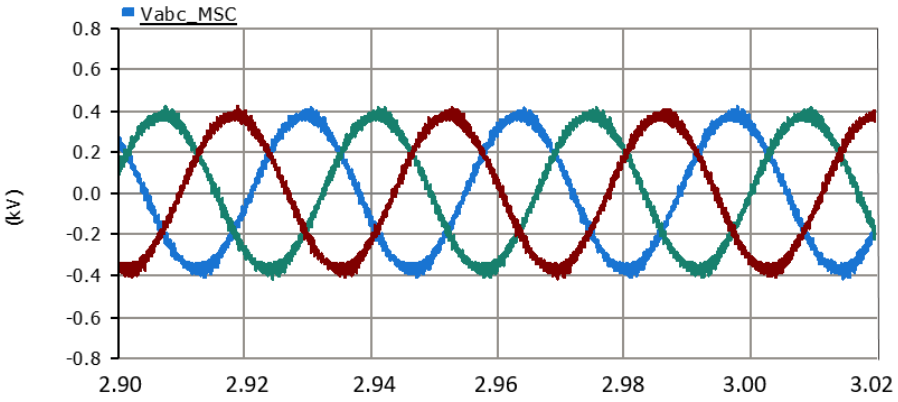

Figure 7.9: Zoomed stator *abc* voltage waveform

Figure 7.8 shows the *abc* stator current waveform, with a relative change in *dq* current components at $t = 2.5s$.

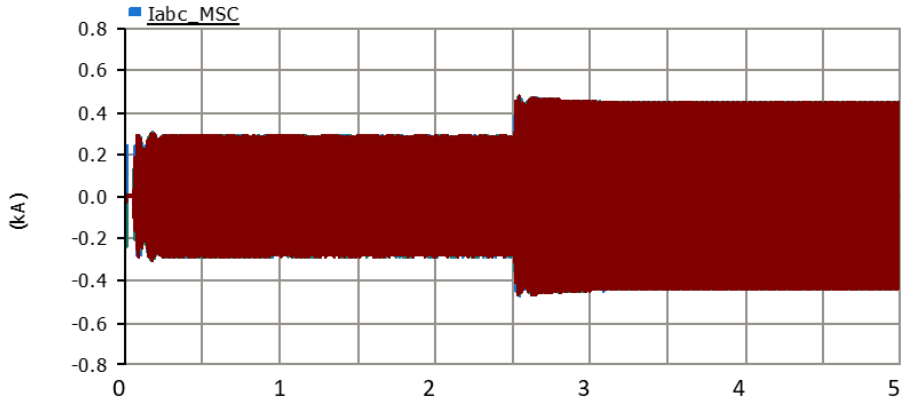

Figure 7.10: Stator *abc* current waveform

Figure 7.11 shows the *abc* zoomed stator current with good waveform which is within the accepted performance.

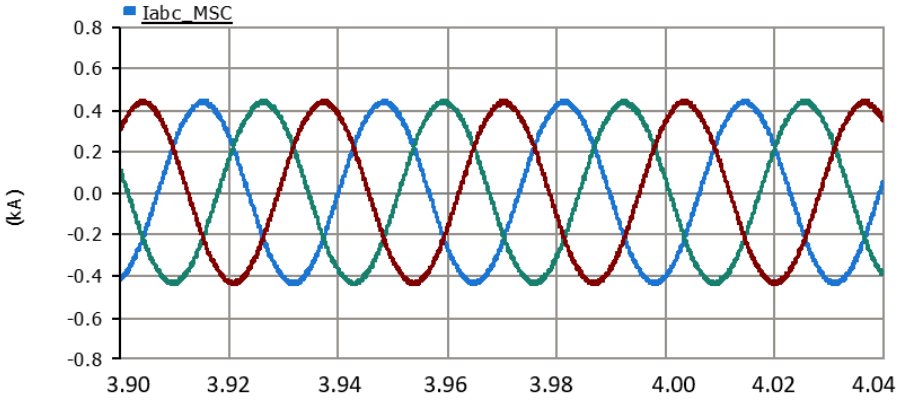

Figure 7.11: Zoomed stator *abc* current Waveform

7.2.3 DC-Link Voltage

The DC voltage controller effectively keeps the DC voltage close to the expected range of 1126.77V. It successfully counteracts the changes that occur when the wind turbine is activated at $t = 0.1$ and $t = 2.5$ seconds, as demonstrated in Figure 7.12. During these transients, overshoots can be observed, and there is a settling time before reaching a steady state. These behaviors arise from machine dynamics; however, the controller promptly stabilizes the voltage and brings it back to its intended level.

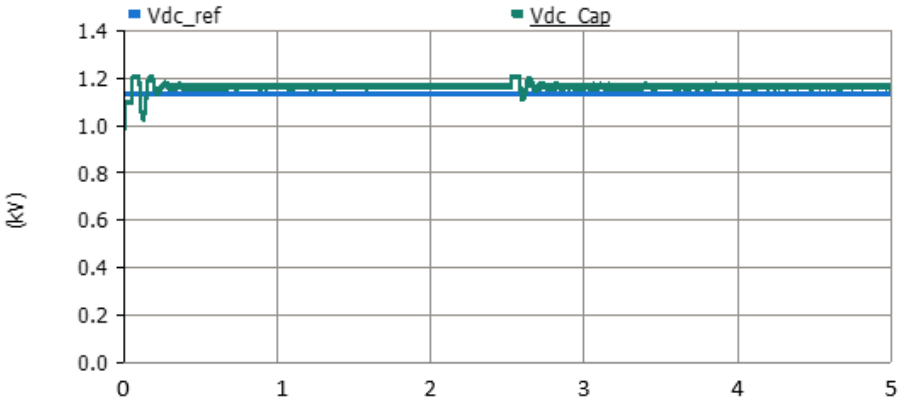

Figure 7.12: DC-Link voltage

7.3 Grid-Side Converter Control

7.3.1 Power Curve

The initial power generated at the speed of 8m/s has double overshoot in the first $t = 0.1s$ owing to machine dynamics, but the controller rapidly resolves it thereafter. The graphs in Figure 7.13 display some significant data, including the fact that the electricity generated by the PMSG system is perfectly transferred from the converter to the grid. This important observation validates the relationship between the converter power and the grid power:

$$P_{dc} = P_{ac} = I_{dc}V_{dc} \tag{7.6}$$

At $t = 2.5s$, the VSC grid-side converter becomes the source of voltage and maintains a constant reactive power output by adjusting the modulation index, denoted by m, which modifies the output voltage. The relationship between the grid voltage and the DC voltage is described by equation Eq 7.7. To keep the voltage constant while the active power increases, the VSC swiftly adapts the modulation index m, allowing for precise voltage regulation.

$$V_g = (V_{dc})(m)\frac{\sqrt{3}}{2\sqrt{2}} \tag{7.7}$$

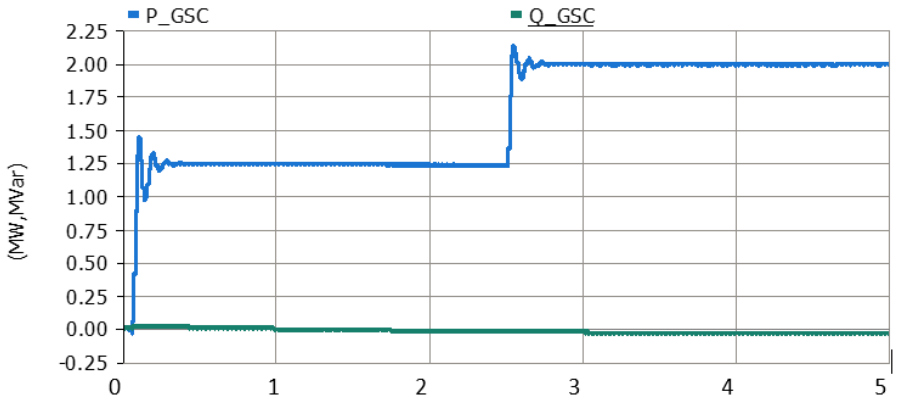

Figure 7.13: Active and reactive power Curves

7.3.2 Grid dq Current and Voltage Components

The active power exchange between the VSC and the grid system can be presented by $dq0$ reference as given by Eq 7.8.

$$P_{grid} = \frac{3}{2}\left(V_{gd}i_{gd} + V_{gq}i_{gq}\right) \tag{7.8}$$

In the $dq0$ axis, it is assumed that V_{gd} perfectly synchronizes with the d-axis, as depicted in Figure 7.14. Consequently, $V_{gq} = 0$. As a result, the power transfer can be expressed as follows:

$$P_{grid} = \frac{3}{2}V_{gd}i_{gd}$$

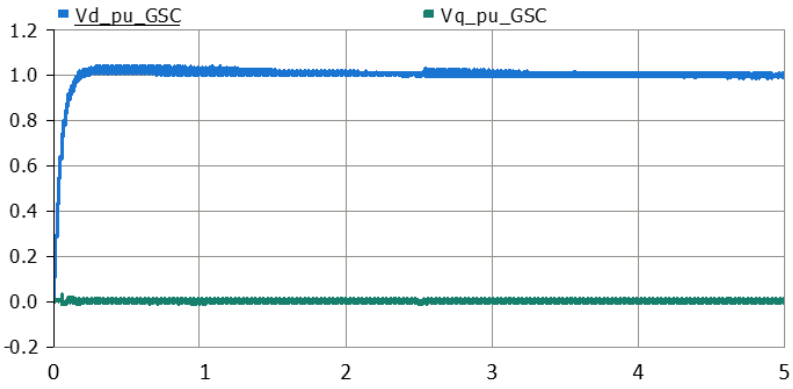

Figure 7.14: Grid voltage dq-components

So, it can be deduced that the grid current d-component is directly controlled by the active power of the grid as shown in Figure 7.15.

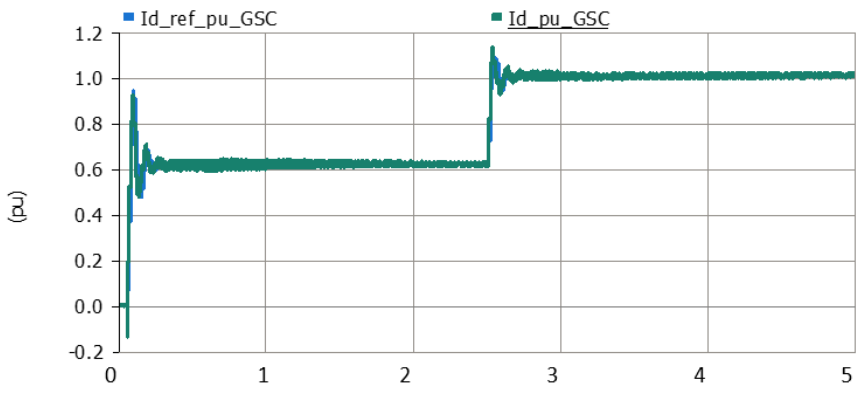

Figure 7.15: Grid current d-component

Similarly, the reactive power exchange between the VSC and the grid system can be presented by dq reference as given by Eq 7.9.

$$Q_{grid} = \frac{3}{2}\left(V_{gd} i_{gd} - V_{gq} i_{gd}\right) \tag{7.9}$$

In the $dq0$ axis, the V_{gd} is assumed to be perfect synchronism with d-axis as verified in figure 10. hence $V_{gq} = 0$. Therefore the power transfer is given as Eq 7.10.

$$Q_{grid} = \frac{3}{2}\left(V_{gd} i_{gq}\right) \tag{7.10}$$

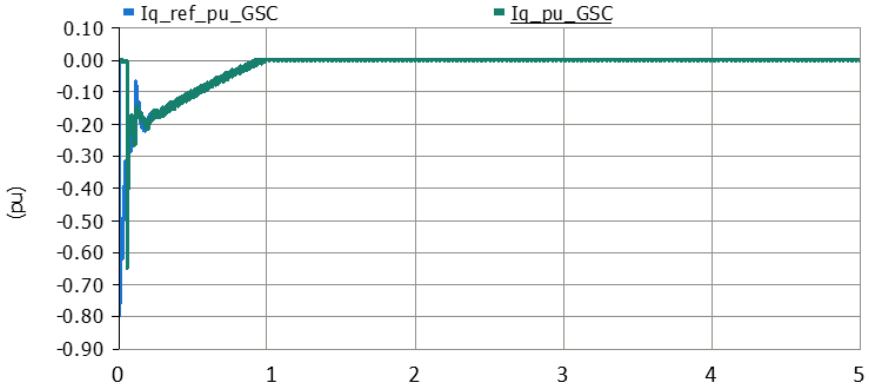

Figure 7.16: Grid current q-component and reference

In Figure 7.16, It is observed that the q-component of the grid current is kept to a minimum and close to zero to ensure that the reactive power absorbed or generated by the converter is also kept to a minimum to ensure unity power factor.

7.3.3 Converter Terminal Voltage and Current

Based on Figure 7.17, the output phase voltage of the grid-side converter is 415V. Consequently, the line-to-line voltage is equal to 652.26 V_{rms}. When calculating the line current, the active power of the 2MW wind turbine generator is taken into account.

$$P = \sqrt{3} V_L I_L \cos\theta \tag{7.11}$$

$$I_{rms} = \frac{2 \times 10^6}{652.26 \times 0.9\sqrt{3}} = 655.67 \text{ A}$$

The *abc* converter voltage graph is shown in Figure 7.17 below.

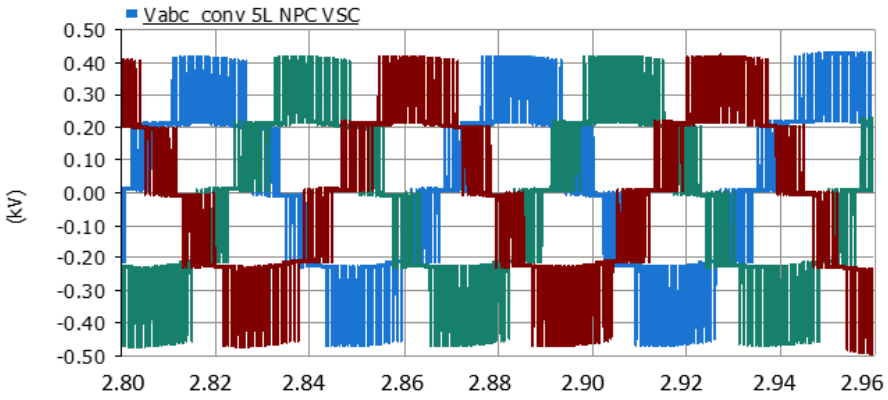

Figure 7.17: Converter *abc* output voltage

The *abc* converter current graph is shown in Figure 7.18 below.

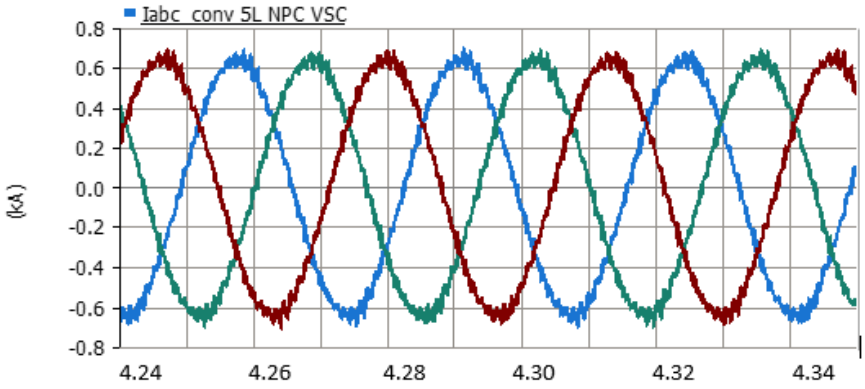

Figure 7.18: Converter *abc* output current

7.4 Grid *abc* Current and Voltage at POC

Figure 7.19 displays the abc POC current graph. It has a decent waveform and performs within the range expected.

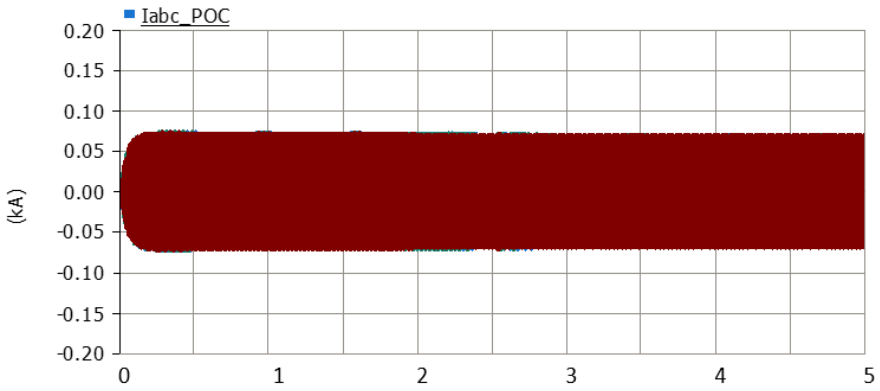

Figure 7.19: Grid *abc* current at POC

The zoomed abc current at the POC is shown in the Figure 7.20 below. The waveform is clearly displaced 120 degree.

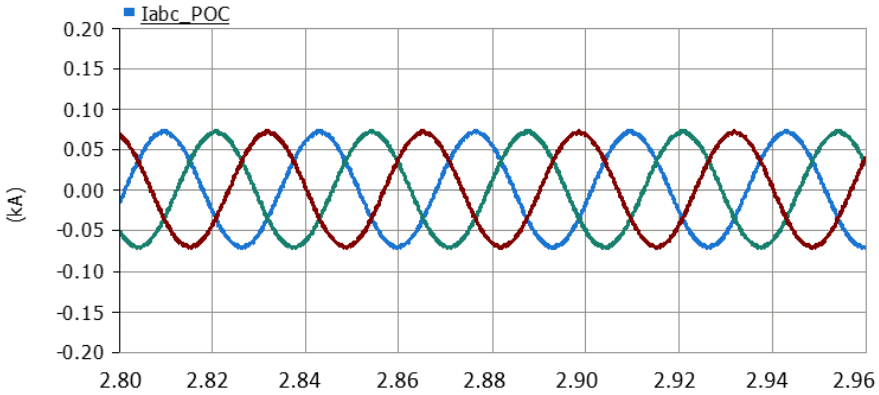

Figure 7.20: Zoomed *abc* Current at POC

The *abc* grid voltage graph is shown in Figure 7.21 below. It has a good waveform which is within the accepted performance.The voltage at POC $\pm 5\%$ 33k V

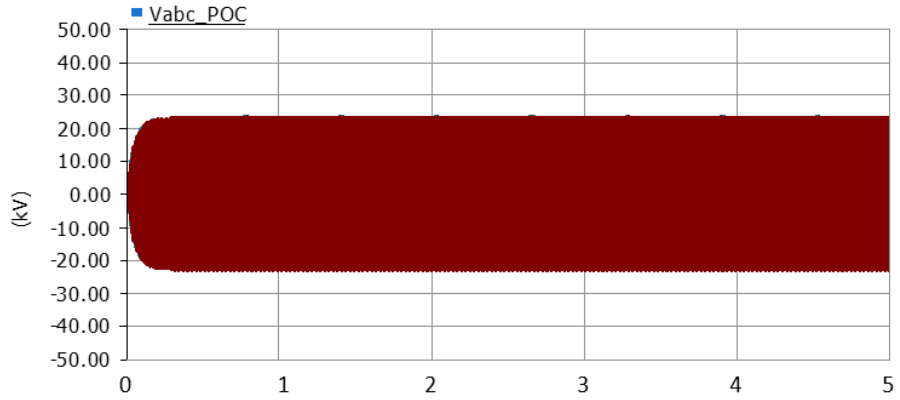

Figure 7.21: Grid *abc* Voltage at POC

The zoomed abc voltage at the POC is shown in the Figure 7.22 below. The waveform is clearly displaced 120 degree.

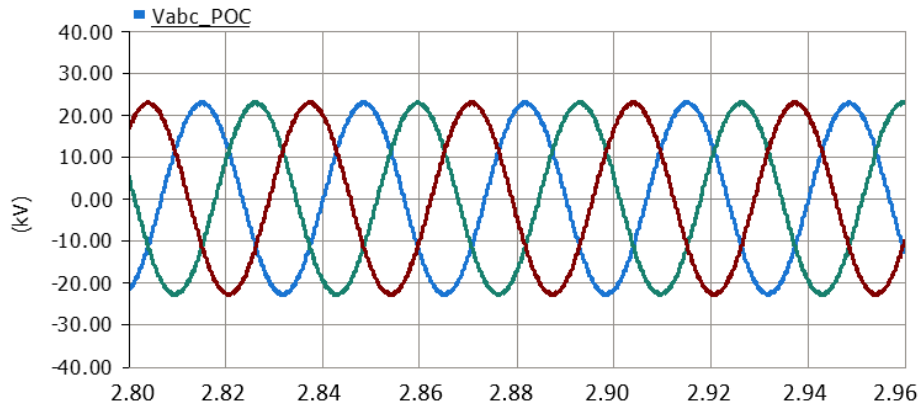

Figure 7.22: Zoomed Grid *abc* Voltage at POC

7.5 THD Analysis of 5L NPC and 2L VSC

In this section, a comparative study between 2-level and 5-level NPC converters is presented for a WECS utilizing a PMSG connected to the grid system. The assessment aims to determine the most suitable converter option. As per the International Electrotechnical Commission (IEC) standards, it is crucial to minimize THD to meet the required specifications and ensure system performance is within acceptable limits.

7.5.1 Two Level VSC

Voltage THD

Figure 7.23 and 7.24 present the voltage THD% in phase voltage wave forms and THD% levels during a significant change in wind speed for the 2-level VSC.

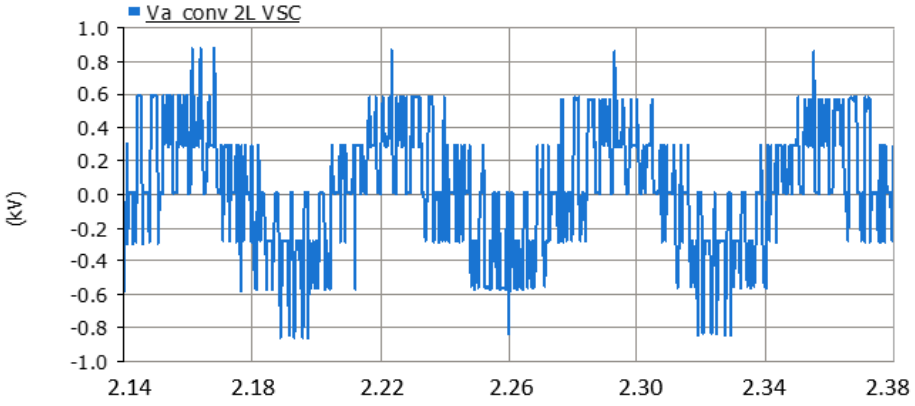

Figure 7.23: Zoomed voltage waveform of a 2L VSC

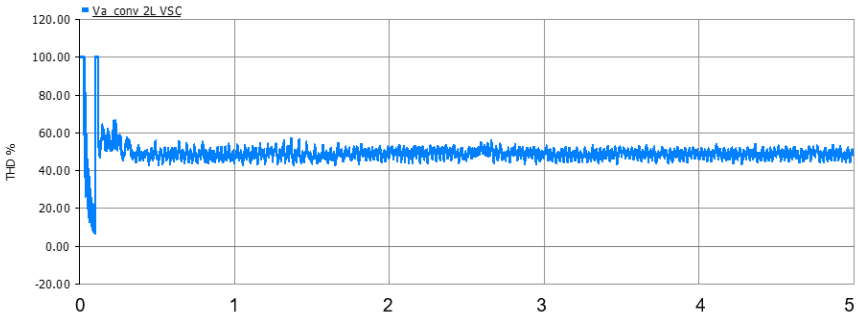

Figure 7.24: 2L VSC Voltage THD %

Current THD

Figure 7.25 shows phase current waveform produced by the 2L VSC.

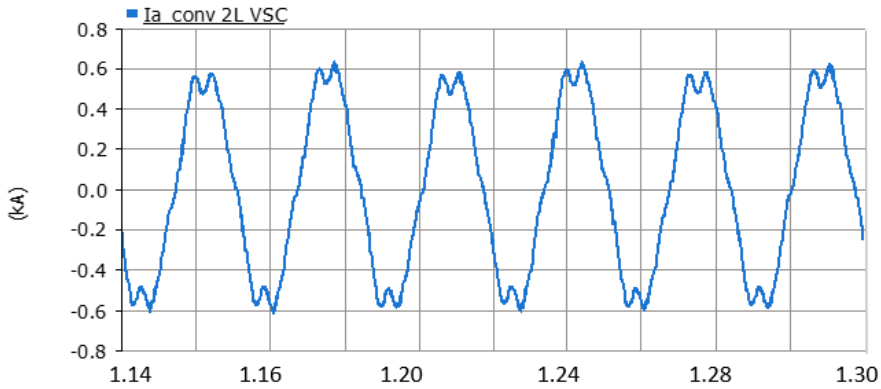

Figure 7.25: Zoomed current waveform of a 2L VSC

Figure 7.26 illustrate the phase current THD % generated during the change in wind speed.

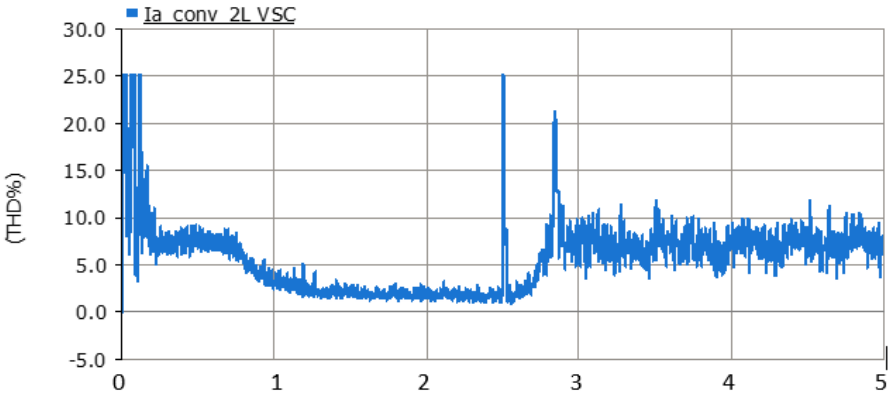

Figure 7.26: 2L VSC Current THD%

As seen in Figure 7.24, the THD% increases simultaneously with the change in wind speed at $t = 2.5$. Additionally, Figure 7.26 displays an overshoot in THD%, which then settles at a new and higher THD% level. Based on these results, it becomes evident that the two-level VSC configuration faces challenges in handling changes in wind speed and reducing THD%.

The observed increase in THD% during varying wind speeds indicates a limitation in the converter's ability to effectively mitigate harmonic distortions under such conditions. The THD% overshoot in the current waveform further highlights the difficulties in maintaining stable and low distortion levels.

7.5.2 5 Level NPC VSC

Voltage THD

Figure 7.27 shows a phase voltage waveform produced by the 5L NPC VSC.

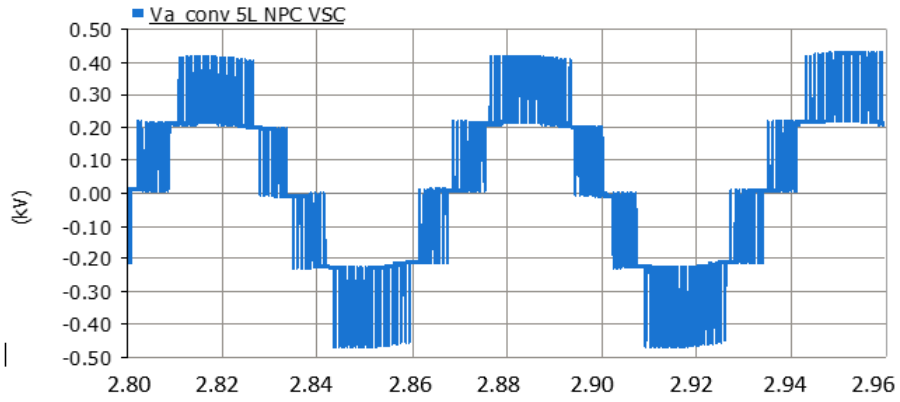

Figure 7.27: Zoomed voltage waveform of a 5L NPC VSC

Figure 7.28 illustrate the phase voltage THD % generated during the change in wind speed.

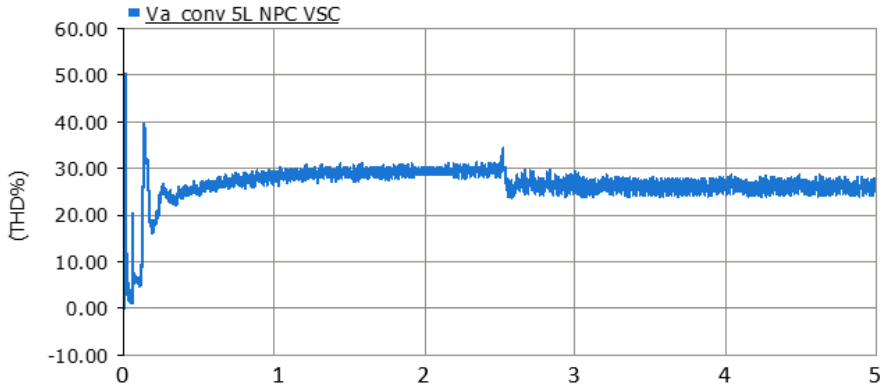

Figure 7.28: 5 NPC VSC Voltage THD%

In Figure 7.28, it is evident that a significant alteration in wind speed occurs at $t = 2.5s$, resulting in a decrease in THD%. This enhancement in THD% is credited to the functionality of the 5-level NPC converter. By employing a larger array of switching pulses, the converter can adapt its pulse modulation more flexibly, thereby swiftly and efficiently reducing THD%.

The presence of more switching pulses in the 5-level NPC converter indeed grants finer control over the output waveform, which proves advantageous in reducing harmonic distortions during transient conditions, such as abrupt changes in wind speed. The converter's ability to adjust its pulse modulation rapidly and flexibly allows it to adapt to the fluctuations in wind speed, thereby ensuring a higher quality output voltage with significantly lower THD% levels.

Current THD

Figure 7.29 shows a phase current waveform produced by the 5L NPC VSC.

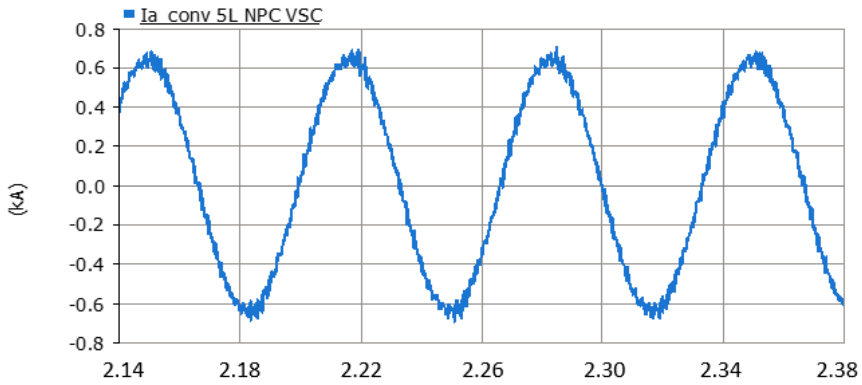

Figure 7.29: Zoomed current waveform of a 5L NPC VSC

Figure 7.30 illustrate the phase current THD % generated during the change in wind speed.

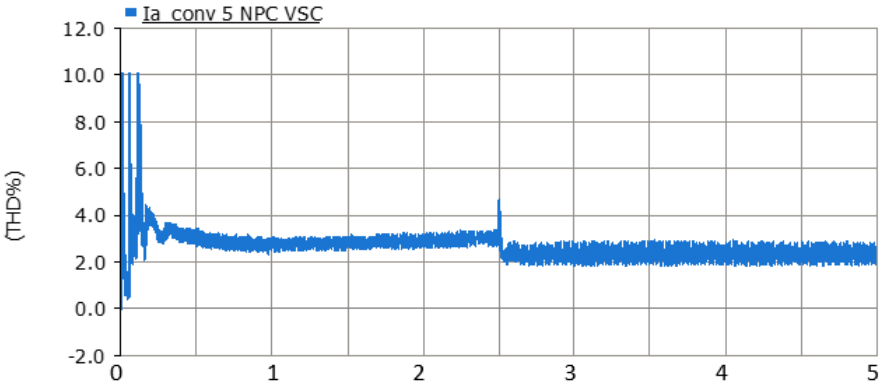

Figure 7.30: 5 NPC VSC current THD%

Similarly to the current,the pulse modulation of 5L NPC adjust, so to reduce THD quickly.

7.5.3 System Efficiency

The efficiency of the WECS-PMSG linked to the 5L-NPC system in cascade configuration as depicted in Figure 7.31 is assessed by measuring the input and output power of each system through simulation.

Figure 7.31: WECS-PSMG, 5L-NPC System

The efficiency of the input power from the wind turbine to the PMSG is calculated as follows.

$$\eta_1 = \frac{P_{MSC}}{P_M} = \frac{1.89 \times 10^6}{2 \times 10^6} = 94.5\% \tag{7.12}$$

The efficiency of the power from the PMSG to the 5L-NPC Converter is calculated as follows.

$$\eta_2 = \frac{P_{GSC}}{P_{MSC}} = \frac{1.83 \times 10^6}{1.89 \times 10^6} = 96.83\% \tag{7.13}$$

The overall efficiency of the WECS-PSMG is calculated as follows :

$$\eta_{overall} = \eta_1 \times \eta_2$$

$$\eta_{overall} = \frac{P_{MSC}}{P_M} \times \frac{P_{GSC}}{P_{MSC}}$$

$$\eta_{overall} = \frac{P_{GSC}}{P_M} = \frac{1.83 \times 10^6}{2 \times 10^6} = 91.5\%$$

Achieving 91.5% system efficiency indicates highly effective energy conversion with minimal losses, reflecting optimized components and advanced engineering. This efficiency ensures reliability, durability, and economic viability, particularly in renewable energy applications like wind turbines, highlighting its importance for sustainability and profitability.

7.6 Chapter Summary

7.6.1 Control Results

In this chapter, we presented the simulation results for the proposed wind energy conversion system, aiming to assess the effectiveness and alignment of the suggested control strategies with the study's objectives. Through comprehensive simulations and analyses, we evaluated the performance of the system under various operating conditions and scenarios.

The simulation findings shed light on the system's behavior, including its response to changes in wind speed, variations in power output, and the impact on voltage and current waveforms. We examined the THD% levels and the capability of the converters to handle transient conditions.

By comparing the outcomes with the study's goals and requirements, we could draw meaningful conclusions about the effectiveness of the proposed control strategies. The results provided valuable insights into the system's stability, efficiency, and ability to meet the specified standards and regulatory requirements. Overall, the simulation findings serve as a crucial validation and verification of the proposed wind energy conversion system, ensuring that the control strategies align with the study's goals and contribute to a reliable and optimized renewable energy solution.

MSC Controller

To ensure a constant flow of active power from the wind turbine to the grid, the DC-link voltage was controlled within acceptable limits, and efforts were made to minimize reactive power transfer for a unity power factor.

GSC Controller

As the wind speed increased, the system successfully achieved maximum power point tracking. Moreover, it demonstrated the capability to regulate both active and reactive power injections into the grid.

7.6.2 THD Results

Table 7.1 and Table 7.2 provide the results of the THD analysis for the 2L VSC and 5L NPC converters, respectively. Both converters utilize the same proposed control strategy and possess identical system rated parameters. The tables present detailed information on the THD% under various operating conditions of drasticaly change of wind speed. By employing the same control strategy and system parameters, the comparison directly highlights the harmonic performance differences between the two converters.

The analysis allows us to evaluate the effectiveness of the two converters in maintaining low THD% levels. It confirms the advantages of using the 5-level NPC converter, as it demonstrates superior performance by achieving lower THD% levels compared to the two-level VSC configuration. These findings validate the suitability of the 5-level NPC converter for applications where harmonic reduction is a critical consideration.

	8 m/s	16m/s
Voltage THD%	56.48%	58.03%
Current THD%	3.04%	8.95%

Table 7.1: 2L VSC THD Analysis

	8 m/s	16m/s
Voltage THD%	29.85%	27.53%
Current THD%	2.84%	2.43%

Table 7.2: 5L NPC VSC THD Analysis

The comparison between the 2-level and 5-level NPC converters indicates that the 5-level NPC converter outperforms the 2-level counterpart in handling changes in wind speed and achieving lower THD levels. This superiority arises from the 5-level converter's ability to provide finer control over the output waveform through a higher number of switching pulses. The 5-level NPC converter's enhanced flexibility in pulse modulation allows it to respond swiftly and effectively to dynamic changes in wind conditions, thereby reducing harmonic distortions and ensuring a high-quality output voltage. Consequently, the 5-level NPC converter becomes the preferred choice, especially in applications where harmonic reduction is of utmost importance. In renewable energy systems, such as WECS-PMSG, maintaining low THD levels is crucial for seamless integration with the grid and ensuring stable and efficient operation.

Chapter 8

Conclusion

The research conducted a thorough investigation to improve the stability and power quality of WECS using PMSGs connected to the grid through 5L NPC voltage source converter. It began with clear objectives, guiding a systematic exploration that led to valuable insights and advancements in the field. The study focused on mathematical modeling and sizing of system components, particularly examining the 5-NPC VSC topology and its AC-side and DC-side dynamics. Additionally, it derived open-loop and closed-loop transfer functions for generator-side and grid-side converter controllers, providing important insights into system behavior and control mechanisms. The meticulous design and stability analysis of these controllers using MATLAB software contributed significantly to understanding control strategies for enhancing system performance and grid integration. The research emphasized the crucial role of modeling and analysis in optimizing WECS operation and highlighted the effectiveness of advanced control techniques in meeting performance criteria.

Furthermore, the investigation explored the practical implementation of system components and controllers using the PSCAD software package. This facilitated comprehensive performance evaluation and validation of proposed control schemes. Through detailed simulations, the study confirmed the effectiveness of the proposed model and control strategies in achieving predefined objectives. Significant insights emerged from these simulations, revealing various aspects of system behavior under different operating conditions. Specifically, the study highlighted the system's response to varying wind speeds, the stabilization of the DC-link voltage to ensure uninterrupted power flow from the generator to the grid. Moreover, the study showcased the effectiveness of the inner current controller in tracking reference currents and maintaining them within desired limits, thereby enhancing system stability and performance during dynamic conditions.

Additionally, the study investigated the relationship between wind speed and rotor angular speed, clarifying the role of the reactive power controller in regulating power flow and ensuring grid stability. An analysis of Total Harmonic Distortion (THD) showed significant reductions with the proposed 5L NPC topology compared to traditional converter topologies, indicating improved power quality and better grid compatibility. These findings highlighted the potential of advanced converter topologies in reducing harmonic distortions and enhancing overall system performance. Based on the results obtained, this dissertation successfully implemented the WECS-PMSGs connected to the grid through a 5L NPC voltage source converter configuration. It can be deduced, therefore, that VSC-based PMSG can be implemented utilizing a phase lead and lag compensator with a VOC controller to improve the stability, performance and grid integration of WECS.

Summary of how each objective was achieved :

Investigate the characteristics and behavior of the proposed WECS-based PMSG system:

- The investigation commenced with a detailed literature review to understand existing research and establish a foundation for the study.
- Mathematical models were developed based on fundamental principles of electromagnetics, mechanical dynamics, and power electronics to accurately represent the behavior of the WECS-based PMSG system.
- These models incorporated parameters such as turbine characteristics, generator dynamics, converter operation, and grid interaction to capture the system's behavior under various operating conditions.
- Simulation tools were employed to analyze the dynamic response of the system to changes in wind speed, grid disturbances, and load variations.

Develop a comprehensive control strategy for the 5L NPC voltage source converter to effectively manage power flow and ensure stable operation:

- The development of the control strategy involved a systematic approach, starting with a thorough understanding of the system dynamics and control objectives.
- Control algorithms were designed using advanced control techniques, including phase and lag compensates, with VOC control, to achieve desired performance criteria such as voltage regulation, power factor correction, and grid synchronization.
- Stability analysis, including Bode plots was conducted to ensure the robustness and stability of the control system under various operating conditions.

Analyze the performance of the control system under varying wind speeds and study its ability to maintain stable power delivery to the grid:

- Simulations were performed to analyze the response of the control system to changes in wind speed and assess its ability to maintain stable power delivery to the grid.
- Dynamic models of wind turbines, including aerodynamic effects, mechanical inertia, and turbine response characteristics, were integrated with the control system to simulate realistic operating conditions.
- The control system's response to transient events, such as wind gusts, turbine overspeed, and grid disturbances, was analyzed to evaluate its effectiveness in maintaining stable power output and grid stability.

Evaluate and compare the power quality of the WECS with the 5L NPC converter to traditional control approaches, such as two-level voltage source converters:

- Power quality assessment involved the analysis of various parameters such as THD, voltage regulation, frequency stability, and transient response.
- Comparative studies were conducted between the WECS with the 5L NPC converter and conventional control approaches, such as two-level voltage source converters, to assess their impact on power quality and grid performance.
- Simulation results were analyzed to quantify improvements in power quality metrics and validate the effectiveness of the proposed control strategy in enhancing grid integration and stability.

Assess the impact of the control strategy on system efficiency, including reduced switching losses and improved overall performance:

- Optimization techniques, such as SPWM optimization and switching frequency selection, were employed to minimize energy losses and improve overall system efficiency.

Investigate the system's response to transient conditions and examine its ability to handle sudden changes in wind speed and power demand:

- Transient analysis involved the study of system response to sudden changes in wind speed, load variations, and grid disturbances.
- Dynamic simulations were conducted to evaluate the system's transient response time, stability margins, and ability to recover from transient events.
- Control system parameters, including gain settings, feedback loops, and controller bandwidth, were optimized to improve transient response characteristics and enhance system stability.

8.1 Recommendations

The list below are the recommendations for future work based on the outcomes of the study:

Model Predictive Control (MPC) Implementation: Investigate the feasibility and benefits of implementing MPC algorithms tailored for WECS-PMSG systems with 5L NPC converters. Evaluate MPC's ability to optimize power extraction from varying wind speeds while ensuring grid stability and minimizing wear on system components.

Adaptive Control Strategies: Explore adaptive control strategies that can dynamically adjust control parameters based on real-time system conditions and performance feedback. Adaptive control algorithms could enhance system robustness and responsiveness to changes in wind speed, grid disturbances, and component aging.

Integration of Machine Learning Techniques: Investigate the integration of machine learning techniques, such as neural networks and reinforcement learning, to develop adaptive control systems for WECS-PMSGs. Utilize historical data and real-time sensor inputs to train control algorithms to optimize system performance and adapt to changing operating conditions.

Fault Detection and Diagnosis: Develop advanced fault detection and diagnosis algorithms to identify and mitigate potential failures or malfunctions in WECS-PMSG systems equipped with 5L NPC converters. Implement anomaly detection techniques and fault isolation strategies to enhance system reliability and minimize downtime.

Hierarchical Control Architectures: Design hierarchical control architectures that enable coordination between different control layers, such as turbine-level control, converter control, and grid interaction control. Hierarchical control schemes can optimize system operation, improve fault tolerance, and facilitate integration with grid-level control strategies.

Experimental Validation: Conduct experimental validation studies to verify the performance and reliability of newly proposed control strategies and system configurations in real-world environments. Collaborate with industry partners and research institutions to establish test facilities and field trials for comprehensive validation of theoretical findings.

By incorporating these recommendations, researchers can leverage advanced control strategies to optimize the performance, reliability, and grid integration capabilities of WECS-PMSG systems, contributing to the widespread adoption of renewable energy technologies and the transition towards a sustainable energy future.

Reference

[1] Q.-C. Zhong, Z. Ma, W.-L. Ming, and G. C. Konstantopoulos, "Grid-friendly wind power systems based on the synchronverter technology," *Energy Conversion and Management*, vol. 89, pp. 719–726, 2015.

[2] J. S. Thongam and M. Ouhrouche, "Mppt control methods in wind energy conversion systems," *Fundamental and advanced topics in wind power*, vol. 15, pp. 339–360, 2011.

[3] H. Z. G. E. Saady, E. A. Ibrahim and M. M. Soliman, "Analysis of wind turbine driven permanent magnet synchronous generator under different loading condition," *Innovative Systems Design and Engineering*, vol. 4, pp. 97–111, 2013.

[4] D.-C. Phan and S. Yamamoto, "Maximum energy output of a dfig wind turbine using an improved mppt-curve method," *Energies*, vol. 8, no. 10, pp. 11 718–11 736, 2015. [Online]. Available: https://www.mdpi.com/1996-1073/8/10/11718

[5] H. Patel and V. K. Sood, "Modeling of voltage source converter based hvdc system in emtp-rv," in *2010 IEEE Electrical Power Energy Conference*, 2010, pp. 1–6.

[6] G. P. Adam, *Voltage Source Converter: modulation, modelling, control and applications in power systems*. CreateSpace, 2014.

[7] B. Zhang and D. Qiu, *Multi-terminal High-voltage Converter*. John Wiley & Sons, 2018.

[8] L. Zhang, L. Harnefors, and H.-P. Nee, "Power-synchronization control of grid-connected voltage-source converters," *IEEE Transactions on Power systems*, vol. 25, no. 2, pp. 809–820, 2009.

[9] V. R. de Souza, L. S. Barros, and F. B. Costa, "Performance comparison of 2l-vsc, 3l-npc, and 3l-mmc converter topologies for interfacing grid-connected systems," *Simpósio Brasileiro de Sistemas Elétricos-SBSE*, vol. 1, no. 1, 2020.

[10] R. Puthiyavapillai and J. Senthilkumar, "An improved dtfc based five levels - npc inverter fed induction motor for torque ripple minimization," *International Journal of Power Electronics and Drive Systems (IJPEDS)*, vol. 7, p. 531, 06 2016.

[11] T. W. Shire, "Vsc-hvdc based network reinforcement," 2009.

[12] M. Z. M. Yin, G. Li and C. Zhao, "Modeling of the wind turbine with a permanent magnet synchronous generator for integration," *Power Engineering Society General Meeting, Tampa*, pp. 97–111, 2007.

[13] A. Mostafaeipour, M. Jahangiri, A. Haghani, S. J. H. Dehshiri, S. S. H. Dehshiri, A. Issakhov, A. Sedaghat, H. Saghaei, E. T. Akinlabi, S. M. Sichilalu *et al.*, "Statistical evaluation of using the new generation of wind turbines in south africa," *Energy Reports*, vol. 6, pp. 2816–2827, 2020.

[14] H. Li and Z. Chen, "Overview of different wind generator systems and their comparisons," *IET Renewable Power Generation*, vol. 2, no. 2, pp. 123–138, 2008.

[15] H. Mortazavi, H. Mehrjerdi, M. Saad, S. Lefebvre, D. Asber, and L. Lenoir, "Application of distance relay for distribution system monitoring," in *2015 IEEE Power & Energy Society General Meeting*. IEEE, 2015, pp. 1–5.

[16] T. H. Nguyen and D.-C. Lee, "Advanced fault ride-through technique for pmsg wind turbine systems using line-side converter as statcom," *IEEE transactions on industrial electronics*, vol. 60, no. 7, pp. 2842–2850, 2012.

[17] M. Singh and A. Chandra, "Application of adaptive network-based fuzzy inference system for sensorless control of pmsg-based wind turbine with nonlinear-load-compensation capabilities," *IEEE transactions on power electronics*, vol. 26, no. 1, pp. 165–175, 2010.

[18] H. Vahedi and K. Al-Haddad, "Real-time implementation of a seven-level packed u-cell inverter with a low-switching-frequency voltage regulator," *IEEE Transactions on Power Electronics*, vol. 31, no. 8, pp. 5967–5973, 2015.

[19] H. Vahedi, P.-A. Labbé, and K. Al-Haddad, "Sensor-less five-level packed u-cell (puc5) inverter operating in stand-alone and grid-connected modes," *IEEE Transactions on Industrial Informatics*, vol. 12, no. 1, pp. 361–370, 2015.

[20] F. Blaabjerg and K. Ma, "Future on power electronics for wind turbine systems," *IEEE Journal of emerging and selected topics in power electronics*, vol. 1, no. 3, pp. 139–152, 2013.

[21] M. Sharifzadeh, H. Vahedi, R. Portillo, M. Khenar, A. Sheikholeslami, L. G. Franquelo, and K. Al-Haddad, "Hybrid shm-she pulse-amplitude modulation for high-power four-leg inverter," *IEEE Transactions on Industrial Electronics*, vol. 63, no. 11, pp. 7234–7242, 2016.

[22] F. Delfino, F. Pampararo, R. Procopio, and M. Rossi, "A feedback linearization control scheme for the integration of wind energy conversion systems into distribution grids," *IEEE systems journal*, vol. 6, no. 1, pp. 85–93, 2011.

[23] S. Li, T. A. Haskew, R. P. Swatloski, and W. Gathings, "Optimal and direct-current vector control of direct-driven pmsg wind turbines," *IEEE Transactions on power electronics*, vol. 27, no. 5, pp. 2325–2337, 2011.

[24] S. Muyeen and A. Al-Durra, "Modeling and control strategies of fuzzy logic controlled inverter system for grid interconnected variable speed wind generator," *IEEE systems journal*, vol. 7, no. 4, pp. 817–824, 2013.

[25] A. Rajaei, M. Mohamadian, and A. Y. Varjani, "Vienna-rectifier-based direct torque control of pmsg for wind energy application," *IEEE transactions on industrial electronics*, vol. 60, no. 7, pp. 2919–2929, 2012.

[26] X. Yuan, F. Wang, D. Boroyevich, Y. Li, and R. Burgos, "Dc-link voltage control of a full power converter for wind generator operating in weak-grid systems," *IEEE Transactions on Power Electronics*, vol. 24, no. 9, pp. 2178–2192, 2009.

[27] Y. Li, X. Tian, C. Liu, Y. Su, L. Li, L. Zhang, Y. Sun, and J. Li, "Study on voltage control in distribution network with renewable energy integration," in *2017 IEEE Conference on Energy Internet and Energy System Integration (EI2)*, 2017, pp. 1–5.

[28] L. Yan, W. Zhibin, C. Yongning, W. Chunxia, L. Hongzhi, and T. Haiyan, "Analysis of coordinated control strategy for large-scale renewable energy vschvdc integration," in *2019 IEEE Innovative Smart Grid Technologies - Asia (ISGT Asia)*, 2019, pp. 234–238.

[29] R. R. Kumar, M. Sanjai, R. Sivashanmugam, S. Saranya, S. Sinega, and T. Logeswaran, "Grid integration of renewable energy sources with iot system," in *2022 International Conference on Sustainable Computing and Data Communication Systems (ICSCDS)*, 2022, pp. 1012–1017.

[30] A. G. Abo-Khalil, *Impacts of Wind Farms on Power System Stability*. DOI: 10.5772/55090, 2013.

[31] E. Hamatwi, I. Davidson, and M. Gitau, "Rotor speed control of a direct-driven permanent magnet synchronous generator-based wind turbine using phase-lag compensators to optimize wind power extraction," *Journal of Control Science and Engineering*, vol. 2017, pp. 1–17, 05 2017.

[32] Z. Civelek, E. Çam, M. Lüy, and H. Mamur, "Proportional–integral–derivative parameter optimisation of blade pitch controller in wind turbines by a new intelligent genetic algorithm," *IET Renewable Power Generation*, vol. 10, no. 8, pp. 1220–1228, 2016.

[33] M. R. Islam, S. Mekhilef, and R. Saidur, "Progress and recent trends of wind energy technology," *Renewable and Sustainable Energy Reviews*, vol. 21, pp. 456–468, 2013.

[34] Z. Zhang, Y. Zhao, W. Qiao, and L. Qu, "A discrete-time direct torque control for direct-drive pmsg-based wind energy conversion systems," *IEEE Transactions on Industry Applications*, vol. 51, no. 4, pp. 3504–3514, 2015.

[35] E. Hamatwi, I. E. Davidson, M. N. Gitau, and G. P. Adam, "Modeling and control of voltage source converters for grid integration of a wind turbine system," in *2016 IEEE PES PowerAfrica*, 2016, pp. 98–106.

[36] E. Hamatwi, I. Davidson, and M. Gitau, "Control of multi-level voltage source converters integrating a wind turbine system into the grid," 11 2016.

[37] N.-Y. Dai and M.-C. Wong, "Power electronics for renewable energy systems, transportation and industrial applications," in *Power Electronics for Renewable Energy Systems, Transportation and Industrial Applications*, 2014.

[38] K. Clark, N. W. Miller, and J. J. Sanchez-Gasca, "Modeling of ge wind turbine-generators for grid studies," *GE energy*, vol. 4, pp. 0885–8950, 2010.

[39] J. M. Verduzco-Duran, A. Medina-Rios, and N. M. Salgado-Herrera, "State-space model of the wind energy conversion system integrated to power grid using type-4 wind turbine/pmsg," in *2020 IEEE International Autumn Meeting on Power, Electronics and Computing (ROPEC)*, vol. 4, 2020, pp. 1–6.

[40] M. J. D. S. K. B. W. Venkata Yaramasu, Apparao Dekka, "Iet electrical power applications," in *PMSG-based wind energy conversion systems: survey on power converters and controls*, vol. 11, no. 6, 2017.

[41] A. A. Elsattar, A. M. Atallah, and E. S. F. El Tantawy, "Direct torque control and direct power control with multilevel converters for variable speed wind turbines," in *2016 Eighteenth International Middle East Power Systems Conference (MEPCON)*, 2016, pp. 480–489.

[42] S. Sewchurran and I. E. Davidson, "Introduction to the south african renewable energy grid code version 2.9 requirements (part i—introduction)," in *2017 IEEE AFRICON*. IEEE, 2017, pp. 1220–1224.

[43] A. Eberhard and R. Naude, "The south african renewable energy ipp procurement programme: Review, lessons learned & proposals to reduce transaction costs," *South Africa: University of Cape Town, Graduate School of Business*, 2017.

[44] S. Sewchurran and I. E. Davidson, "Introduction to the south african renewable energy grid code version 2.9 requirements (part iii—discussions and conclusions)," in *2017 IEEE AFRICON*. IEEE, 2017, pp. 1231–1235.

[45] I. Erlich and U. Bachmann, "Grid code requirements concerning connection and operation of wind turbines in germany," in *IEEE Power Engineering Society General Meeting, 2005.* IEEE, 2005, pp. 1253–1257.

[46] M. Yao and L. Yao, "Integration of large scale wind farm into electrical grids," *CICED 2010 Proceedings*, pp. 1–5, 2010.

[47] M. Tsili and S. Papathanassiou, "A review of grid code technical requirements for wind farms," *IET Renewable power generation*, vol. 3, no. 3, pp. 308–332, 2009.

[48] O. Alizadeh, "Control of wind energy conversion systems for large-scale integration with the power system," 2014.

[49] T. M. Haileselassie, "Control of multi-terminal vsc-hvdc systems," Master's thesis, Institutt for elkraftteknikk, 2008.

[50] S. Botha and R. Gouws, "Intelligent controller for improved efficiency of micro wind turbine generators," in *2016 international conference on the industrial and commercial use of energy (ICUE)*. IEEE, 2016, pp. 278–285.

[51] M. A. Abdullah, A. Yatim, C. W. Tan, and R. Saidur, "A review of maximum power point tracking algorithms for wind energy systems," *Renewable and sustainable energy reviews*, vol. 16, no. 5, pp. 3220–3227, 2012.

[52] I. Buehring and L. Freris, "Control policies for wind-energy conversion systems," in *IEE Proceedings C (Generation, Transmission and Distribution)*, vol. 128, no. 5. IET, 1981, pp. 253–261.

[53] A. M. Knight and G. E. Peters, "Simple wind energy controller for an expanded operating range," *IEEE Transactions on Energy Conversion*, vol. 20, no. 2, pp. 459–466, 2005.

[54] S. K. Bisoyi, R. Jarial, and R. Gupta, "Modeling and control of variable speed wind turbine equipped with pmsg," *International Journal of Emerging Technologies in Computational and Applied Sciences*, vol. 6, no. 1, pp. 56–62, 2013.

[55] S. Tripathi, A. Tiwari, and D. Singh, "Grid-integrated permanent magnet synchronous generator based wind energy conversion systems: A technology review," *Renewable and Sustainable Energy Reviews*, vol. 51, pp. 1288–1305, 2015.

[56] M. Abdullah, T. Al-Hadhrami, C. Tan, and A. H. Yatim, "Towards green energy for smart cities: Particle swarm optimization based mppt approach," *IEEE Access*, vol. PP, pp. 1–1, 10 2018.

[57] M. A. Abdullah, A. H. M. Yatim, and C. W. Tan, "An online optimum-relation-based maximum power point tracking algorithm for wind energy conversion system," in *2014 Australasian Universities Power Engineering Conference (AUPEC)*, 2014, pp. 1–6.

[58] R. D. Shukla and R. Tripathi, "Maximum power extraction schemes & power control in wind energy conversion system," *International Journal of Scientific and Engineering Research*, vol. 3, no. 6, pp. 1–7, 2012.

[59] G. Stamatiou, *Converter interactions in VSC-based HVDC systems*. Chalmers Tekniska Hogskola (Sweden), 2015.

[60] K. Padiyar and N. Prabhu, "Modelling, control design and analysis of vsc based hvdc transmission systems," in *2004 International Conference on Power System Technology, 2004. PowerCon 2004.*, vol. 1. IEEE, 2004, pp. 774–779.

[61] S. Meier, "Novel voltage source converter based hvdc transmission system for offshore wind farms," Ph.D. dissertation, KTH, 2005.

[62] Z. Chen and F. Blaabjerg, "Wind farm—a power source in future power systems," *Renewable and Sustainable Energy Reviews*, vol. 13, no. 6-7, pp. 1288–1300, 2009.

[63] S. Li and Y. Li, "A novel fast current-control method for the back-to-back converters," in *2004 IEEE International Conference on Industrial Technology, 2004. IEEE ICIT'04.*, vol. 1. IEEE, 2004, pp. 351–357.

[64] K. Padiyar and N. Prabhu, "Modelling, control design and analysis of vsc based hvdc transmission systems," in *2004 International Conference on Power System Technology, 2004. PowerCon 2004.*, vol. 1. IEEE, 2004, pp. 774–779.

[65] E. R. C. Da Silva, E. C. dos Santos, and C. B. Jacobina, "Pulsewidth modulation strategies," *IEEE Industrial Electronics Magazine*, vol. 2, no. 5, pp. 37–45, 2011.

[66] D. G. Holmes and T. A. Lipo, *Pulse width modulation for power converters: principles and practice*. John Wiley & Sons, 2003, vol. 18.

[67] G. P. Adam, "Quasi two-level operation of a five-level diode clamped converter," Ph.D. dissertation, University of Strathclyde, 2007.

[68] A. Nabae, I. Takahashi, and H. Akagi, "A new neutral-point-clamped pwm inverter," *IEEE Transactions on industry applications*, no. 5, pp. 518–523, 1981.

[69] S. Tripathi, A. Tiwari, and D. Singh, "Grid-integrated permanent magnet synchronous generator based wind energy conversion systems: A technology review," *Renewable and Sustainable Energy Reviews*, vol. 51, pp. 1288–1305, 2015.

[70] M. R. Islam, Y. Guo, and J. Zhu, "Power converters for wind turbines: Current and future development," *Materials and processes for energy: communicating current research and technological developments*, pp. 559–571, 2013.

[71] M. R. Islam, Y. Guo, J. G. Zhu, and D. Dorrell, "Design and comparison of 11 kv multilevel voltage source converters for local grid based renewable energy systems," in *IECON 2011-37th Annual Conference of the IEEE Industrial Electronics Society*. IEEE, 2011, pp. 3596–3601.

[72] S. S. Fazel, S. Bernet, D. Krug, and K. Jalili, "Design and comparison of 4-kv neutral-point-clamped, flying-capacitor, and series-connected h-bridge multilevel converters," *IEEE Transactions on Industry Applications*, vol. 43, no. 4, pp. 1032–1040, 2007.

[73] S. Li, T. A. Haskew, and L. Xu, "Conventional and novel control designs for direct driven pmsg wind turbines," *Electric Power Systems Research*, vol. 80, no. 3, pp. 328–338, 2010.

[74] N. Freire, J. Estima, and A. Cardoso, "A comparative analysis of pmsg drives based on vector control and direct control techniques for wind turbine applications," *Przeglad Elektrotechniczny*, vol. 88, no. 1, pp. 184–187, 2012.

[75] C.-M. Hong, C.-H. Huang, and F.-S. Cheng, "Sliding mode control for variable-speed wind turbine generation systems using artificial neural network," *Energy Procedia*, vol. 61, pp. 1626–1629, 2014.

[76] U. Jassmann, J. Berroth, D. Matzke, R. Schelenz, M. Reiter, G. Jacobs, and D. Abel, "Model predictive control of a wind turbine modelled in simpack," in *Journal of Physics: Conference Series*, vol. 524, no. 1. IOP Publishing, 2014, p. 012047.

[77] M. Narayana and G. Putrus, "Optimal control of wind turbine using neural networks," in *45th International Universities Power Engineering Conference UPEC2010*. IEEE, 2010, pp. 1–5.

[78] A. Mechter, K. Kemih, and M. Ghanes, "Backstepping control of a wind turbine for low wind speeds," *Nonlinear Dynamics*, vol. 84, no. 4, pp. 2435–2445, 2016.

[79] J. D. Irwin, *The industrial electronics handbook*. CRC press, 1997.

[80] J. M. Carrasco Solís, L. García Franquelo, J. T. Bialasiewicz, E. Galván Díez, R. C. Portillo Guisado, M. d. l. Á. Martín Prats, J. I. León Galván, and N. Moreno-Alfonso, "Power-electronic systems for the grid integration of renewable energy sources: a survey," *IEEE Transactions on Industrial Electronics, 53 (4), 1002-1016.*, 2006.

[81] A. Arranz-Gimon, A. Zorita-Lamadrid, D. Morinigo-Sotelo, and O. Duque-Perez, "A review of total harmonic distortion factors for the measurement of harmonic and interharmonic pollution in modern power systems," *Energies*, vol. 14, no. 20, p. 6467, 2021.

[82] F. De La Rosa, *Harmonics and power systems*. CRC press Boca Raton, 2006, vol. 13.

[83] B. Wu, Y. Lang, N. Zargari, and S. Kouro, *Power conversion and control of wind energy systems*. John Wiley & Sons, 2011.

[84] M. Sanz, A. Llombart, A. Bayod, and J. Mur, "Power quality measurements and analysis for wind turbines," in *Proceedings of the 17th IEEE Instrumentation and Measurement Technology Conference [Cat. No. 00CH37066]*, vol. 3. IEEE, 2000, pp. 1167–1172.

[85] H. A. Faraasen, "Power electronic converters for efficient operation of the modular hvdc generator for offshore wind power," Master's thesis, NTNU, 2020.

[86] M. Stecca, T. B. Soeiro, L. R. Elizondo, P. Bauer, and P. Palensky, "Comparison of two and three-level dc-ac converters for a 100 kw battery energy storage system," in *2020 IEEE 29th International Symposium on Industrial Electronics (ISIE)*. IEEE, 2020, pp. 677–682.

[87] A. Arrizabalaga, M. Mazuela, A. Idarreta, U. Iraola, and I. Aizpuru, "System level optimization of 5 mw wind converter using 3l-npc topology in medium voltage with 1.7 kv igbt," in *IECON 2020 The 46th Annual Conference of the IEEE Industrial Electronics Society*. IEEE, 2020, pp. 4127–4132.

[88] A. T. S.M.Tripathi and D. Singh, "Grid-integrated permanent magnet synchronous generator based wind energy conversion systems: a technology review," in *Renewable and Sustainable Energy Reviews*, vol. 51, no. 4598, 2015, pp. 1288–1305.

[89] W. Y. A.L. Soriano and J. Rubio, "Modeling and control of wind turbine," mathematical problems in engineering," in *Renewable and Sustainable Energy Reviews*, vol. 51, no. 982597, 2013, p. 7.

[90] J. Thongam, P. Bouchard, H. Ezzaidi, and M. Ouhrouche, "Wind speed sensorless maximum power point tracking control of variable speed wind energy conversion systems," in *2009 IEEE International Electric Machines and Drives Conference*. IEEE, 2009, pp. 1832–1837.

[91] T. W. Shire, "Vsc-hvdc based network reinforcement," 2009.

[92] M. Yin, G. Li, M. Zhou, and C. Zhao, "Modeling of the wind turbine with a permanent magnet synchronous generator for integration," in *2007 IEEE Power Engineering Society General Meeting*. IEEE, 2007, pp. 1–6.

[93] L. Fateh, O. Ahmed, O. Amar, D. Abdelhak, and B. Lakhdar, "Modeling and control of a permanent magnet synchronous generator dedicated to standalone wind energy conversion system," *Frontiers in Energy*, vol. 10, no. 2, pp. 155–163, 2016.

[94] G. P. Adam, *Voltage Source Converter: modulation, modelling, control and applications in power systems*. CreateSpace, 2014.

[95] ——, "Quasi two-level operation of a five-level diode clamped converter," Ph.D. dissertation, University of Strathclyde, 2007.

[96] O. Gomis-Bellmunt, A. Junyent-Ferre, A. Sumper, and J. Bergas-Jane, "Control of a wind farm based on synchronous generators with a central hvdc-vsc converter," *IEEE Transactions on power systems*, vol. 26, no. 3, pp. 1632–1640, 2010.

[97] G. P. Adam, *Voltage Source Converter: modulation, modelling, control and applications in power systems*. CreateSpace, 2014.

[98] A. D. Hansen and G. Michalke, "Modelling and control of variable-speed multi-pole permanent magnet synchronous generator wind turbine," *Wind Energy: An International Journal for Progress and Applications in Wind Power Conversion Technology*, vol. 11, no. 5, pp. 537–554, 2008.

[99] J. Zhu, J. M. Guerrero, W. Hung, C. D. Booth, and G. P. Adam, "Generic inertia emulation controller for multi-terminal voltage-source-converter high voltage direct current systems," *IET Renewable Power Generation*, vol. 8, no. 7, pp. 740–748, 2014.

[100] C. Du, *VSC-HVDC for industrial power systems*. Chalmers Tekniska Hogskola (Sweden), 2007.

[101] A. ABB, "Grid systems-hvdc,"hvdc light-it's time to connect," abb," Ludvika, Technical Report, Tech. Rep., 2012.

[102] ——, "Grid systems-hvdc,"hvdc light-it's time to connect," abb," Ludvika, Technical Report, Tech. Rep., 2012.

[103] N.-Y. Dai and M.-C. Wong, "Design considerations of coupling inductance for active power filters," in *2011 6th IEEE Conference on Industrial Electronics and Applications*. IEEE, 2011, pp. 1370–1375.

[104] O. Giddani, A. Y. Abbas, G. P. Adam, O. Anaya-Lara, and K. L. Lo, "Multi-task control for vsc–hvdc power and frequency control," *International Journal of Electrical Power & Energy Systems*, vol. 53, pp. 684–690, 2013.

[105] C. Blake and C. Bull, "Igbt or mosfet: choose wisely," *International Rectifier*, pp. 1–5, 2001.

[106] G. Beale, "Phase lead compensator design using bode plots," in *George Mason University*, 2003.

Appendix A

Appendix

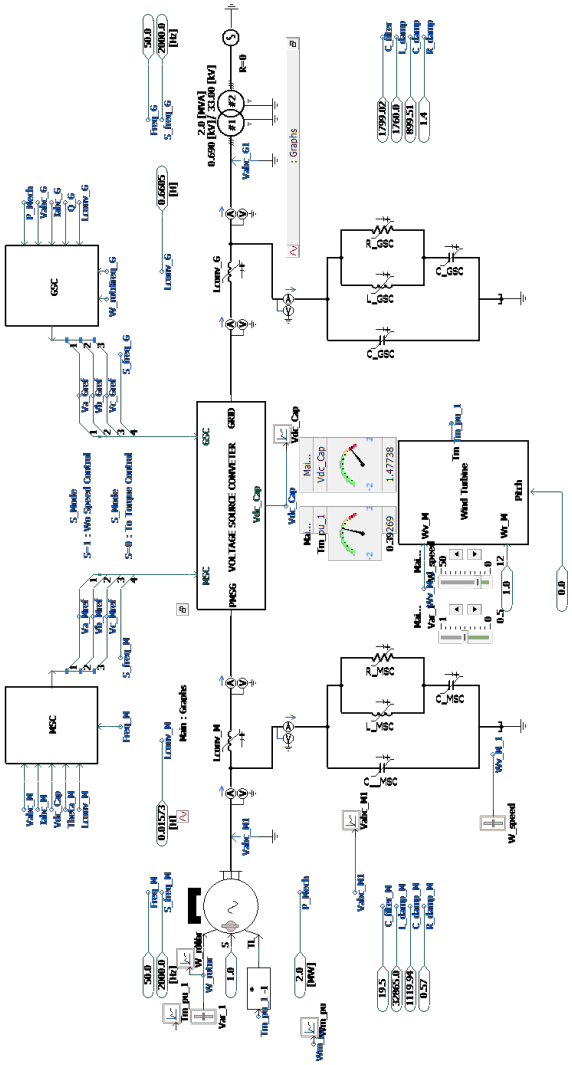

Figure A.1: Subsystem block

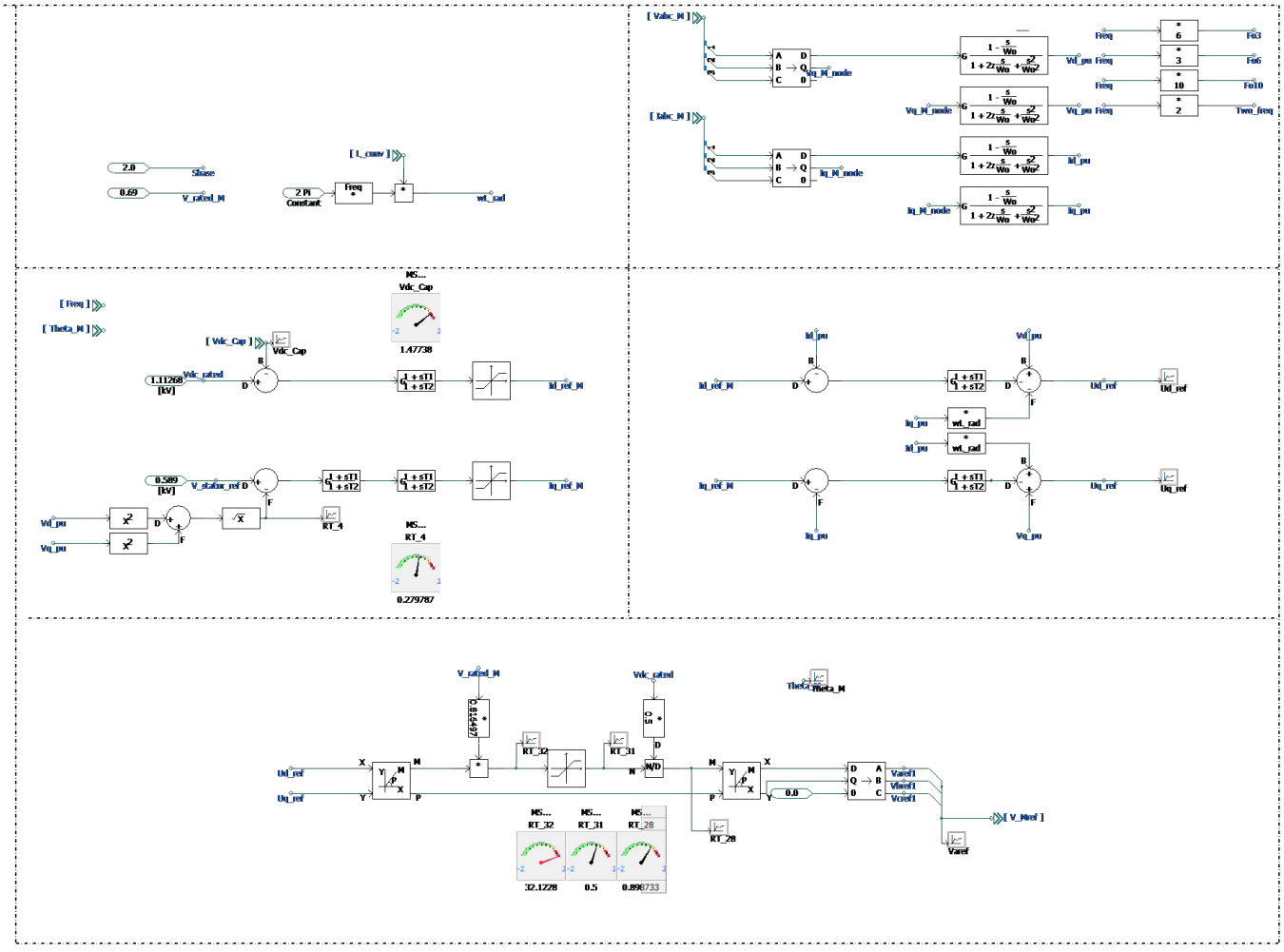

Figure A.2: Machine side control block

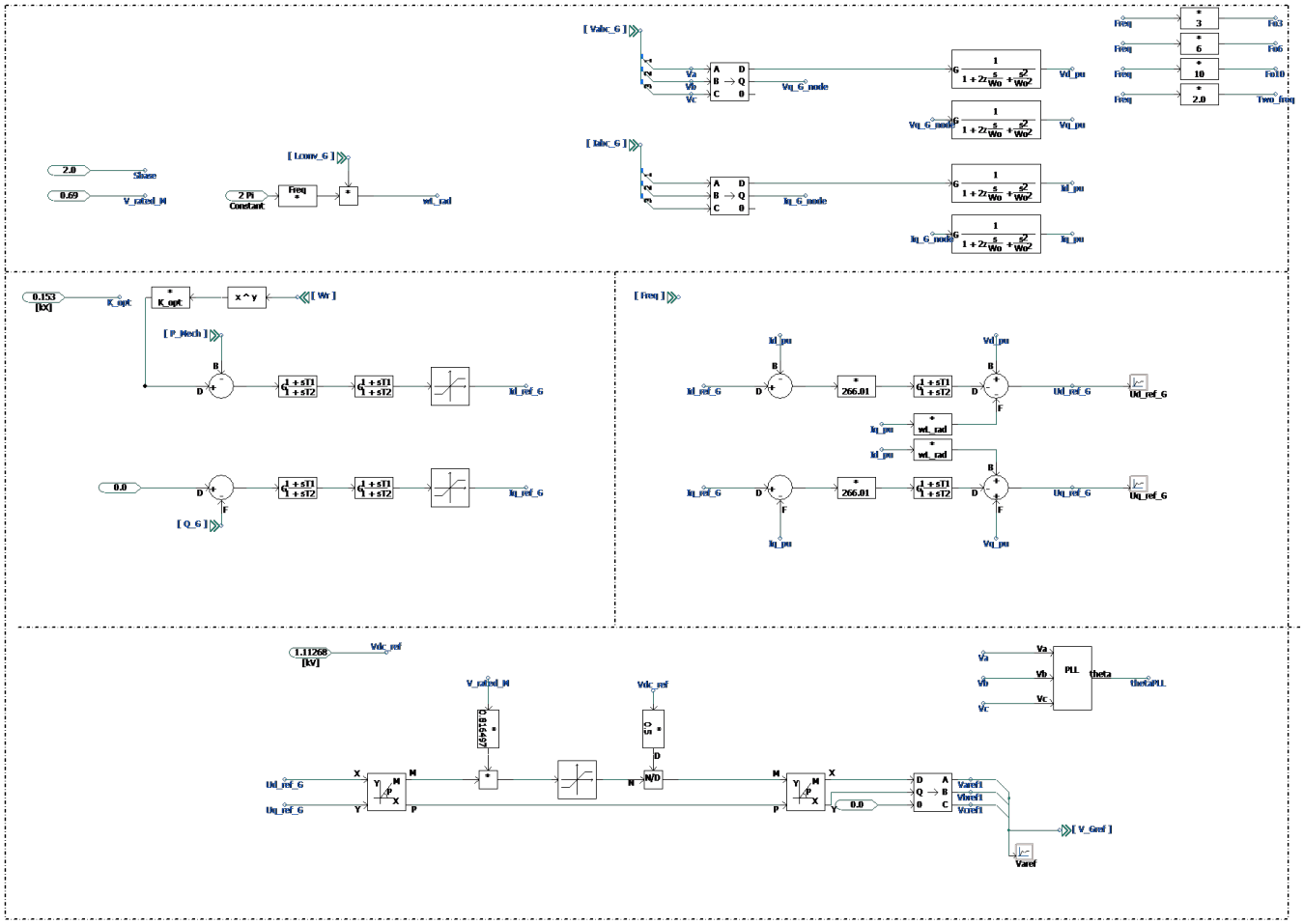

Figure A.3: Grid side control block